ABSTRACT

A STUDY OF THE GAMOW TELLER STRENGTH IN
^{40,42,44,48}Ca FROM THE (p,n) REACTION AT 119 MeV

By

Janaki Narayanaswamy

The (p,n) reaction at 119.3 MeV has been employed to measure the spin transfer strength in ^{40,42,44} and ^{48}Ca. The experiment was carried out at the Indiana University Cyclotron Facility using the neutron time of flight apparatus and time compensated scintillation detectors at a target-to-detector distance of 131.5 meters. Analyses of the data by several different methods indicate that a significant amount of 1^+ strength is contained in what is conventionally taken as the background in neutron energy spectra. This finding explains at best partially the apparent quenching of the spin depdendent operator $V_{0\tau}$ when the data were analyzed ignoring such a background. An earlier observation that the 16.8 MeV state in ^{48}Sc is wider than the parent state in ^{48} Ca at an excitation of 2.52 MeV is confirmed by the present data. The 2.73 MeV state in ^{48}Sc is found to have an angular distribution corresponding to L=0.

A STUDY OF THE GAMOW TELLER STRENGTH IN ^{40,42,44,48}Ca FROM THE (p,n) REACTION AT 119 MeV

By

Janaki Narayanaswamy

A DISSERTATION

Submitted to
Michigan State University
in partial fulfillment of the requirements
for the degree of

DOCTOR OF PHILOSOPHY

Department of Physics and Astronomy

1983

DEDICATED

TO

Seethalakshmi and Narayanaswamy

(My Parents)

ACKNOWLEDGMENTS

It is a pleasure to thank Professor Sam M. Austin for his guidance. His patience and constructive criticisms have been indispensable to the completion of this work. I have also benefited greatly from the assistance provided by Professor Aaron Galonsky during data acquisition and by Dr. Olaf Scholten during the final stages of the analysis.

I express my gratitude to the Department of Physics and Astronomy of Michigan State University and the National Superconducting Cyclotron Laboratory for financial support during my graduate program. The faculty, staff and fellow students at the M.S.U. Cyclotron Laboratory deserve special mention for their kindness. The hospitality extended by the Indiana University Cyclotron Facility and the assistance provided by Professor Charles D. Goodman and Dr. T.N. Taddeucci are gratefully acknowledged. Thanks to R. Geetha, Shobha Prasad and Parul Vora for making life in East Lansing more enjoyable. I am also most grateful to Barbara Jacak and Patty Pirnie for their support during the difficult time of thesis writing and to Ron Fox for helping me understand the mysteries of the program SCOPEFIT. Special thanks to Shari Conroy for the typing of this thesis.

Lastly, thanks to my parents for their love and support to a daughter with unconventional ambitions, to Rukku and Raghu (my sister and brother-in-law) for the countless pep talks, to my sister Hema for her wishes and to my brother Kedarnath for repairing everything from wristwatch to car and keeping me going.

TABLE OF CONTENTS

LIST OF TABLES

LIST OF TABLES (continued)

LIST OF FIGURES

LIST OF ABBREVIATIONS

DWBA	Distorted Wave Born Approximation
DWIA	Distorted Wave Impulse Approximation
F	Fermi Transition or Operator
GT	Gamow Teller Transition or Operator
IAS	Isobaric Analog State
IUCF	Indiana University Cyclotron Facility
N x N x Th	N times the ^{228}Th Compton edge
NTOF	Neutron Time of Flight
PWBA	Plane Wave Born Approximation
TAC	Time to amplitude converter
TOF	Time of Flight

I. Introduction

The discovery of the neutron in 1932 was fundamental to the formulation of successful nuclear models. An underlying assumption in all such models and verified experimentally is that the two body nucleon-nucleon force possesses charge symmetry and charge independence i.e., it is the same for p-p, n-n, and p-n systems. In this picture, the proton and the neutron are viewed as different manifestations of the same fundamental entity, the nucleon. It is in the z axis projection of the isospin (t_z) in isospin space that the two differ: the proton has $t_z = -1/2$; for the neutron, $t_z = +1/2$. Then the nucleus can be viewed as an aggregate of nucleons, whose intrinsic states are distributed among spin up or spin down, and isospin up or isospin down donfigurations. But recent experiments at intermediate energies have led to speculation that one may have to consider additional degrees of freedom for the nucleon, for example, the Δ resonance (Os 79, Bo 81, Go 82, Ra 82, Ga 82). To be specific, this has been brought about by an apparent quenching of the spin dependent operators observed in (p,p') (M1 strength) and (p,n) (GT strength) reactions. Obviously, such a coupling of nucleon structure to nuclear structure is of fundamental importance to our picture of the nucleus. The goal of this

study is to locate the spin transfer strength from ^{40,42,44} and ^{48}Ca, and to study the systematics of the strength as a function of neutron excess. We employed the (p,n) reaction on the calcium isotopes at a proton energy of 119 MeV. The following considerations will explain the particular usefulness of the (p,n) reaction in this context and the relevance of the chosen bombarding energy.

The strength of the nucleon-nucleon interaction at short range forces one to use an effective interaction, v_{eff}, in calculations of nuclear structure and reactions. This interaction is assumed to be the sum of two body interactions over all possible pairs of nucleons in the system. Many body forces present in nuclei contribute less than 10% of the binding energy (Be 72). Therefore, the nuclear Hamiltonian can be written

$$H = \sum_i K_i + \sum_{i<j} V_{ij} \qquad 1.1$$

Here K_i is the kinetic energy operator for the i^{th} nucleon, and V_{ij} is the two body potential between the i^{th} and j^{th} nucleons.

In practice, phenomenological effective potentials of the form given in Eq. 1.2 are used to fit nucleon-nucleus or nucleon-nucleon scattering data (Au 79);

$$\begin{aligned} V_{ij} &= V_{ij}^{central} + V_{ij}^{tensor} + V_{ij}^{spin\text{-}orbit} \\ V_{ij}^{central} &= V_o(\underline{r}) + V_\sigma(\underline{r})\vec{\sigma}_i\cdot\vec{\sigma}_j + V_\tau(\underline{r})\vec{\tau}_i\cdot\vec{\tau}_j + \\ &\quad V_{\sigma\tau}\vec{\sigma}_i\cdot\vec{\sigma}_j\vec{\tau}_i\cdot\vec{\tau}_j \\ V_{ij}^{tensor} &= (V^{tensor}(\underline{r}) + V_\tau^{tensor}(\underline{r})\tau_i\cdot\tau_j)S_{ij} \end{aligned} \qquad 1.2$$

$$V^{\text{spin-orbit}} = (V^{SO}(\underline{r}) + V_{\tau}^{SO}(\underline{r})\vec{\tau}_i \cdot \vec{\tau}_j)\underline{L}\cdot\underline{S}$$

S_{ij} = Tensor operator 1.2 cont.

Simple shapes are assumed for the V's, often sums of Yukawas, and the strengths of $V_o(\underline{r})$, $V_\sigma(\underline{r})$, $V_\tau(\underline{r})$, $V_{\sigma\tau}(\underline{r})$ are determined from such fits.

Recent work on (p,n) reactions at intermediate energies has brought to light a specific behavior of the effective interaction that can be used to advantage (Go 80). The case in question is the total Gamow-Teller strength, obtainable directly from beta decay measurements only for a few $N < Z$ nuclei. In beta decay, a free or a bound neutron transforms to a proton or vice versa. There are two components to the coupling of the nucleon to the weak field established by this process: (a) The spin independent vector coupling or Fermi β decay (F), and (b) The spin dependent axial vector coupling or Gamow-Teller β decay (GT). For a free neutron the decay rate is expressed as (Go 81)

$$\frac{K}{ft} = G_v^2 + 3G_a^2 \qquad 1.3$$

where G_v and G_a are the vector and axial vector coupling constants. When a neutron is bound in a nucleus, its decay rate is modified by the presence of the neighboring nucleons and can be written

$$\frac{K}{ft} = G_v^2\langle F\rangle^2 + G_a^2\langle GT\rangle^2 \ , \qquad 1.4$$

where

$$B_f^{\pm}(F) \equiv \langle F \rangle^2 \equiv \frac{1}{2J+1} \left| \langle f || \sum_k t_k^{\pm} || i \rangle \right|^2$$

$$B_f^{\pm}(GT) \equiv \langle GT \rangle^2 \equiv \frac{1}{2J+1} \left| \langle f || \sum_k \sigma_k t_k^{\pm} || i \rangle \right|^2$$

$|i\rangle$, $|f\rangle$ are the initial and final states and $t_k^{\pm}$, $\sigma_k t_k^{\pm}$ are the spin and spin-isospin operators that mediate the transitions. The presence of other nucleons may block some transitions because the single particle states into which they must decay may already be occupied.

It is useful to define the reduced transition probabilities B(F) and B(GT) such that B(F) = 1 and B(GT) = 3 for a free neutron as is implied by Eq. 1.3. In these units, it can be shown that the difference in beta decay strengths for a nucleus with a neutron excess N-Z is given by

$$B(F) = S_{\beta-} - S_{\beta+} = N-Z \text{ for a Fermi transition}$$

$$B(GT) = S_{\beta-} - S_{\beta+} = 3(N-Z) \text{ for a GT transition}$$

This model independent sum rule is derived in Appendix A. Therefore, we can write

$$B(F) \geq N-Z \text{ and}$$

$$B(GT) \geq 3(N-Z)$$

Thus, N-Z and 3(N-Z) are the minimum strengths one would expect to find for Fermi and GT transitions respectively. The equality holds when $S_{\beta+}$ is negligible.

It had been a puzzling observation that measured beta decay rates were slow compared to simple model expectations. The discovery of the isobaric analog state (IAS) in (p,n) reactions contributed greatly to the understanding of this

phenomenon. The IAS happens to be nearly the projection of the collective Fermi operator on the final nucleus and in heavy nuclei the Coulomb displacement energy puts this state out of the reach of beta decay, hence the slow rate. This discovery further prompted postulation of the existence of a giant GT resonance that would contain most of the GT strength and would be located at an excitation energy near and slightly above the IAS (Ik 63). In fact, if the nuclear Hamiltonian were spin independent, then the IAS and the GT would be degenerate. But the spin dependent interaction shifts the GT distribution. Obviously, the existence of this giant GT resonance, out of the reach of beta decay for $N > Z$ nuclei, had to be tested by some probe other than beta decay. Table 1.1 lists the relevant operators for different probes

Table 1.1
Relevant operators for different probes

Transition	$0^+ \to 0^+$ $S=0$ $L=0$	$0^+ \to 1^+$ $S=1$
(p,n)	$\sum_j V_\tau \vec{\tau}_p \cdot \vec{\tau}_j$	$\sum_j V_{\sigma\tau} \vec{\sigma}_p \cdot \vec{\sigma}_j \vec{\tau}_p \cdot \vec{\tau}_j$
β decay	$\sum_j \tau_j$ (Fermi	$\sum_j \sigma_j \cdot \tau_j$ (GT)
M_1^*		$\sum_j (\mu_p - \mu_j) \vec{\sigma}_j \cdot \vec{\tau}_j$

*Ignoring current and small isoscalar parts of the operator.

In the (p,n) reaction, the target nucleus gains one more proton and loses a neutron. In this sense, the reaction is similar to beta decay. Since the operators have the same form in spin-isospin space one would expect strong transitions in GT beta decay or M1 to be strong in (p,n) reactions. This similarity suggests that the (p,n) reaction can be used to mimic beta decays that are prohibited by energy considerations and to determine GT strengths. But one has to study first, nuclei with known GT matrix elements so as to understand the signature in the (p,n) reaction that corresponds to beta decay strength and establish empirical quantitative relationships between the two. More importantly, the beta decay conditions have to be simulated with the (p,n) reaction as closely as possible (near zero momentum transfer, for example) and quantitative corrections made for deviations from these conditions. Then it is possible, in principle, to extract beta decay information from the (p,n) reaction in an almost model independent way (Go 80).

It was seen that the IAS, corresponding to superallowed Fermi transitions stood out in (p,n) spectra. But the GT transitions were not apparent in low energy (p,n) reactions. The first evidence for the existence of GT giant resonances came from 45 MeV (p,n) data taken at M.S.U. (Do 75). It was soon apparent from intermediate energy proton beams (up to 200 MeV) at IUCF that GT transitions dominate the 0° (p,n) spectra at energies greater than about 100 MeV (Go 78). This is a direct consequence of the relative behavior of V_τ

and $V_{\sigma\tau}$ as a function of proton energy (Ta 81). These intermediate energy (p,n) reaction studies led to the following observations (Go 80).

The (p,n) reaction is mediated by isovector parts of V_{jp} i.e., $V_{\sigma\tau}$ and V_{τ} in Eq. 1.4. At 0° (small momentum transfer) only low momentum components contribute appreciably to the cross section. Therefore, at 0°, the (p,n) reaction favors states with significant allowed Fermi ($L = 0$, $S = 0$) and GT ($L = 0$, $S = 1$) matrix elements. At intermediate energies, strong transitions in (p,n) are direct; central parts in V_{jp} dominate; for small q, noncentral parts can be neglected. Also at 120 MeV, the impulse approximation has some validity i.e., $V_{eff} \tilde{=}$ the free nucleon-nucleon t matrix.

In the distorted wave approximation the cross section for a reaction A(a,b)B is proportional to the square of the transition matrix element and can be written (Go 80)

$$\frac{d\sigma}{d\Omega} = \left(\frac{\mu}{2\pi\hbar^2}\right)^2 \frac{k_f}{ki} \frac{1}{(2J_i+1)(2S_p+1)} \times$$

$$\sum \left| \int \chi_f^{(-)*}(\underline{r}_p) \langle f | \sum_j V_{jp}(1 - P_{jp}) | i \rangle \chi_i^{(+)}(\underline{r}_p) d^3 r_p \right|^2 \qquad 1.5$$

where the χ's are distorted waves generated in an appropriate optical potential; μ and k denote the reduced mass and wave number in the center of mass system respectively; $\langle f | \sum_j V_{jp}(1-P_{ij}) | i \rangle$ is the target matrix element, and V_{jp} is the effective nucleon-nucleon interaction; knockout exchange is excluded by the term $1 - P_{jp}$ where P_{jp} is the permutation operator. The inner sum is over all the nucleons in the

target; the outer sum is over the initial and final spin projections of the projectile and the target.

Under the conditions observed for (p,n) reactions at 120 MeV, the 0° differential corss section can be written

$$\frac{d\sigma}{d\Omega}(0°) \simeq \left(\frac{\mu}{\pi\hbar^2}\right)\frac{k_f}{k_i}\{N_\tau^D|J_\tau<F>|^2+N_{\sigma\tau}^D|J_{\sigma\tau}<GT>|^2\} \qquad 1.6$$

where J_τ and $J_{\sigma\tau}$ are the magnitudes of the volume integrals of the effective spin independent $(\vec{\tau}_j\cdot\vec{\tau}_p)$ and spin dependent $(\vec{\sigma}_j\cdot\vec{\sigma}_p\ \vec{\tau}_j\cdot\vec{\tau}_p)$ isovector central terms in $V_{jp}(1-P_{jp})$, N_τ^D and $N_{\sigma\tau}^D$ are distortion factors defined to be the ratio of the DWBA and PWBA cross sections; $|<F>|^2$ and $|<GT>|^2$ are the squares of the Fermi and Gamow-Teller matrix elements given by 1.4. Following Goodman et al., (Go 80) define for a pure Fermi or GT transition,

$$K = \frac{d\sigma(0°)}{d\Omega}/\{\left(\frac{\mu}{\pi\hbar^2}\right)^2\frac{k_f}{k_i}N^D\} \qquad 1.7$$

Then from a plot of K vs. B(F) or B(GT) one can extract empirically the corresponding interaction strengths, J_τ and $J_{\sigma\tau}$ in Equation 1.6. Goodman et al., used the local t-matrix interaction of Love et al., (Lo 78) and computed the distortion factor N^D. They find that N^D shows a smooth exponential A dependence and is only moderately sensitive to the reaction Q values and the model nuclear wave functions. By comparing the 0° (p,n) cross sections of the IAS and GT states in the case of several nuclei to known F and GT beta decay matrix elements, Goodman et al., find that there is a linear correspondence between these two quantities and that

interaction strengths at $E_p = 120$ MeV are 168 MeV-fm (spin flip) and 89 MeV-fm (non spin flip). Figures 1.1a and 1.1b show the data and the fits from their work. This finding demonstrates that the (p,n) reaction can serve as a precise probe to measure GT strength for light and medium weight nuclei.

Taddeucci et al., (Ta 81) define another convenient empirical ratio

$$\{R(E_p)\}^2 = \frac{\sigma_{GT}(0°)/|\langle GT\rangle|^2 K_{GT}(E_p)}{\sigma_F(0°)/|\langle F\rangle|^2 K_F(E_p)} \qquad 1.8$$

where $\sigma_{GT}(0°)$ and $\sigma_F(0°)$ are cross sections in the same nucleus for a 1^+ state with known $B_f(GT)$ and the IAS with $B(F) = N-Z$, respectively. In terms of the quantities in Equation 1.6

$$R(E_p) \simeq \left|\frac{J_{\sigma\tau}}{J_\tau}\right| (N^D_{\sigma\tau}/N^D_\tau)^{\frac{1}{2}}$$

$$K(E_p) = (E_f E_i/\pi^2)(k_f/k_i) \qquad 1.9$$

It has been found from DWIA calculations that at intermediate energies the distortion factor ratio is approximately independent of energy and has the value 1.2 ± 0.1 for GT and F transitions not widely separated in energy. The quantity $R(E_p)$ then represents roughly the ratio of interaction strengths $J_{\sigma\tau}/J_\tau$ at momentum transfer $q = 0$ but corrected for small distortion effects. Taddeucci et al., considered the variation of R with incident proton energy for several odd and even mass nuclei and found that $R \propto E_p$ to a good

Figure 1.1. Graphs of K, defined in Eq. 1.7 and deduced from the measured 0° (p,n) cross sections vs $\langle F \rangle^2$ and $\langle ME \rangle^2$. The top graph contains only the pure Fermi transitions while the lower graph contains the complete data set. Error bars on K reflect uncertainties in measured cross sections only. The transitions are labeled by specifying the target nucleus with the excitation energy in the final nucleus given in parentheses. The solid curves represent the fits to ^{26}Mg data, the dashed curves are the impulse approximation strengths, and the dot-dashed curve the one-pion-exchange-potential strength.
(Figure and caption from Goodman et al., (Go 80).

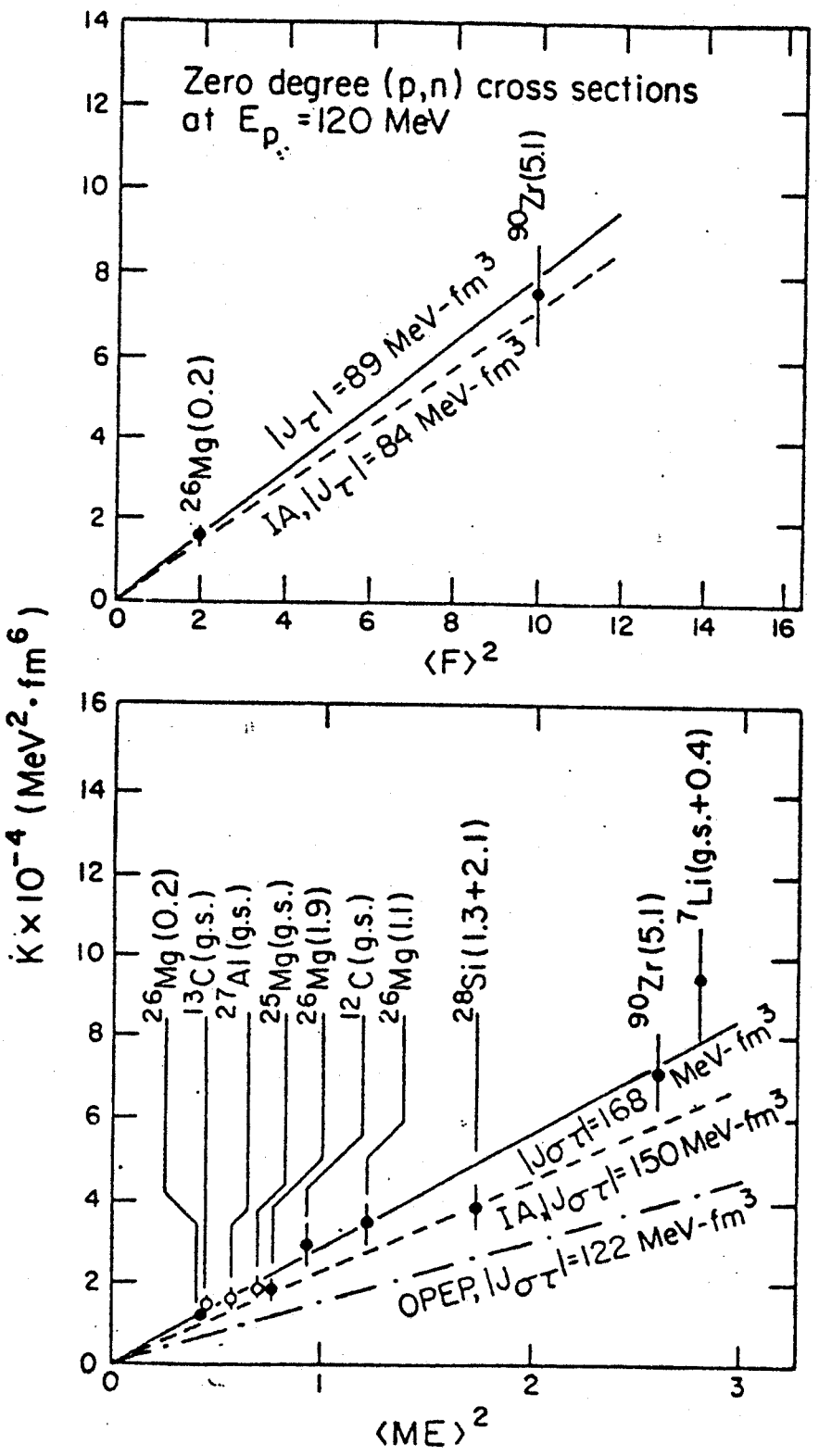
Zero degree (p,n) cross sections
at E_p = 120 MeV
^{26}Mg(0.2)
^{90}Zr(5.1)
$|J_\tau|$ = 89 MeV-fm^3
IA, $|J_\tau|$ = 84 MeV-fm^3
$\langle F \rangle^2$
$K \times 10^{-4}$ (MeV^2·fm^6)
^{26}Mg(0.2)
^{13}C(g.s.)
^{27}Al(g.s.)
^{25}Mg(g.s.)
^{26}Mg(1.9)
^{12}C(g.s.)
^{26}Mg(1.1)
^{28}Si(1.3+2.1)
^{90}Zr(5.1)
^{7}Li(g.s.+0.4)
$|J_{\sigma\tau}|$=168 MeV-fm^3
IA, $|J_{\sigma\tau}|$=150 MeV-fm^3
OPEP, $|J_{\sigma\tau}|$=122 MeV-fm^3
$\langle ME \rangle^2$

Figure 1.1

approximation above $E_p = 60$ MeV. Figures 1.2a and 1.2b show the data that they used and the linear fit to the data. For example, at 120 MeV, $R = 2.19$. This linear and model independent relation can be used to compute GT strengths from (p,n) reactions at 120 MeV with an accuracy only slightly worse than that of the cross section measurement i.e., 20%. One simply compares the IAS cross section with the 1^+ state of interest and applies Equation 1.8. Note that such a determination is independent of calibration transitions, cross section normalizations, and DWIA mass dependent extrapolations. Hence, this method has a particular simplicity and we use it exclusively.

Some measurements have already been made of GT strength from (p,n) reactions on ^{40,42} and ^{48}Ca at 160 MeV, (Ga 81,An 80); but the current work is more complete and includes a ^{44}Ca target; it will serve as a parallel to the electron scattering studies of Steffen et al., (St 80). The measured B(GT) is compared to the simple sum rule prediction to determine the quenching of the spin dependent operator $\sigma\tau^-$. In recent work on heavier nuclei, roughly 0.6 ± 0.1 of the sum rule strength was seen. This has been interpreted as evidence for the coupling of the nucleon to the Δ isobar ($T = T_z = 3/2$, $S = 3/2$) by several authors (Os 79, Go 82, Ra 82, Ga 82, Bo 82). There seems to be some evidence from pion inelastic scattering also that such a coupling exists (Mo 82). Calculations including this coupling to the spin-isospin degrees of freedom of the nucleon suggest that roughly 65%

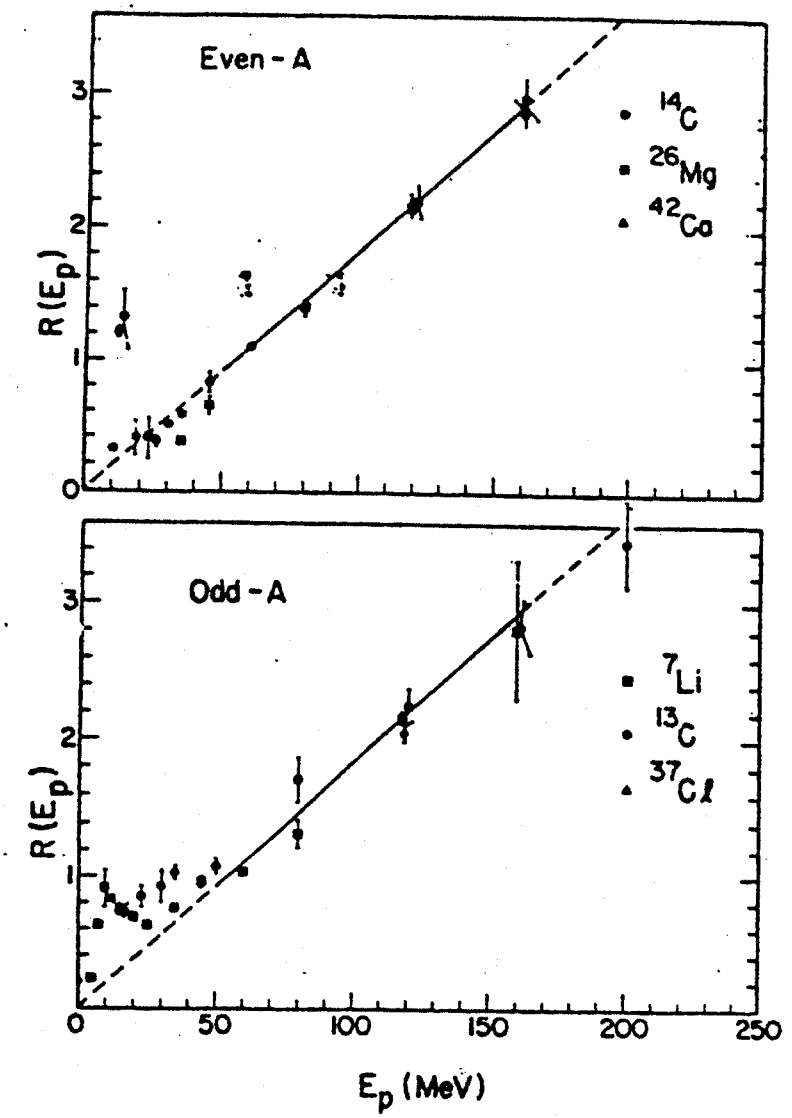

Figure 1.2. The empirical quantity $R(E_p)$ for odd- and even-A targets. The solid line represents the average value $R(E_p)/E_p = (54.9 \pm 0.9 \text{ MeV})^{-1}$ determined from the even-A target data for bombarding energies $E_p \geq 50$ MeV.

(Figure and caption from Taddeucci et al. (Ta 81).)

of the classical strength should fall in the nuclear excitation region for ^{208}Pb (Ga 80). Sagawa used the constituent quark model to calculate the isobar-hole coupling matrix element and finds that the combined effects of RPA correlations and particle-hole coupling decrease the transition strengths of M1 and GT states by about 35% (Sa 82). If true, all the above observations point towards a significant coupling of the nucleon structure to nuclear structure.

However, the work of Bertsch and Hamamoto, including 2p-2h states for ^{90}Zr, indicates that the strong tensor force shifts the strength to between 10 and 45 MeV excitation (Be 82). Yet another approach to the problem of spin-isospin excitations in terms of a unifying response function by Ericson suggests that at low momentum, in addition to creating a collective mode, the strong repulsive ph force, also produces a quenching of the GT strength due to a Lorentz-Lorentz effect similar to that of electromagnetism (Er 82). Microscopic background calculations for (p,n) reactions on ^{40} and ^{48}Ca at 160 MeV, carried out by Osterfeld imply that a significant part of the missing 1^+ strength is contained in what is conventionally taken as an experimenter's background and this accounts at least partly for the larger values of the observed quenching of the spin dependent operators earlier deduced from (p,n) reactions (Of 82). Thus the precise amount of quenching may bear importantly on the question of the number of degrees of freedom in the nuclear wave function. In the present work, an attempt has

been made to verify the last of the above hypotheses as will be discussed in Chapter IV.

Finally, one notes that these results may have substantial applications. The GT strength is a measure of the degree to which nucleons are unpaired in the ground state of a nucleus. The measured strength for ^{40}Ca should therefore be useful for an estimate of the same. The present study also verifies a recent claim that the analog of the 10.3 MeV state in ^{48}Ca is significantly wider than the parent state (An 80). The energy systematics seen in this study seem to indicate what was already noted by Bertsch--i.e., one does not expect pion condensation in nuclei (Be 81). The width of the GT strength function is a necessary input in calculations of stellar nucleosynthesis. In the gross theory of β decay, Takahashi et al., use the mean energy of GT strength to be degenerate with the IAS which is not quite right and use a width of 10 MeV, much larger than seen in (p,n) reactions (Tk 73). Redoing these calculations using the mean energy and width of the GT strength values as suggested by the current (p,n) reaction studies might improve our understanding of the r-process nucleosynthesis. Further, GT matrix elements are of considerable importance in computing weak decay rates in supernovae (Fu 80). We hope that the current measurements will therefore, aid in calculations of reaction rates in these stages of stellar evolution and nucleosynthesis.

The organization of this thesis is as follows: Chapter

II contains a description of IUCF and the neutron time of flight apparatus. Methods of data acquisition and reduction are described in Chapter III. An analysis using DWBA 79 and interpretation of our results are given in Chapter IV. A summary of our findings is given in the concluding Chapter V. The simple sum rule quoted earlier is derived in Appendix A. Plots of energy calibrated spectra for all the four targets at the three angles measured (0°, 6.3°, and 11.1°) are shown in Appendix B. Neutron detector efficiencies are listed in Appendix C. Appendix D contains Tables giving the details of the computation of the GT strength.

of the classical strength should fall in the nuclear excitation region for ^{208}Pb (Ga 80). Sagawa used the constituent quark model to calculate the isobar-hole coupling matrix element and finds that the combined effects of RPA correlations and particle-hole coupling decrease the transition strengths of M1 and GT states by about 35% (Sa 82). If true, all the above observations point towards a significant coupling of the nucleon structure to nuclear structure.

However, the work of Bertsch and Hamamoto, including 2p-2h states for ^{90}Zr, indicates that the strong tensor force shifts the strength to between 10 and 45 MeV excitation (Be 82). Yet another approach to the problem of spin-isospin excitations in terms of a unifying response function by Ericson suggests that at low momentum, in addition to creating a collective mode, the strong repulsive ph force, also produces a quenching of the GT strength due to a Lorentz-Lorentz effect similar to that of electromagnetism (Er 82). Microscopic background calculations for (p,n) reactions on ^{40} and ^{48}Ca at 160 MeV, carried out by Osterfeld imply that a significant part of the missing 1^+ strength is contained in what is conventionally taken as an experimenter's background and this accounts at least partly for the larger values of the observed quenching of the spin dependent operators earlier deduced from (p,n) reactions (Of 82). Thus the precise amount of quenching may bear importantly on the question of the number of degrees of freedom in the nuclear wave function. In the present work, an attempt has

II. Experimental Techniques

The electric charge neutrality of the neutron does not permit conventional detection techniques, using magnetic spectrographs and solid state detectors. Neutrons can only be detected by the charged particle recoils, or the charged reaction products produced when they scatter from, or react with other nuclei. Although the energy signals thus produced are not proportional to the neutron energy, the time of emission of these signals in the detector relative to a fixed time reference is proportional to the time of flight, which in turn, defines the neutron velocity, and hence, the neutron energy. Thus, precise time signals and long flight paths are required in high precision neutron spectroscopy.

Quantitatively expressed, neutron energy E, neutron velocity v, time of flight t, and the path length L are related as

$$\begin{aligned} E &= M_n c^2 \left(\frac{1}{2}\frac{v^2}{c^2} + \frac{3}{8}\frac{v^4}{c^4} \ldots\right) \\ t &= L/v \\ E &\cong M_n c^2 \left(\frac{1}{2}\frac{L^2}{t^2 c^2} + \frac{3}{8}\frac{L^4}{t^4 c^4}\right) \end{aligned} \tag{2.1}$$

where $M_n c^2$ is the rest mass energy of the neutron.

In the nonrelativistic limit, energy resolution and time resolution are therefore, related as

$$\Delta E \cong \frac{2^{3/2}}{M_n^{1/2}} \frac{E^{3/2}}{L} \Delta t \tag{2.2}$$

Note that this is a lower limit on ΔE. The different factors contributing to Δt are electronic, beam bunch width, scintillator transit time, target energy loss and straggling, beam energy spread, kinematic broadening, and intrinsic state width. One way to improve energy resolution is to increase the flight path with a consequent loss in count rate $\propto L^{-2}$. Using large detectors can compensate partly for count rate loss; but then, scintillator transit time causes a major loss of time resolution unless one compensates for it by other means. At the Indiana University Cyclotron Facility (IUCF) where the experiment was carried out, typical proton pulse widths are 0.5 nsec. Using large volume scintillators and a time compensation technique described later in this chapter, Goodman et. al., have achieved subnanosecond resolution for 100 MeV neutrons (Go 79). To get an estimate of the pathlength involved, note from Equation 2.2 that for Δt=1 nsec, roughly a 115 meter long flight path is required for an energy resolution of 300 KeV for 115 MeV neutrons. With these limitations, the major technical problems associated with neutron spectroscopy are the need for (a) a beam swinger (b) large detectors and (c) a stable stop signal.

(a) Beam Swinger: It is not very practical to move detectors around the target to measure angular distributions, when the flight path is long. This requires not only large space, but also very carefully placed shielding along the flight path to insure that the detector sees only neutrons from the target. It is easier to change the direction of the incident beam on the target. The floor plan of the experimental areas at IUCF are shown in Figure 2.1. The neutron station is located at the northern end of the laboratory. The remoteness of this location allows one to set up long flight paths with little inconvenience to and

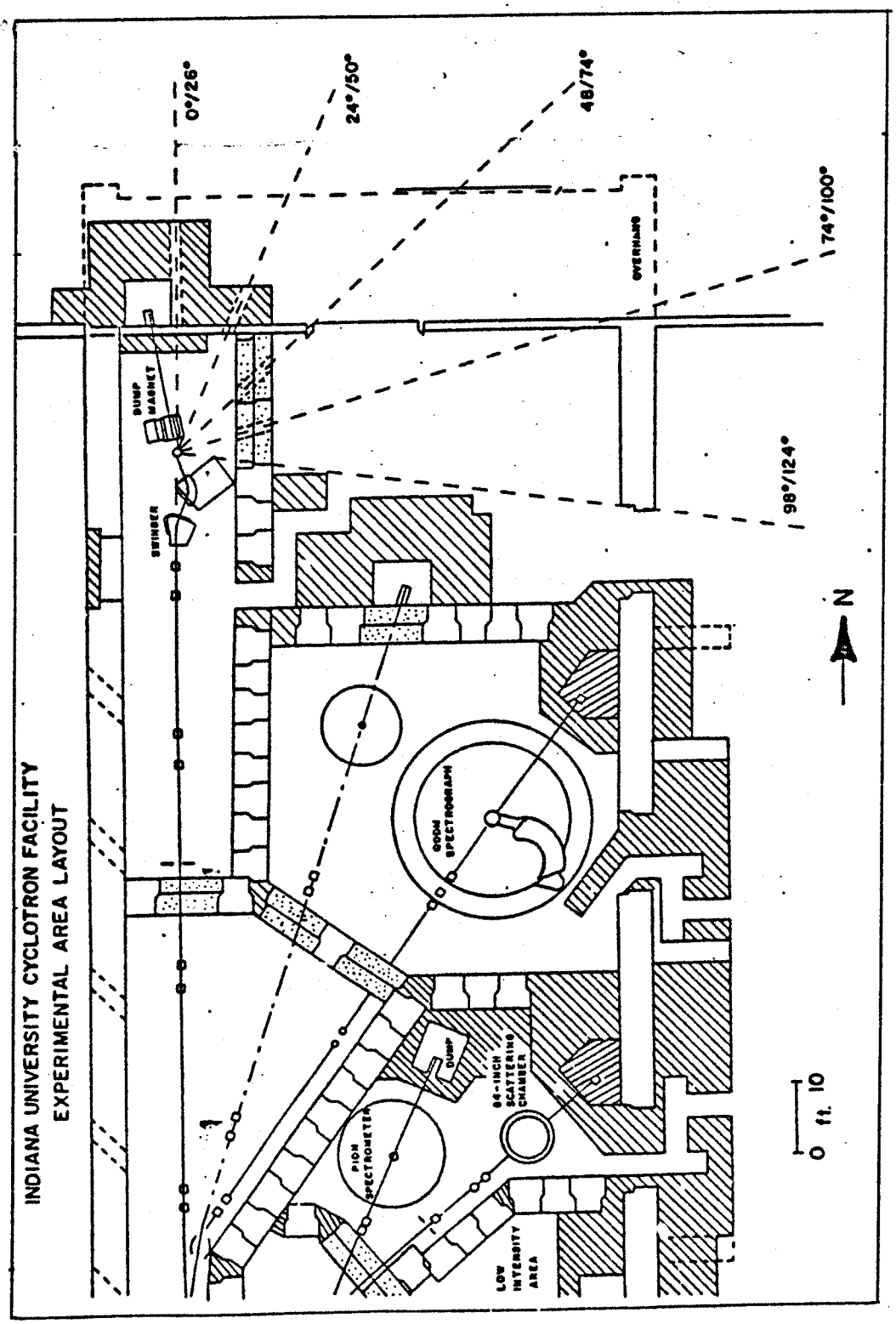

Figure 2.1. Floor plan of experimental areas showing locations of the new pion spectrograph, beam swinger magnet and neutron time-of-flight area. (Figure and caption from IUCF Annual Report 1977-78.)

from other sections of the laboratory. A major feature of the neutron station is a beam swinger using three fixed magnets that enables one to change the angle of incidence of the beam on the target; for a fixed flight path, this is equivalent to changing the effective reaction angle. Figure 2.2 illustrates the geometry. The first magnet bends the beam away from its original path, the second magnet bends it back towards the target. The pole faces of the second magnet are large enough to accept a range of paths that impinge on the target at a range of angles. The third magnet steers the beam into a dump. With the use of the third magnet, the beam dump can remain fixed, as the angle is varied. This feature is particularly useful at high energies, when massive shielding is required around the beam dump to keep the neutron background low. It also makes possible observations at 0°, where L=0 spin flip processes dominate.

In the NTOF system currently in use at Indiana, the angular range on target of incident protons is 26°. The scattering angle θ is determined by the radii of curvature of the beam protons in the two magnets, $\rho_1(\theta)$ and $\rho_2(\theta)$. Thus, to set the system for a given angle, one sets the fields B_2 and B_1 to correspond to the magnetic rigidity of the incident particle. The angle is then measured more precisely by centering the beam on a motor driven slit that pivots around the target position. The slit is used only when the beam is being focused and the angle measured and is retracted during data runs to avoid neutron background from it. Since the scattering plane is horizontal one can have multiple paths with all detectors at ground level. Currently, there are three time of flight lines covering angular ranges of $0\text{-}26^{\circ}$, $24\text{-}50^{\circ}$,

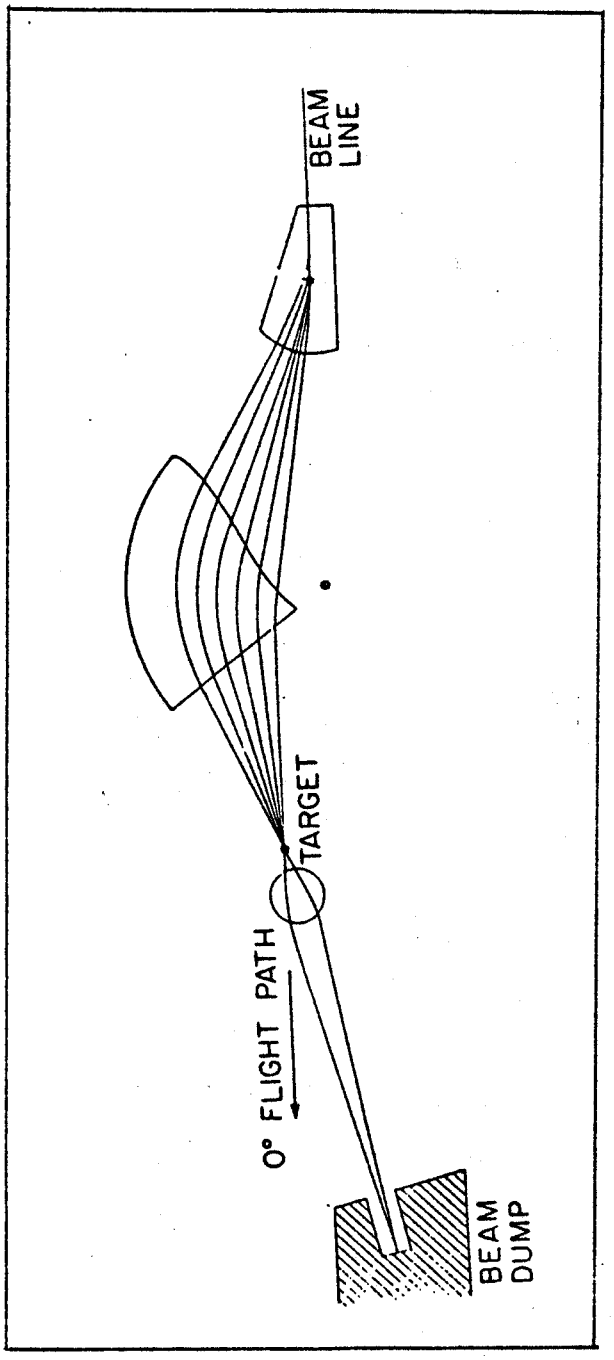

Figure 2.2. Magnet layout for beam swinger.
(Figure from Goodman et al., (Go 79).)

and 45-71°. The detectors are housed in huts that can be moved with a fork lift and placed at the desired locations.

(b) Detectors: To get an idea of the size of the detectors needed for our purpose, note that for a solid angle of 1 msr (typical for a solid state detector of area 50 mm^2 at a distance of 22 cm and therefore, a comparable count rate assuming same efficiency of detection), a neutron detector at a distance of 100 meters from the target has to have an area of 10 m^2. A second consideration is that neutron detectors are not 100% efficient. These two effects point in the direction of large detectors. In a large scintillator (>10cm in any dimension), there is some loss of time resolution because (i) the measured time of detection of a neutron depends on the position at which the scintillation event occurs; and (ii) the spatial distribution of the light on the photocathode is different for scintillations occuring at different points in the scintillator. The resulting loss of time resolution can be reduced if one arranges to determine the position of scintillation and applies a correction later. Alternately, a time compensation technique can be used.

At IUCF, Goodman et. al., have employed a geometric approach to time compensation (Go 78a, Go 78b, Go 79). The detector axes are tilted relative to the incident neutron direction such that the neutron and photon transit times are independent of the position at which the scintillation occurs. As can be seen from Figure 2.3, the time of arrival of a photon at the phototube from a scintillation occuring at coordinates x,y in the scintillator is

$$t(x,y,\beta,\theta) = t_0 + \frac{nL}{c\cos\theta} + \frac{x}{c}\left(\frac{\cos\phi}{\beta} - \frac{n}{\cos\theta}\right) + \frac{y}{c}\frac{\sin\phi}{\beta} \qquad (2.3)$$

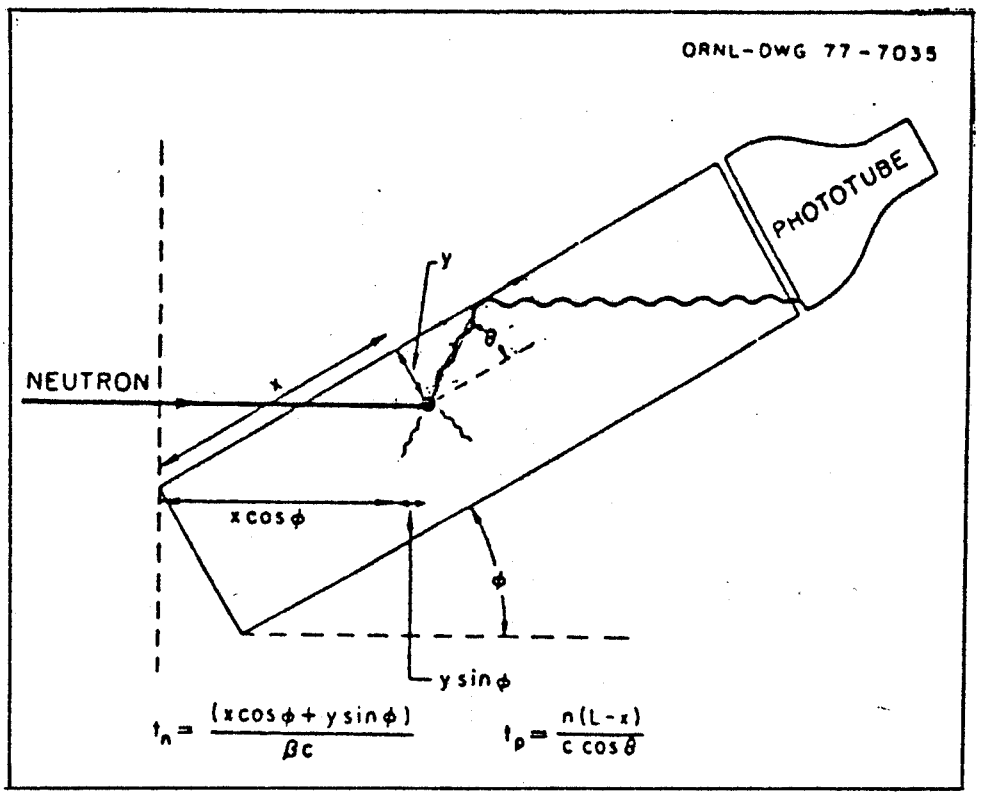

Fig. 2.3. This figure shows the geometrical parameters of time compensation. β is the ratio of neutron velocity to the velocity of light. c is the velocity of light. n is the index of refraction of the scintillator. t_n is the transit time of the neutron and t_p is the transit time of the light (photon). L is the length of the scintillator. (Figure and caption from Goodman et al., (Go 78b).)

where t_0 is the neutron time of flight up to the scintillator and other variables are defined in the figure caption. What one would like to achieve by time compensation is to make t nearly independent of x and y for a given neutron energy i.e., a given value of β. It is assumed that the light is emitted isotropically. Light emitted with $\theta > \theta_{max}$ (limiting angle for total internal reflection) is lost. For an index of refraction n = 1.58, $\theta_{max} = 51^{\circ}$. The time equation then implies that light from an instantaneous flash will arrive at the phototube over a period from $t(x,y,\beta,\theta = 0^{\circ})$ to $t(x,y,\beta,\theta = 51^{\circ})$. In a real scintillator, the light is not emitted instantaneously; it follows an exponential decay curve with a characteristic decay time which for example, is 2.4 nsec for NE 102 scintillator. This is dominant in determining the light curve at E_n = 100 MeV. Note that the light profiles illustrated in Figure 2.4a exhibit varying risetimes as well as varying amplitudes, (due to random scattering angle in the neutron reaction). Constant fraction timing can only compensate for variations in amplitudes. A form of extrapolated zero timing is employed at IUCF to compensate for varying risetimes.

The principle behind this method is as follows: The pulse shape of the signal from the photocathode is found to have a parabolic shape near the origin, represented by

$$A(t) = A_0((t-t_0)/\tau)^2 \qquad (2.4)$$

where t_0 is the origin of the light pulse and both A_0 and τ vary. The objective is to determine t_0, as marked in Figure 2.4b. Define two

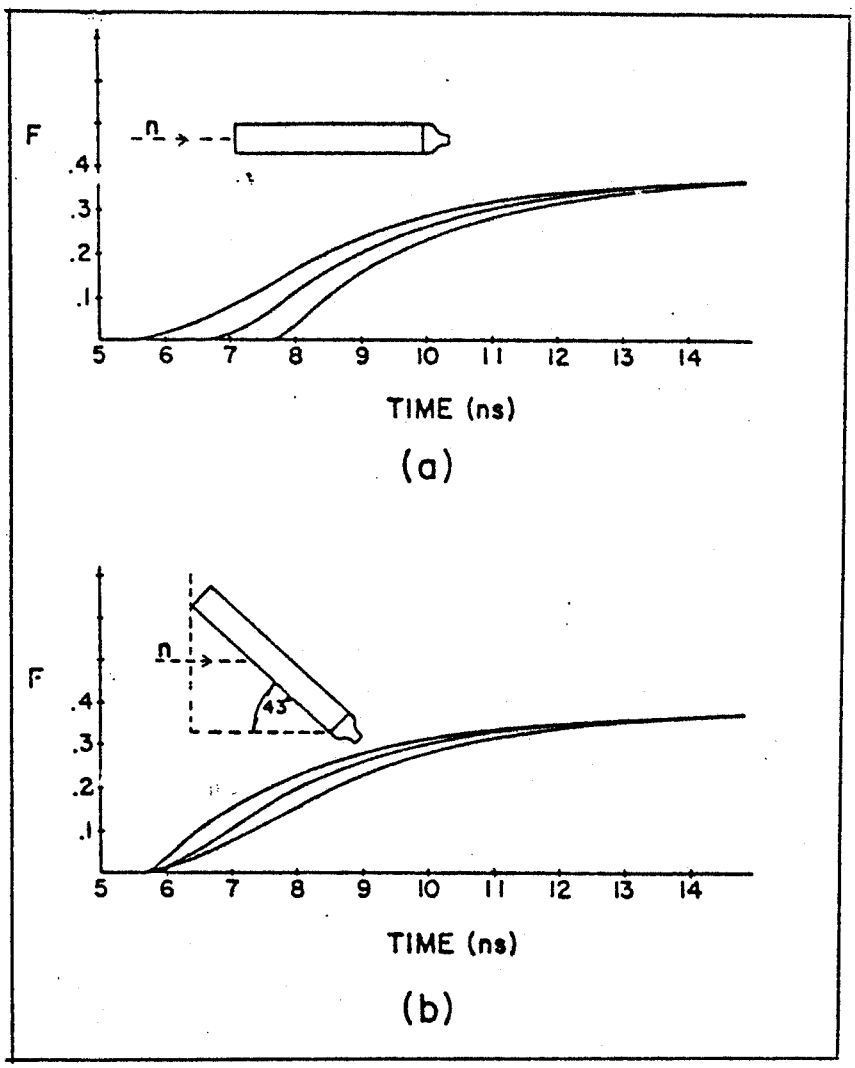

Figure 2.4

(a) The curves show the fraction of forward emitted light that has reached the phototube by time t, measured from when the neutron crosses the plane through the front face of the scintillator. The parameters used are: length of scintillator = 1 m, index of refraction = 1.6, phosphor decay constant = 2.4 ns, neutron energy = 100 MeV. The three curves are for scintillations at the front, middle and back of the scintillator.

(b) This shows how time compensation is achieved by tilting the scintillator. The calculation is the same as for Fig. (a) except for the tilt.
(Figure and caption from Goodman et al., (Go 79).)

amplitudes A_1 and A_2, such that the corresponding times t_1 and t_2 satisfy

$$t_1 - t_0 = t_2 - t_1 = (t_2-t_0) - (t_1-t_0) \qquad (2.5)$$

Set up two discriminators with thresholds at A_1 and A_2 to start two time to amplitude converters (TACs) and measure $(T-(t_1-t_0))$ and $(T-(t_2-t_0))$, the stop time T being provided by the cyclotron rf to be described later. Subtracting the output of the second TAC from that of the first yields t_2-t_1; with our choice of A_1 and A_2, this is exactly the origin of time. Thus, if Equation 2.4 is a valid approximation to the portion of the pulses sensed by the discriminators, the required amplitude ratio A_2/A_1 can be shown to be 4. Then the tilt angle should be chosen to line up the the origin of the pulses and extrapolated zero timing should be used with $A_2/A_1 = 4$. Figure 2.4b shows how tilting the detectors lines up the origins of the pulses.

It can be seen that time compensation is exact for neutrons of a particular energy only, because the tilt angle to accomplish it is derived from β, the neutron velocity (Equation 2.3). Calculated tilt angles vs. neutron energy for axial light rays are shown in Figure 2.5. In an experimental set up with long flight paths, one is far from having axial light rays; therefore, the tilt angle is determined by trial and error. A known sharp line is obtained from a known target. On line analysis gives the FWHM of this peak in the TOF spectrum. Tilt angle is changed until the highest resolution is obtained. At IUCF, a triple discriminator is used with levels 2 and 3 set for amplitudes A_1 and A_2 defined earlier. See Figure 2.7. Level 1 (the lowest threshold) is set as high as 1/4 to 1/2 of the maximum neutron energy because the flight

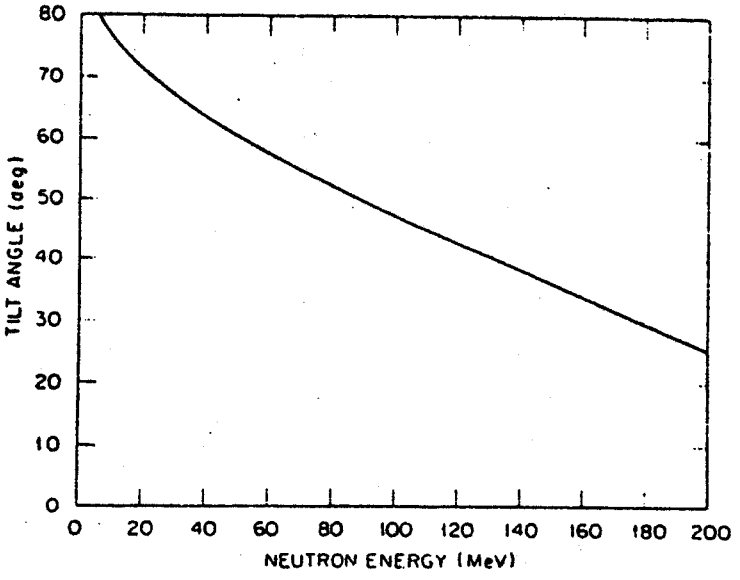

Figure 2.5. This shows the required tilt angle ϕ, as a function of neutron energy to achieve exact time compensation for the axial light rays. (Figure and caption from Goodman et al., (Go 78b).)

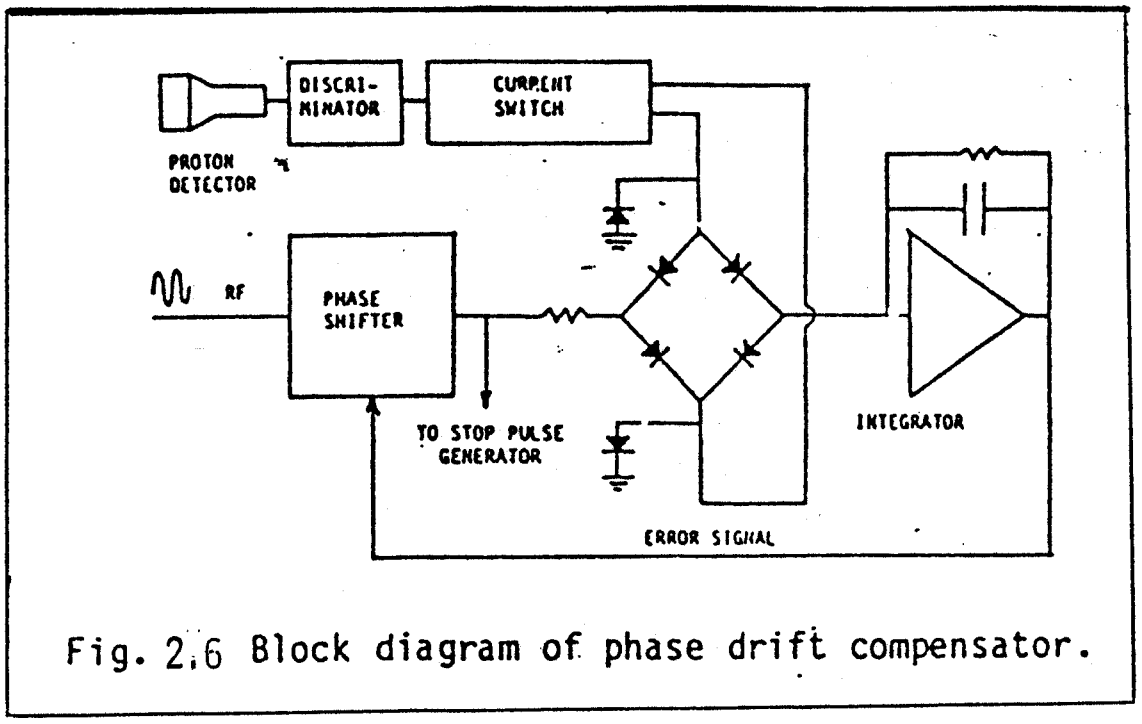

Fig. 2.6 Block diagram of phase drift compensator.

Figure and caption from Goodman et al.,(Go 79).

time of neutrons at that fraction of the energy becomes greater than the separation of the beam pulses, and neutron spectra from adjacent bursts would overlap if the threshold were set lower.

(c) RF Timing with phase drift compensation: A precise timing signal for STOP input to the TACs can be derived from the cyclotron rf signal. The Indiana cyclotron is a three stage system consisting of an ion source, a preaccelerator cyclotron and a main stage cyclotron. Under normal operating conditions, there are 4 to 6 bunches per orbit in the cyclotrons. Since the time separation between the bunches is too small for TOF studies with long paths, one bunch per orbit is selected, with the help of a pulse selector and a buncher located on the beam line between the ion source and the first cyclotron. The beam is swept across an aperture in a circle with a subharmonic of the cyclotron frequency, f. One uses 3/4 f or 5/6 f to achieve 1 of 4 or 1 of 6 selection respectively. The reference time for the TOF system is taken from a phase coincidence between the f signal from the cyclotron master oscillator and the subfrequency. If the magnetic fields on the cyclotrons were stable, the proton transit time through the accelerator system would be constant and the stop signal would be stable. In practice, small phase drifts of the order of a few nanoseconds occur between the accelerating voltage and the proton bunches and compensation is necessary for good time resolution.

The phase compensation method devised by Goodman et al., is illustrated in Figure 2.6. Protons elastically scattered from the target are detected with a fast scintillation counter located along a 12^{o} line with respect to the undeflected incident beam. The proton signal is set to trigger a discriminator which generates a pulse with a

width of about 1/2 the rf period. This pulse opens the current gate of a diode bridge. If the opening time is centered about the crossover point of the rf sine wave, then the net charge passing through the gate is zero. If there is a phase drift, this net charge is nonzero, being positive or negative, depending on the direction of the drift. The integrated output of the gate is a measure of the phase drift and is used as an error signal into a phase shifter that shifts the phase of the rf signal going to the stop pulse generator.

The standard electronics employed at IUCF by Goodman et. al., for NTOF studies is shown in Figure 2.7. To obtain the highest resolution, the tilt angle was varied to optimize the peak to valley ratio of the barely resolved states in the $^{7}Li(p,n)^{7}Be$(g.s., 0.429 MeV) reaction. Level 1 was set at nominally 10 times the Compton edge from ^{228}Th. Total charge was measured by split Faraday cups at the end of the third magnet in the neutron station. The other details of data acquisition are described in Chapter III.

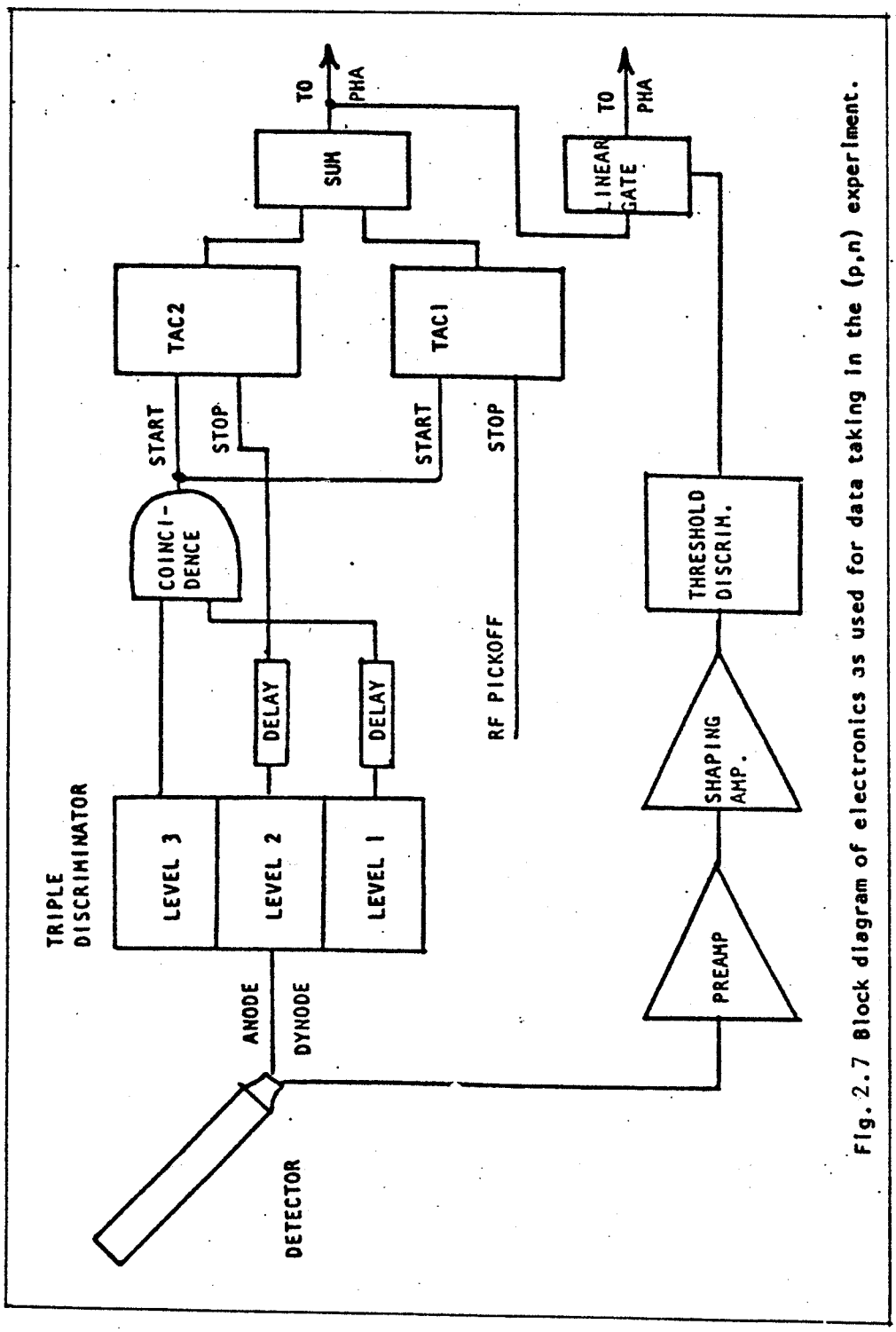

Fig. 2.7 Block diagram of electronics as used for data taking in the (p,n) experiment.

Figure and caption from Goodman et al.,(Go 78a).

III. Data Acquisition And Reduction

The experiment was carried out at the IUCF with a 119.3 MeV proton beam. Beam energy was obtained from the calibration of the beam analysis system. The targets (^{40,42,44} and ^{48}Ca, ^{7}Li, and ^{12}C) were loaded on the ten position Geneva drive target ladder at the beam swinger. This target drive was remotely controlled through the Sigma-2 cyclotron controls computer. The targets were protected from oxidizing by the vacuum interlock of the target drive. The 0^{o} flight path from target to center of detector was 131.52 meters long. The cyclotron rf was 28.72 MHz. With a 1 in 4 pulse selection, this corresponds to a beam repetition period of 139.3 nsec. Target information is summarized in Table 3.1. Four large volume plastic scintillators

Table 3.1 Target Information

Target	Thickness (mg/cm^2)	Purity (Percentage)
^{40}Ca	29.2±0.3	99.965
^{42}Ca	30.5±0.5	93.60
^{44}Ca	28.5±0.5	98.68
^{48}Ca	28.5±0.5	97.30
^{7}Li	43.1±0.3	99.99
^{12}C	34.9±0.5	99.99

and two anticoincidence paddles (to veto cosmic rays) were arranged in the 0^{o} hut as shown in Figure 3.1. The scintillators were coupled to 5" phototubes with tapered light pipes at both ends. Another scintillator was housed in the 24^{o} hut at a distance of 39.0 meters from the target, and data were accumulated, but were not used in the analysis. A

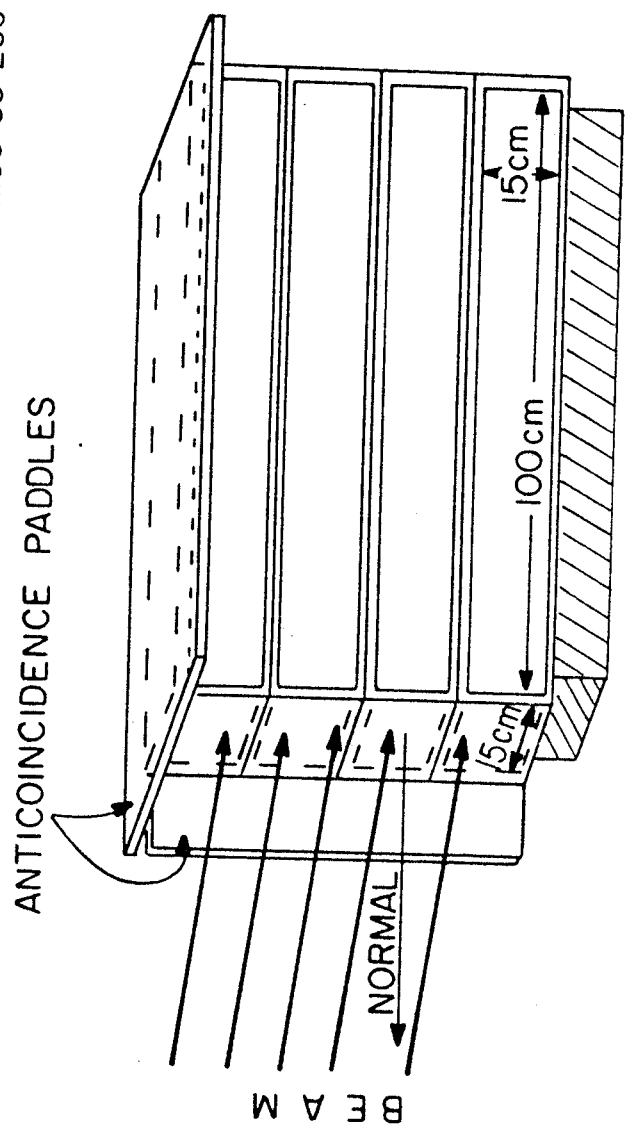

Figure 3.1. Arrangement of detectors in the 0° hut.

hardware threshold of nominally 23.8 MeV electron energy (10 times the Compton edge of the 2.61 MeV gamma ray from a ^{228}Th source) was used. If the detector had infinite resolution, then the Compton edge would be seen as a sharp structure in the spectrum; the finite resolution of the detector smears this edge with a Gaussian shape. Computations have been carried to measure the position of the actual Compton edge relative to the peak of this Gaussian distribution as a function of the resolution (Ta 82, Ga 83). It was found that the detector resolution was 25% at the energy of interest. This yields the position of the Compton edge as 0.93 times the position of the half maximum point of the peak in the spectrum. Additional software thresholds of nominally 17, 23, and 28 times the ^{228}Th Compton edge were set within the IUCF data acquisition program DERIVE. We refer to the spectra by these as labels. An off-line analysis of the spectra from the ^{228}Th source yielded values about 10% higher than these corresponding to thresholds of 11.0, 18.7, 25.3, 30.8 times the ^{228}Th Compton edge. In equivalent neutron (proton) energy the thresholds were therefore at 32.6, 50.7, 65.9, and 78.4 MeV respectively (An 79). The total incident charge, total number of events within each detector, and total number of events vetoed were registered by scalers. The time resolution achieved was 1.5 nsec, corresponding to an energy resolution of 330 KeV, at the best.

The ^{7}Li and ^{12}C targets were used for purposes of cross section normalization. These two targets were the first to be measured at 0^{o}; the unresolved states in ^{7}Li(p,n)^{7}Be(g.s.+0.429 MeV) were used to determine the best tilt angle. Next, the calcium spectra were taken at 0^{o}; calibration runs with ^{7}Li and ^{12}C were repeated at the end of the 0^{o} runs. Following this, background due to cosmic rays was measured for

about 24 minutes. Then measurements were made with the calcium targets at 6.3^{o} and 11.1^{o}. Beam current was maintained between 200 and 400 namp.

1. Determination of centroid shifts for energy bands and choice of threshold for analysis

Loss of time resolution results primarily from (a) variation in risetimes of pulses and (b) variation in amplitudes of pulses. As discussed in Chapter II, the method of extrapolated zero timing is used to compensate for timing errors due to variation in risetimes of pulses. The amplitude dependent 'time walk' was minimized by breaking the observed range of pulse heights into bands defined by the threshold settings and evaluating the necessary shifts using a standard peak. The raw TOF data are in the form of 1024 channel spectra; there are 16 of them--four thresholds for each detector and four detectors. For example, for detector 1, the TOF spectra corresponding to the 4 thresholds are stored in arrays 1,5,9 and 13 with array 1 containing the data for the lowest threshold and 13, that for the highest. First, channel by channel difference spectra of these arrays i.e. 1-5, 5-9 and 9-13 are obtained. This is done for all the 0^{o} runs. Then a sharp peak is chosen in each target and its centroid found in each of the energy bands 1-5, 5-9, 9-13 and array 13. The centroid shifts of the higher bands relative to the lowest band 1-5 are determined. The results for different targets are then averaged to obtain the final band shifts for detector 1. The procedure is repeated for detectors 2, 3, and 4. Table 3.2 displays the results. Next the bands were added channel by channel with appropriate shifts. Data from detectors 2, 3 and 4 were then added to that of detector 1 with the necessary shifts. One thus obtains the

Table 3.2. Energy Band Centroid Shifts (in Channels)

Detector #	Band 1 10xTh to 17xTh	Band 2 17xTh to 23xTh	Band 3 23xTh to 28xTh	Band 4 28xTh and above
1	0[a)]	2	4	5
2	18	20	22	23
3	34	36	38	39
4	18	21	23	25

a) Taken as reference position.

Note: The threshold settings quoted here are only nominal. Exact settings inferred from detailed analysis are 11.0, 18.7, 25.3 and 30.8 times the ^{228}Th Compton Edge.

final TOF spectra for all targets and all angles including the cosmic ray run. Figure 3.2 shows the results for 0^{o} runs for the ^{40,42,44} and ^{48}Ca targets.

2. Cosmic ray and foldover neutron background contributions and subtraction

Cosmic ray events were partially vetoed by the arrangement of the anticoincidence paddles marked in Figure 3.1, but some background remains. This can be seen from the cosmic ray spectrum measured between the 0^{o} and 6^{o} runs. In the absence of any major transient phenomena occuring on the Sun during our runs, it can be assumed that the diurnal variation of the muon component of the cosmic ray background is negligible (Wi 76); therefore it is possible to correct for the different counting times and subtract the cosmic ray background from the TOF spectra.

The low counting rate for the cosmic ray background combined with the brief counting time (1441 seconds) resulted in relatively large statistical uncertainties for all the thresholds except the lowest one. In addition, examination of the cosmic ray spectra revealed that the TAC had a nonlinear response for channels <290. To treat these effects, we first obtained average counts by summing over every 50 channels. Figure 3.3 shows the cosmic ray spectrum for the lowest threshold, with the open circles representing the averages over 50 channels. It can be seen that the TAC is linear for channels >300. There are 500 channels in this region which we define as the flat portion of the cosmic ray spectrum. The weighted average of the flat portion was obtained for each threshold. Next, the region of the spectrum between channels 100 and 250 was examined for the lowest threshold (11xTh case) and a

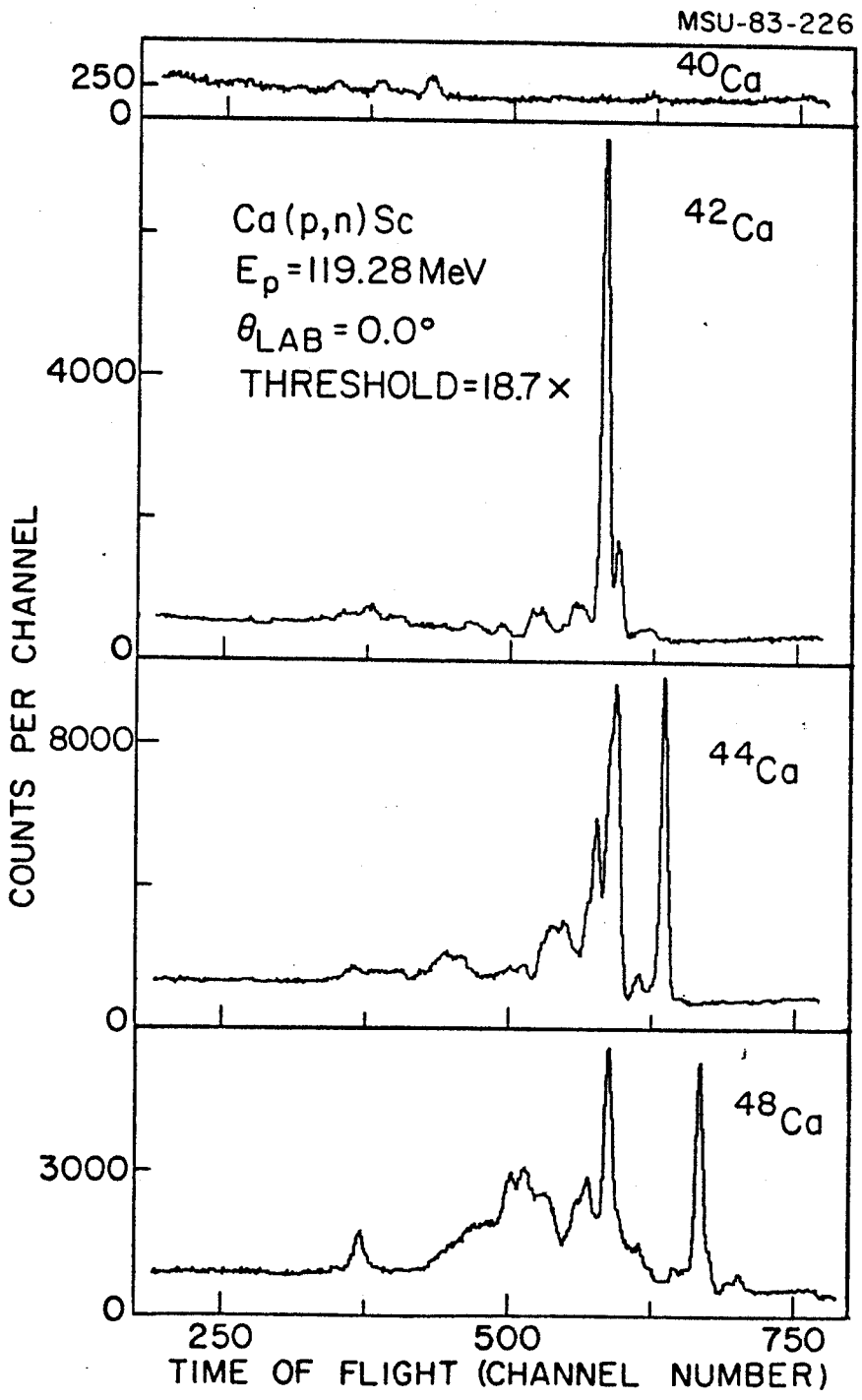

Figure 3.2. Time of flight spectra for ^{40,42,44} and ^{48}Ca (p,n) at 0°.

straight line approximation obtained. The two regions, channel >250 and channel <250, were joined smoothly for the 11x case where the statistics are good. The higher threshold spectra were obtained by scaling down the 11x spectrum using as scale factor, the ratio of the flat portion of the spectrum to that of the 1x case. Poor statistics made it impossible to obtain reliable TAC nonlinearities directly from these spectra. Figure 3.4 shows the averaged cosmic ray spectrum for the lowest threshold. These spectra were then time normalized and subtracted from the TOF spectra for the different targets.

In neutron time of flight studies using a pulsed beam, there exists the problem of slow neutrons from a certain beam burst and fast neutrons from the next burst arriving at the detector at the same time. To minimize this slow neutron background, the foldover neutron background, one has to set the hardware threshold fairly high; in our case, this was set at roughly 36.0 MeV neutron energy. The dynamic range of 120 MeV neutrons at a distance of 130 meters for pulsed beam of period 139 nsec is approximately 32.0 MeV. This means that to avoid the foldover background completely one has to have the hardware threshold of at least 88 = (120-32) MeV. But this will reduce the count rate severely. As a compromise, software thresholds between 50.0 and 80.0 MeV neutron energy were set within the data acquisition program; the plan was to accumulate all the data, and decide on a proper choice of threshold for analysis at a later time. Offline analysis of the data revealed that the foldover neutron background can be eliminated by extrapolating the TOF spectrum from below the ground state to higher excitation energies and subtracting it. This was done by examining the foldover neutron behavior in 6^{o} and 11^{o} spectra of the $^{40}Ca(p,n)^{40}Sc$ reaction which has a

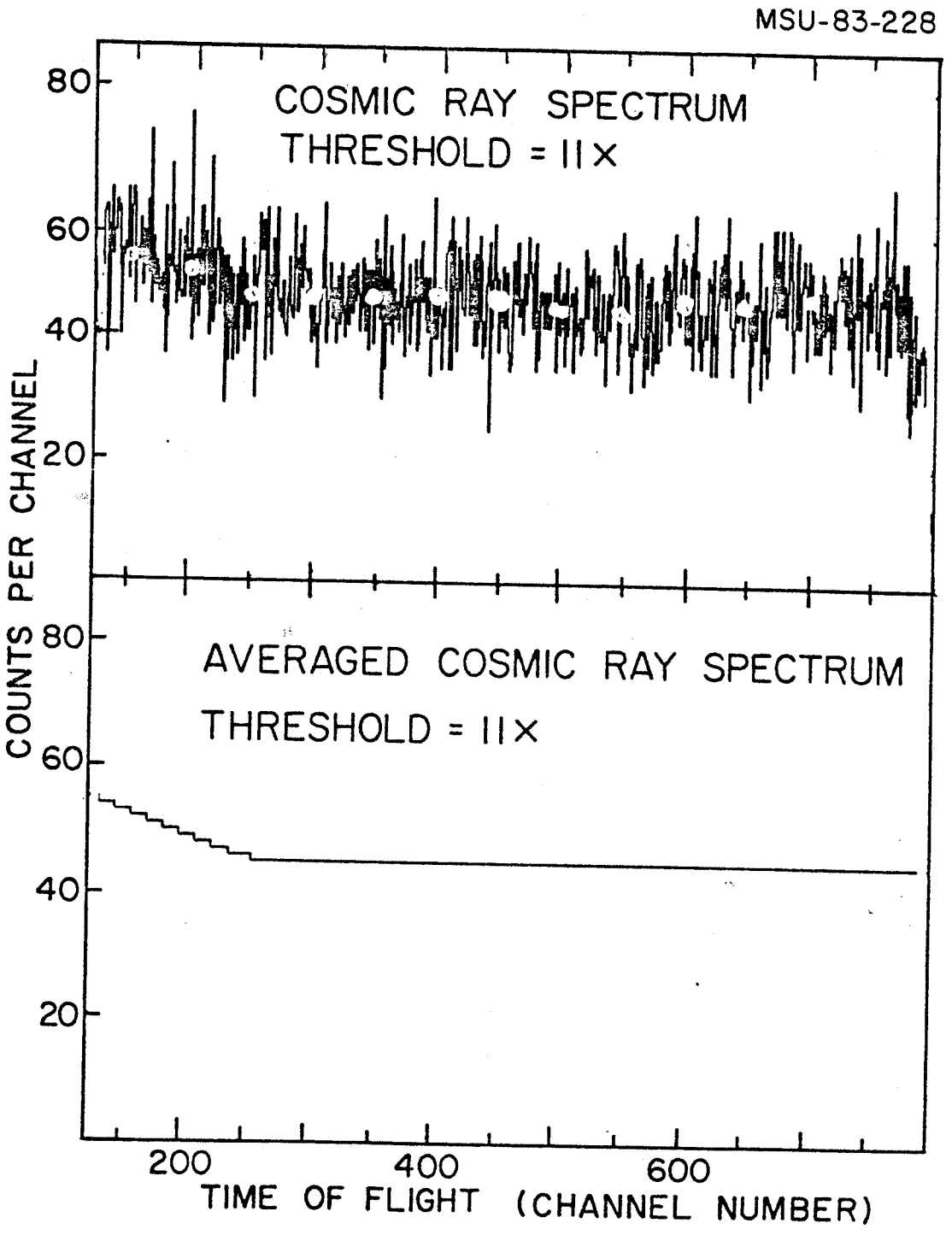

Figure 3.3 (top). Cosmic ray spectrum (data)

Figure 3.4 (bottom). Cosmic ray spectrum (average)

large negative Q value and using this to guide the extrapolation in the case of the other calcium targets. The 0^{o} spectrum from $^{40}Ca(p,n)^{40}Sc$ which would have been ideal for this purpose had additional peaks arising from a leakthrough beam burst and could not be used. The foldover background thus obtained for the 0^{o} ^{40}Ca run was found to be selfconsistent. Figure 3.5 shows $^{44}Ca(p,n)$ spectra at 0^{o}, with the foldover background indicated. The errors accumulated by these subtractions are discussed in section 7 of this chapter. The spectra with the second lowest threshold (18.7x the ^{228}Th Compton edge) were found to be the best compromise between poor statistics and minimum foldover neutron background and were chosen for final analysis.

3. Deadtime Correction

The ADC is dead to incoming signals while it is processing a previous event. This effect is significant at high count rates and has to be taken into account when we calculate the differential cross sections. In order to determine the ADC dead time, signals from the proton monitor and the four detectors in the 0^{o} hut were sent into a scaler and also to the ADC. The ratio of the counts registered by the ADC to the counts registered by the scaler is a measure of the live time and is typically of the order of 80%. These fractional livetimes are the correction factors to the Faraday cup readings and measure the effective charge incident during the run.

4. Neutron detector efficiency and determination of absolute cross sections.

In order to compute differential cross sections from the TOF measurements, it is necessary to measure, or calculate reliably, the detection efficiency of the neutron counters. The latter approach has

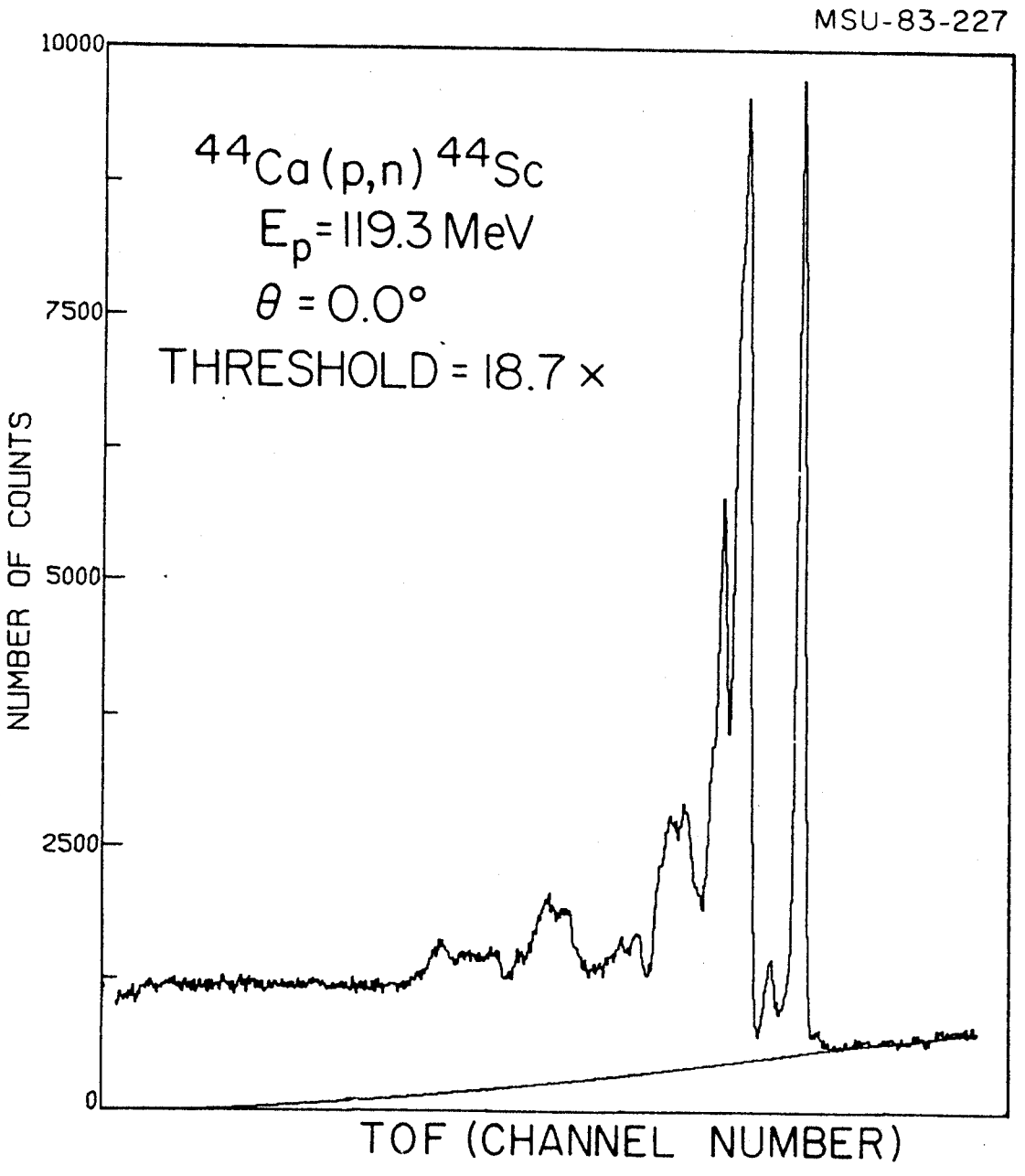

Figure 3.5. Time of flight spectrum for $^{44}Ca(p,n)^{44}Sc$ at 0°, with cosmic ray contribution subtracted. Solid line indicates foldover neutron background.

been used by Rapaport et al., to predict the relative efficiency of the neutron counters for detecting neutrons in the energy range 30 MeV to 200 MeV for different light thresholds (Ta 82). Basically the program computes the probability that an incident neutron of a given energy will induce in the scintillator material, nuclear reactions whose charged products create more than a specified amount of light. Appendix C shows the computed efficiencies for the neutron energy range of interest.

The relative differential cross sections so derived have to be normalized to absolute values. Two calibration runs were made at 0^{o} with targets of ^{7}Li and ^{12}C and are shown in Figures 3.6a and 3.6b. The absolute cross sections are known in the two cases by independent means--from angular distributions normalized to activation analysis cross sections for $^{7}Li(p,n)^{7}Be(0.0 + 0.429\ MeV)$ and from $^{12}C(p,p')^{12}C(15.1\ MeV)$ and arguments of isospin conservation. These measurements have been made at E_{p}=120 MeV and reported elsewhere (Ta 82, Ra 81, Gl 79). Comparison of these relative and absolute cross sections at 0^{o} yields the cross section normalization constant; the relevant numbers are listed in Table 3.3. Note that the absolute cross section for the $^{12}C(p,n)^{12}N(g.s.)$ reaction is only known to within 16% and the $^{7}Li(p,n)^{7}Be(g.s. + 0.429\ MeV)$ cross section is known to within about 3%; but the normalization constants derived from the two cases agreed to within 6%. We took an arithmetic average of the two constants, without weighting them by their errors.

The $^{7}Li(p,n)$ and $^{12}C(p,n)$ data can also be used to check the relative efficiencies used in the analysis. Define

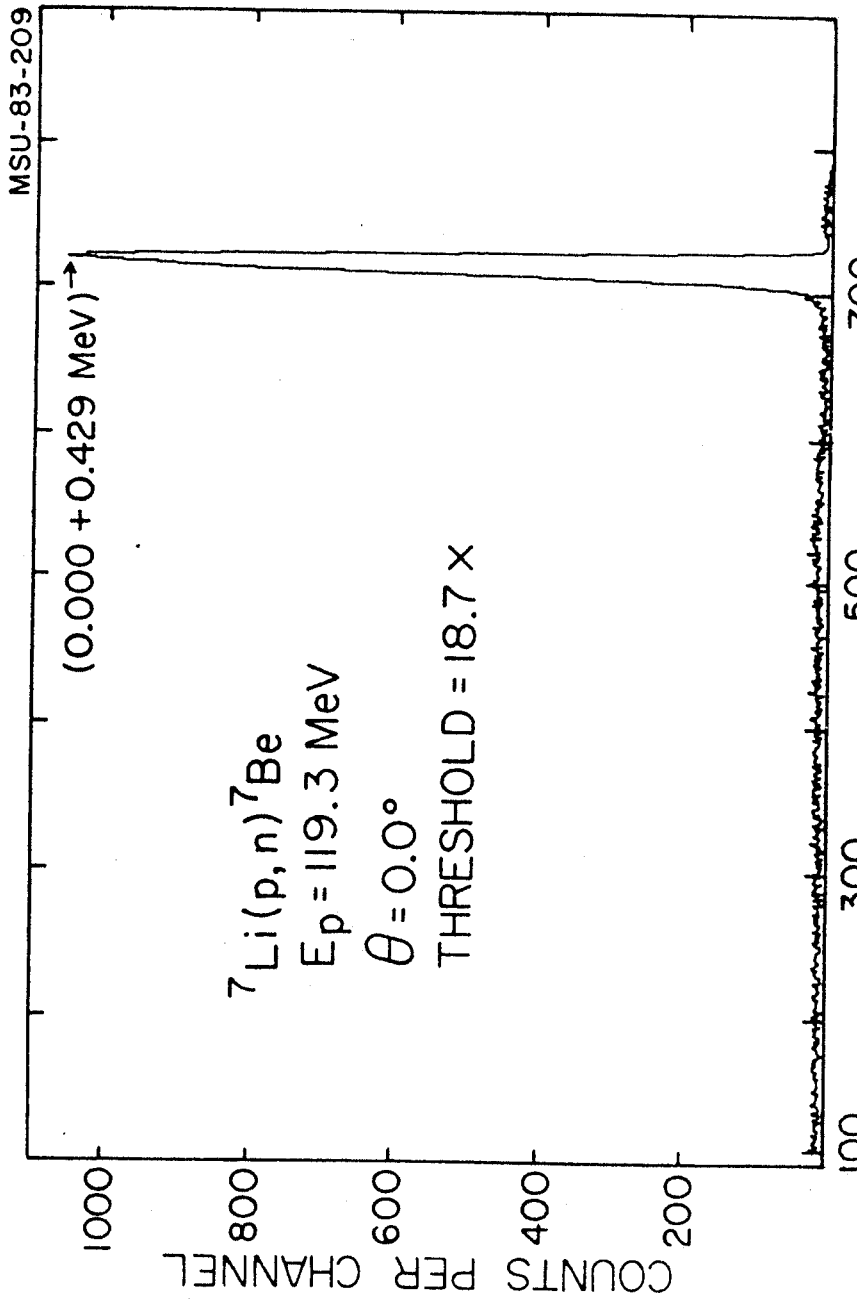

Figure 3.6(a). Time of flight spectrum for ^{7}Li(p,n)^{7}Be.

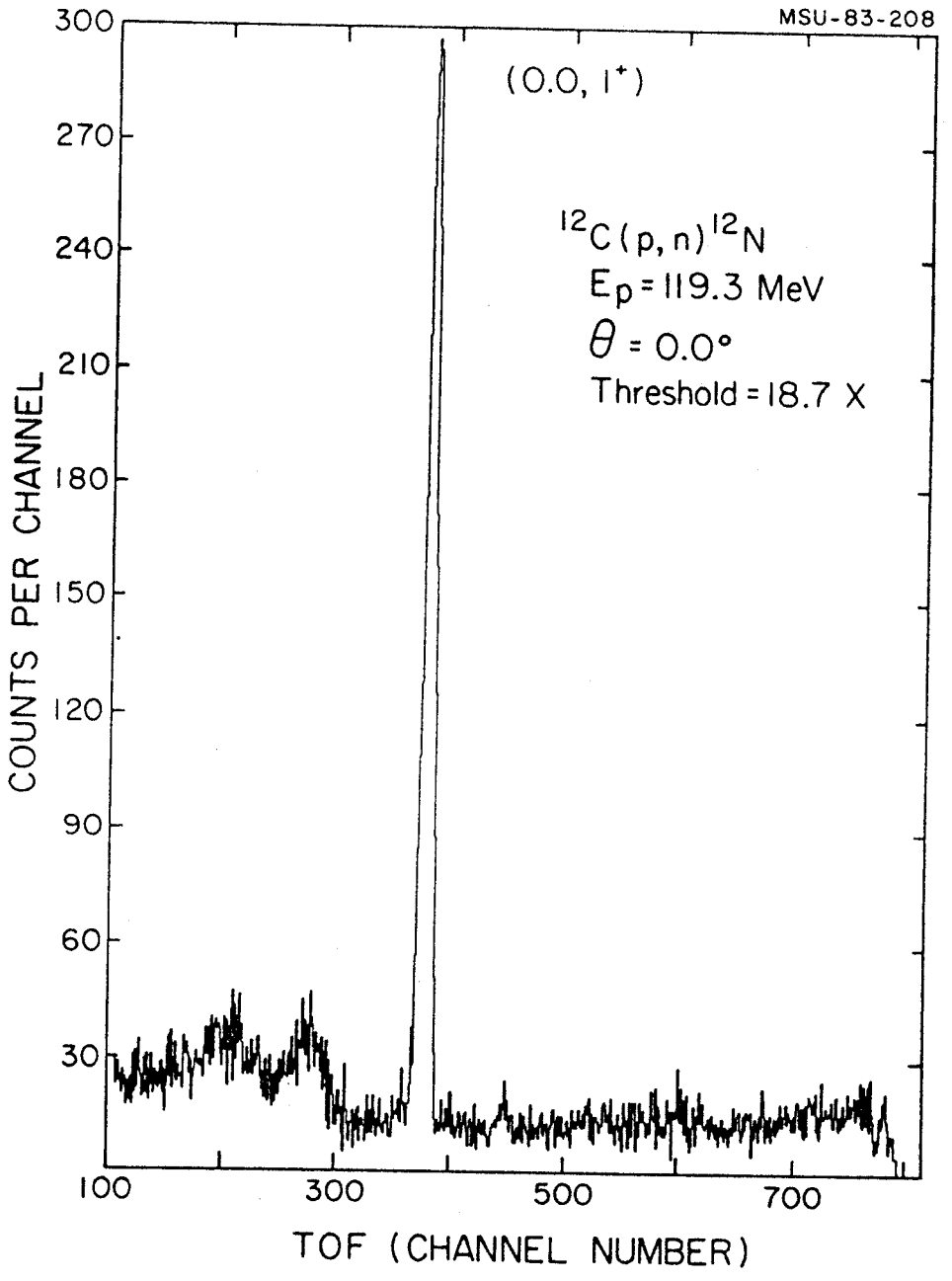

Figure 3.6b. Time of flight spectrum for $^{12}C(p,n)^{12}N$.

Table 3.3. Normalization of Relative to Absolute Differential Cross Sections (at 0^{o}).

Reaction	$E_{neutron}$ (MeV)	Efficiency* (relative)	$d\sigma/d\Omega$(rel.)	$d\sigma/d\Omega$(abs.) (mb/sr)	C ($\frac{d\sigma}{d\Omega}$(rel)/$\frac{d\sigma}{d\Omega}$(abs))
$^{7}Li(p,n)^{7}Be$ (g.s.,0.429 MeV)	117.3	0.1246	1.2126×10^{6}	31.0 ± 1.0 [a]	3.9115×10^{4}
$^{12}C(p,n)^{12}N$ (g.s.)	100.5	0.1030	2.2062×10^{5}	6.0 ± 1.0 [b]	3.6769×10^{4}

a) References: Gl 79, Ta 82.

b) Reference: Ta 82.

* Efficiencies read at Threshold = 18.7 x Th.

$$\text{Yield} \equiv \frac{\text{Peak Area (TOF)}}{F_{T,\text{Effective}} \times Ndx}$$

$$F_{T,\text{Effective}} = \text{Faraday cup (total) x live time}$$

$$Ndx \equiv \text{Target thickness in units of number/cm}^2$$

$$Y \equiv \frac{\text{Yield}(^{7}\text{Li(p,n)}^{7}\text{Be(g.s.+0.429 MeV)})}{\text{Yield}(^{12}\text{C(p,n)}^{12}\text{N(g.s.)})}$$

$$\varepsilon(\text{Th.}) \equiv \frac{\text{Efficiency (117 MeV) (Th.)}}{\text{Efficiency (100 MeV) (Th.)}}$$

ε(Th.) $\equiv$ Threshold (in equivalent electron energy)

$$R(\text{Th.}) \equiv \frac{Y(\text{Th.})}{\varepsilon(\text{Th.})}$$

If the calculated efficiency had the correct energy dependence, then,

(a) Plots of log Y vs. E(Th) and log ε(Th) vs. E(Th) should be parallel curves;

(b) Plot of R(E(Th)) vs. E(Th) should be a constant, independent of E(Th). The constant value = the ratio of experimentally determined absolute cross sections, to within experimental uncertainties. As indicated by Table 3.4 and Figures 3.7a and 3.7b, the relative efficiencies do have the correct behavior. Yet another check on the definition of the threshold and the corresponding efficiencies used in the calculations is to look for the constancy of $d\sigma/d\Omega$ with respect to the threshold. For the nominal thresholds, there is a steady decrease of the inferred cross sections for ^{7}Li and ^{12}C, totalling 36%, as one

Table 3.4

Computation of R as a function of assumed threshold energy

Threshold	$^{7}Li(p,n)^{7}Be$: (g.s., 0.429 MeV) Ndx=$3.71 \times 10^{21}/cm^2$ $E_{Neutron}$=117.3 MeV		$^{12}C(p,n)^{12}N$ (g.s.) Ndx=$1.75 \times 10^{21}/cm^2$ $E_{Neutron}$=100.5 MeV		$Y = \frac{Y1}{Y2}$	$\varepsilon = \frac{\varepsilon 1}{\varepsilon 2}$	$R = \frac{Y1/\varepsilon 1}{Y2/\varepsilon 2}$
	Efficiency (ε1) (relative)	Yield (Y1)*	Efficiency(ε2) (relative)	Yield (Y2)			
10 x Th	0.2035	2.6323×10^{-22} 2.4759×10^{-22}	0.1918	4.2401×10^{-23}	6.0237	1.0610	5.6774±0.12
17 x Th	0.1370	1.6085×10^{-22} 1.5109×10^{-22}	0.1185	2.2723×10^{-23}	6.8640	1.1561	5.9372±0.15
23 x Th	0.0930	9.1746×10^{-23} 8.7250×10^{-23}	0.0660	1.0496×10^{-23}	8.5269	1.4091	6.0513±0.19
28 x Th	0.0600	4.8936×10^{-23} 4.6138×10^{-23}	0.0277	3.9368×10^{-24}	12.0749	2.1661	5.5745±0.28

* The two sets of yields for ^{7}Li correspond to the 2 separate runs that were made, before and after the 0^{o} calcium target runs; the average of Y1 was used in deriving Y.

R average = 5.811±0.080
R(from independent measurements) = 5.17±0.88

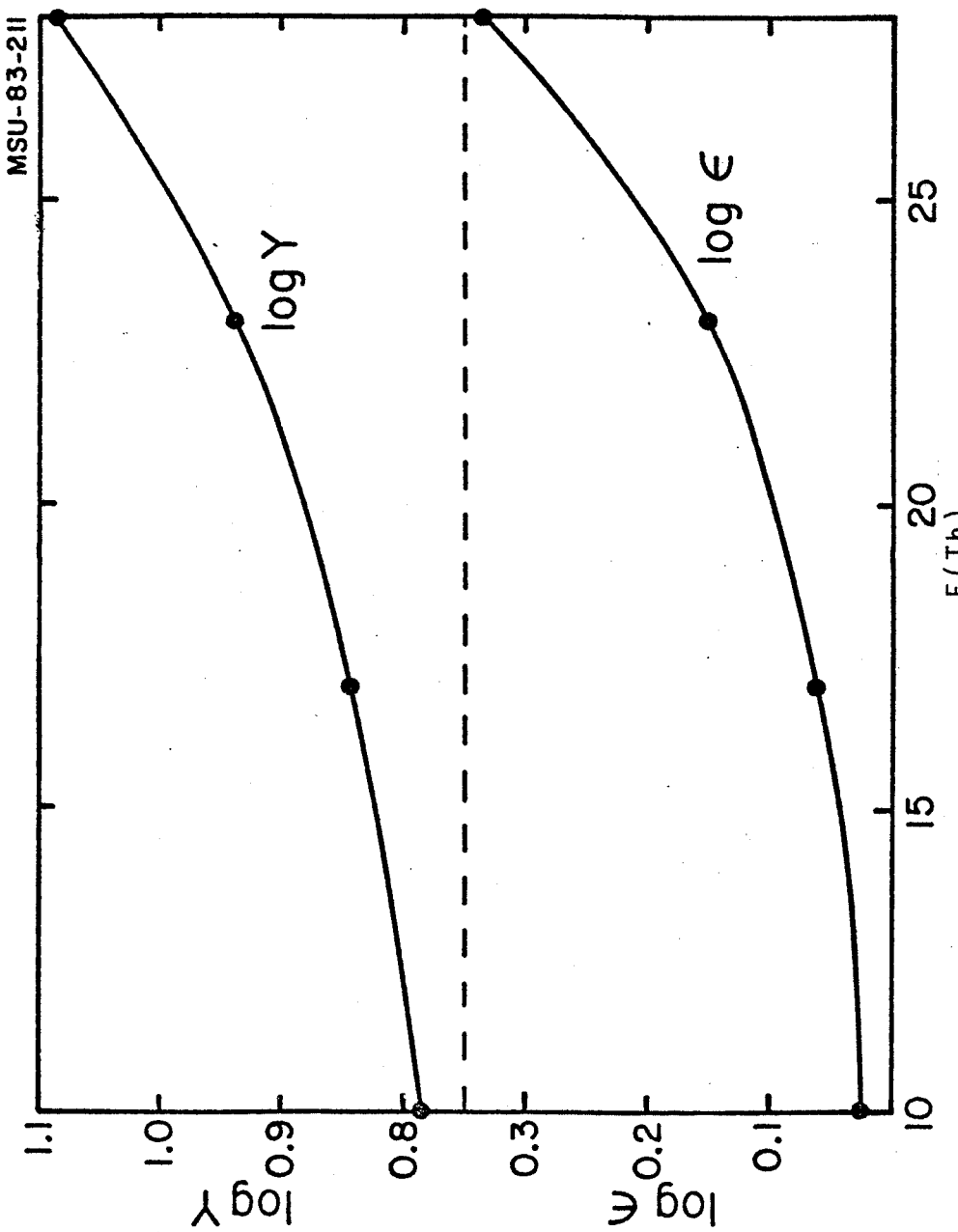

Figure 3.7(a). Plots of log Y and log ε vs. E(Th) in units of Compton Edge. Note that these threshold values are only nominal.

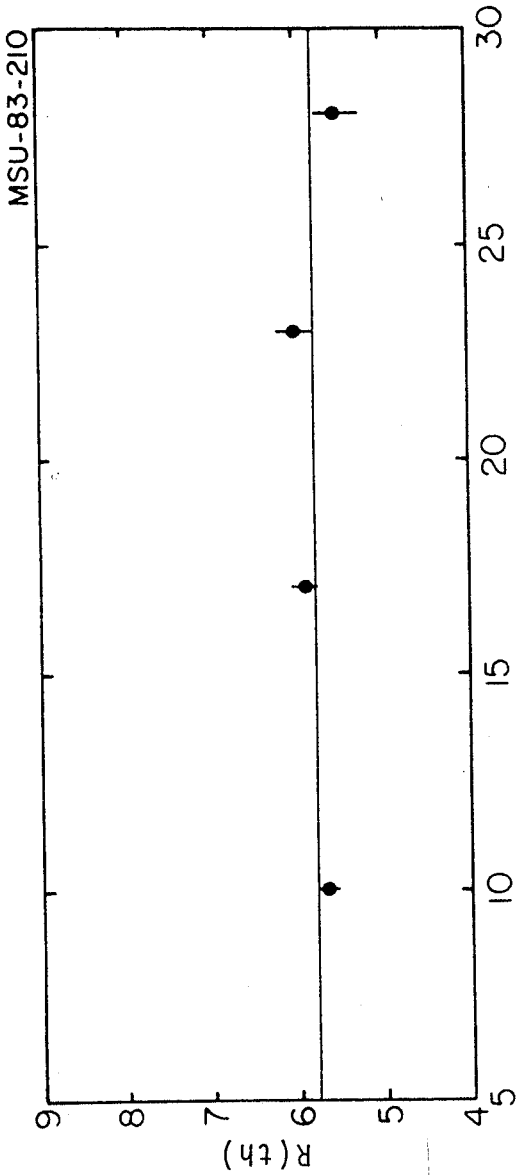

Figure 3.7(b). Plot of R(Th) vs. E(Th) (in units of Compton Edge). Solid line is the weighted average of the four values and agrees with experimentally determined absolute cross section ratios for (p,n) reactions on ^{7}Li and ^{12}C for states shown in Figures 3.6(a) and 3.6(b), to experimental uncertainties. The threshold values shown are only nominal.

Table 3.5a

Dependence of efficiency corrected peak areas on threshold energies

$^{7}Li(p,n)^{7}Be$ (g.s., 0.429 Mev) $E_{Neutron} = 117.0$ MeV

Threshold	Peak Area A	Efficiency ε	A/ε	$\frac{A/\varepsilon}{(A/\varepsilon)_{10xTh}}$
(0.9) 10xTh		0.2150	141884	1.00
(1.0) 10xTh	30505	0.2035	149902	1.00
(1.1) 10xTh		0.1922	158715	1.00
(1.15) 10xTh		0.1866	163478	1.00
(0.9) 17xTh		0.1508	123607	0.87
(1.0) 17xTh	18640	0.1370	136058	0.91
(1.1) 17xTh		0.1246	149599	0.94
(1.15) 17xTh		0.1185	157337	0.96
(0.9) 23xTh		0.1106	96130	0.68
(1.0) 23xTh	10632	0.0930	114323	0.76
(1.1) 23xTh		0.0776	137010	0.86
(1.15) 23xTh		0.0696	152715	0.93
(0.9) 28xTh		0.0866	65485	0.46
(1.0) 28xTh	5671	0.0600	94517	0.63
(1.1) 28xTh		0.0427	132810	0.84
(1.15) 28xTh		0.0347	163618	1.0009

Table 3.5b

Dependence of efficiency corrected peak areas on threshold energies

$^{12}C(p,n)^{12}N$ (g.s.) $E_{Neutron} = 100.0$ MeV

Threshold	Peak Area A	Efficiency ε	A/ε	$\frac{A/\varepsilon}{(A/\varepsilon)_{10xTh}}$
(0.9) 10xTh		0.2055	29188	1.00
(1.0) 10xTh	5999	0.1918	31277	1.00
(1.1) 10xTh		0.1801	33307	1.00
1.15 10Th		0.1734	34595	1.00
(0.9) 17xTh		0.1358	23675	0.81
(1.0) 17xTh	3215	0.1185	27131	0.87
(1.1) 17xTh		0.1030	31229	0.94
1.15 17xTh		0.0945	34021	0.98
(0.9) 23xTh		0.0857	17330	0.73
(1.0) 23xTh	1485	0.0660	22500	0.83
(1.1) 23xTh		0.0463	32080	1.03
(1.15) 23xTh		0.0373	39812	1.15
(0.9) 28xTh		0.0477	11667	0.40
(1.0) 28xTh	557	0.0277	20108	0.64
(1.1) 28xTh		0.0194	28682	0.86
(1.15) 28xTh		0.0148	37635	1.09

moves towards higher thresholds. A detailed analysis of the Compton spectrum from the ^{228}Th source revealed that the thresholds were, in fact set about 10% higher than the nominal 10, 17, 23, and 28 times the Compton edge; therefore, the thresholds were at 26.18, 44.51, 60.21, and 71.97 MeV equivalent electron energy. With this correction, the cross sections do remain a constant to within 15% for all the thresholds. (See Tables 3.5a and 3.5b). This was further verified with the calcium target data. Tests (a) and (b) mentioned above worked as well as they did because ratios were considered in each case; this shows the insensitivity of the derived normalized cross sections to the precise value of the threshold.

5. Neutron Energy Spectra

The TOF spectra (after subtracting the Cosmic ray and the foldover neutron background) have been converted to neutron energy spectra with the relative detector efficiency folded in, using the M.S.U program TOFTOEN. The input data required are distance from target to detector, detector efficiency as a function of neutron energy, proton beam repetition period, TAC calibration in terms of nsec/channel, and the centroid of one peak with known neutron energy. The neutron energy calibration for the spectra shown in Figure 3.8 is

$$E_{Neutron}(MeV) = (\text{channel number} + 2125)/25$$

Appendix C shows energy spectra for all calcium targets at the 3 angles 0.0^{o}, 6.3^{o} and 11.1^{o}. These spectra have been analyzed with the peak fitting program SCOPEFIT, defining backgrounds as shown in Figure 3.8. A reference peak was defined in each case based on a sharp peak in the

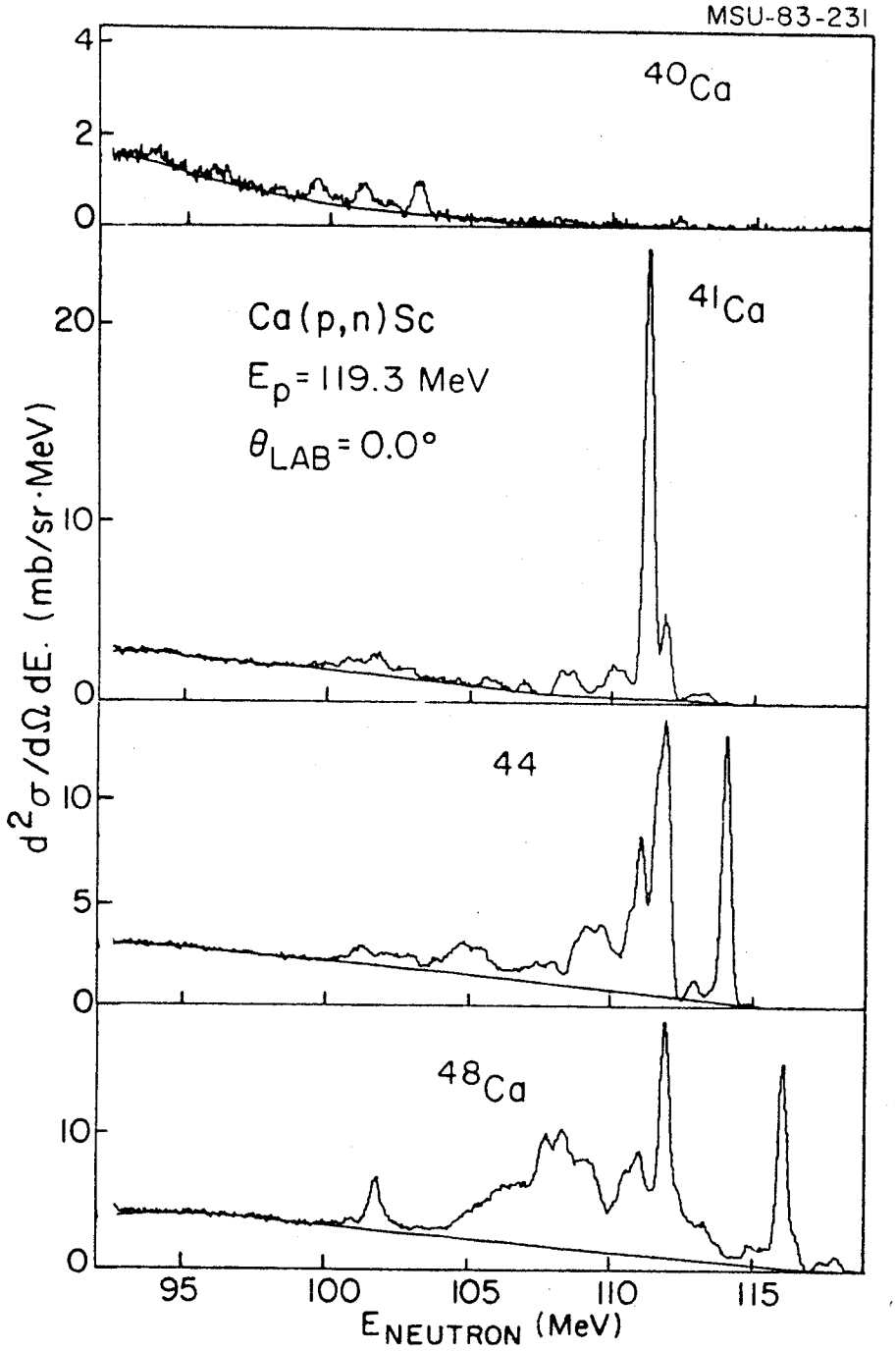

Figure 3.8. Energy spectra for ^{40,42,44} and ^{48}Ca(p,n)^{40,42,44} and ^{48}Sc. Experimenter's backgrounds defined to fit peaks are indicated by solid lines.

high neutron energy end of the spectrum, peaks fitted and areas and centroids obtained. See Tables 3.6, 3,7, 3.8 and 3.9. It should be noted that a constant time resolution does not yield a constant energy resolution; but the neutron energy range in the parts of the spectra that were fitted with a given reference peak shape was small enough that that peak width did not change by more than 9%. This has a negligible effect on the derived centroid for the strong peaks which is known to + 40 KeV (± 1 channel). Relative differential cross sections were converted to absolute values using the normalization constant derived by the method outlined in Section 4 and are listed in Tables 3.6, 3.7, 3.8, and 3.9. Angular distributions are plotted in Figures 3.9, 3.10a, 3.10b, 3.11a, 3.11b and 3.12a, 3.12b for ^{40,42,44} and ^{48}Ca respectively. The TAC nonlinearity mentioned earlier is reflected in the energy spectra. Table 3.10 shows the neutron energies at which this effect is starting to influence the energy spectra

6. Calculation of the GT strength

The angular distributions were used to pick out L=0 transitions; following an empirical method developed by Taddeucci et al., and described in Chapter I, the 0^{o} differential cross sections were used in calculating the total GT strength in ^{42,44} and ^{48}Ca and are compared to the sum rule prediction of B (GT) > 3 (N-Z) (Ta 81). (See Appendix D). It should be noted that the experimentally extracted strengths are independent of the absolute cross section normalization.

The case of ^{42}Ca is an anomaly within our measurements. This has been brought about by the fact that the target was contaminated with oxygen and that the beam was apparently hitting the aluminum target frame during at least part of the 0^{o} run. The bump in the ^{42}Ca(p,n)

Table 3.6. Angular distributions for $^{40}Ca(p,n)^{40}Sc$

E_x(MeV)	Limits E_x(MeV)	dσ/dΩ (mb/sr)		
		0.0°	6.3°	11.1°
0.96	0.37 to 1.33	0.372±0.036	0.224±0.115	1.281±0.116
1.81	1.41 to 2.33	0.109±0.012	0.284±0.026	0.417±0.040
2.73	1.85 to 3.29	0.384±0.036	0.269±0.033	0.140±0.020
4.22	3.29 to 4.89	0.394±0.041	0.534±0.052	0.569±0.075
5.75	5.17 to 6.25	0.106±0.011	0.148±0.015	0.261±0.028

Table 3.7. Angular distributions for $^{42}Ca(p,n)^{42}Sc$

E_x(MeV)	Limits E_x(MeV)	dσ/dΩ(mb/sr)		
		0.0°	6.3°	11.1°
0.00	-0.49 to 0.63	1.843±0.171	0.829±0.095	0.304±0.048
0.61	0.11 to 1.23	10.342±0.915	4.593±0.411	1.361±0.126
1.80	0.95 to 2.99	1.782±0.169	0.840±0.086	0.675±0.074
3.43	2.71 to 4.27	1.239±0.118	0.681±0.070	0.310±0.038
4.93	4.39 to 5.39	0.256±0.023	0.191±0.018	0.210±0.020
6.12	5.39 to 6.83	0.423±0.038	0.287±0.027	0.146±0.016
10.28	6.87 to 13.99	3.047±0.271	1.609±0.146	1.350±0.124

Table 3.8

Angular distributions for $^{44}Ca(p,n)^{44}Sc$

E_x(MeV)	Limits E_x(MeV)	$d\sigma/d\Omega$(mb/sr)		
		0.0^o	6.3^o	11.1^o
0.67	0.14 to 1.78	5.225±0.464	2.313±0.207	1.003±0.096
1.78	1.26 to 2.22	0.432±0.042	0.155±0.029	0.207±0.020
2.79	2.26 to 3.26	4.973±0.444	3.317±0.304	0.767±0.076
3.12	2.62 to 3.62	3.561±0.322	1.581±0.153	0.646±0.009
3.80	3.06 to 4.38	4.765±0.437	1.119±0.111	1.379±0.095
5.27	4.30 to 6.38	4.898±0.434	1.876±0.173	0.834±0.087
7.31	6.38 to 8.46	1.672±0.148	0.374±0.043	0.079±0.012
9.77	8.46 to 11.30	2.765±0.246	0.481±0.045	
12.82	11.30 to 14.78	0.784±0.159	0.182±0.028	0.332±0.040

Table 3.9

Angular distributions for $^{48}Ca(p,n)^{48}Sc$

E_x(MeV)	Limits E_x(MeV)	$d\sigma/d\Omega$(mb/sr)		
		0.0^o	6.3^o	11.1^o
0.67	0.13 to 1.67	0.512±0.053	0.162±0.017	0.464±0.043
1.08	1.27 to 1.95	0.288±0.030	0.394±0.041	0.482±0.049
2.52	1.63 to 3.31	7.176±0.638	3.615±0.327	1.152±0.109
3.34	2.47 to 4.15	0.465±0.058	0.641±0.063	3.452±0.057
3.86	2.83 to 4.43	0.989±0.095	0.898±0.088	1.317±0.126
5.13	4.47 to 6.07	1.824±0.178	1.049±0.103	0.636±0.072
5.96	4.83 to 6.91	2.425±0.239	0.735±0.081	0.677±0.083
6.67	5.75 to 7.63	9.322±0.680	4.086±0.372	1.902±0.129
7.86	6.43 to 8.63	9.290±0.839	6.191±0.381	1.767±0.171
11.02	8.63 to 15.59	28.937±2.566	10.214±0.913	4.011±0.358
16.8	15.59 to 19.07	3.344±0.297	2.007±0.185	11.462±0.140

Table 3.10. Neutron Energies (in MeV) below which TAC nonlinearity is present in the energy spectra

Target \ θ	0.0°	6.3°	11.1°
^{40}Ca	97.40	97.16	97.20
^{42}Ca	98.04	97.12	97.20
^{44}Ca	98.12	97.20	97.20
^{48}Ca	98.36	97.12	97.24

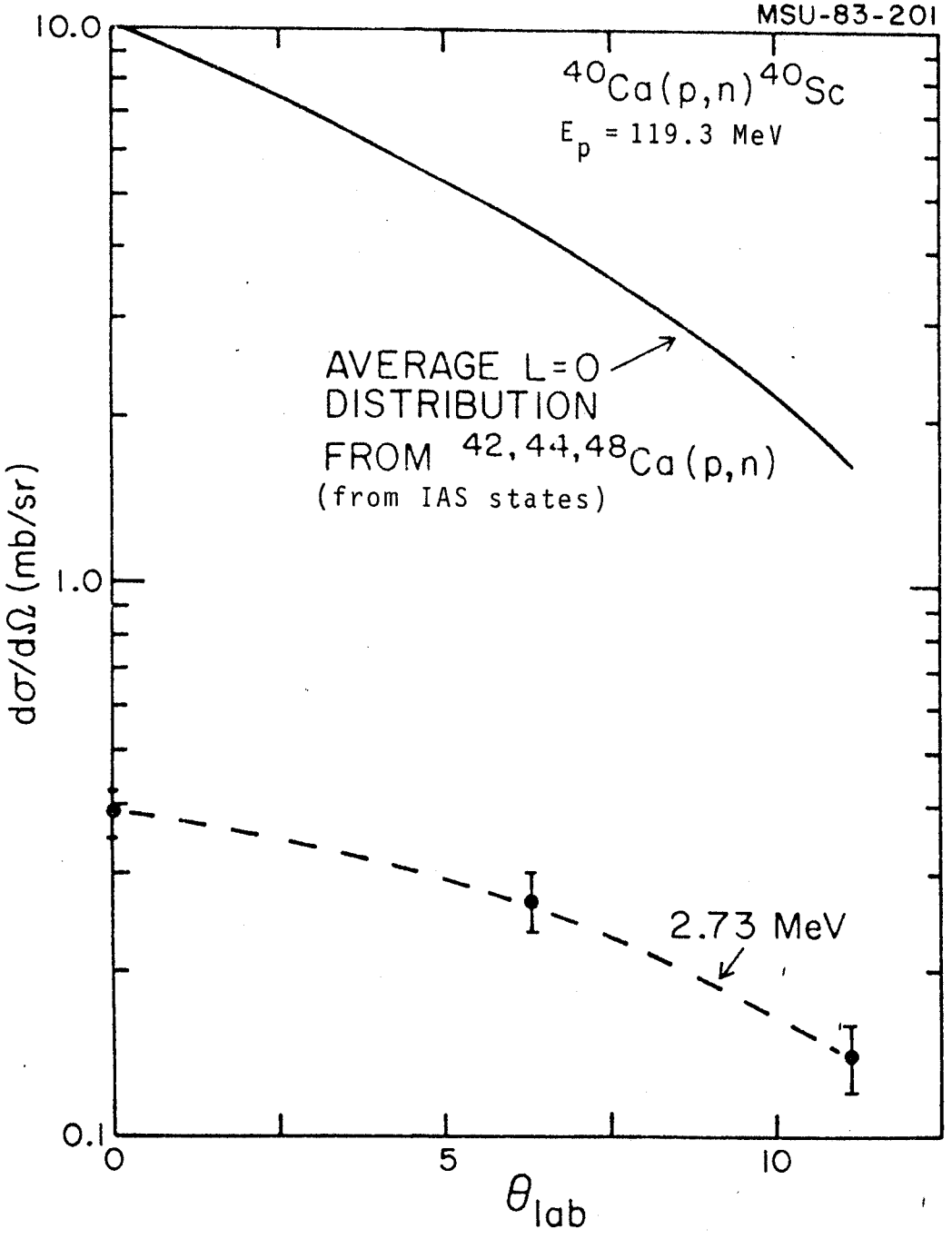

Figure 3.9. Angular distribution of 1^+ state in ^{40}Sc (dotted line). Solid line shows an average of the 1^+ angular distributions derived from ^{42,44} and ^{48}Sc.

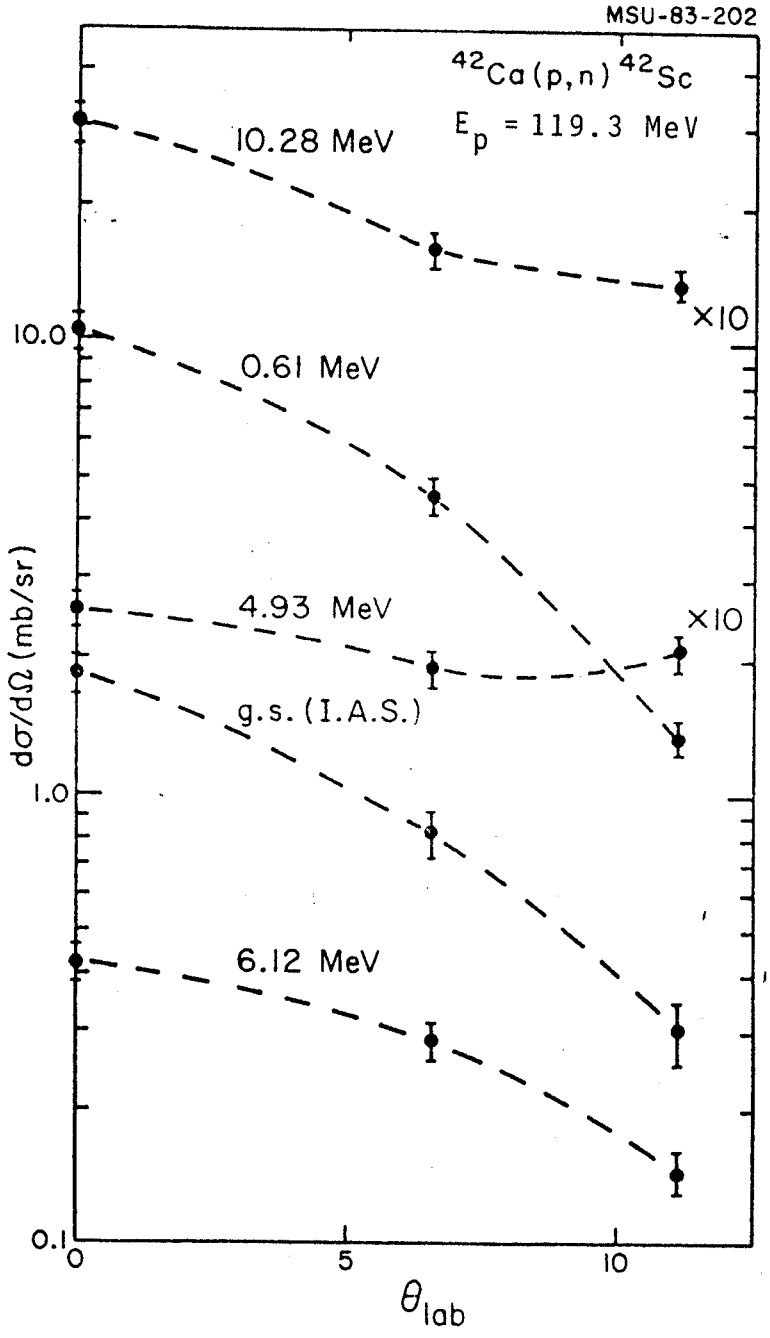

Figure 3.10(a). Angular distributions of observed states in ^{42}Sc.

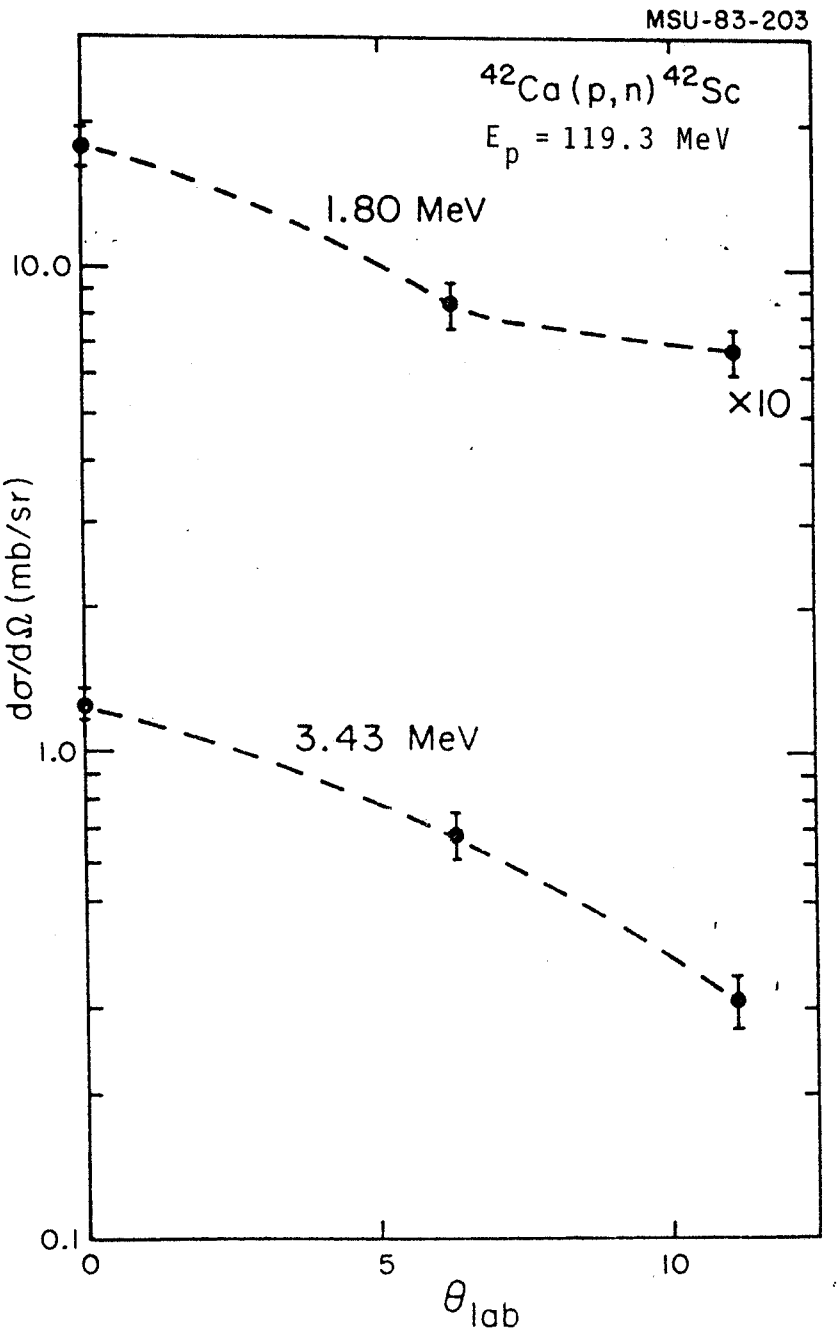

Figure 3.10(b). Same as Figure 3.10(a).

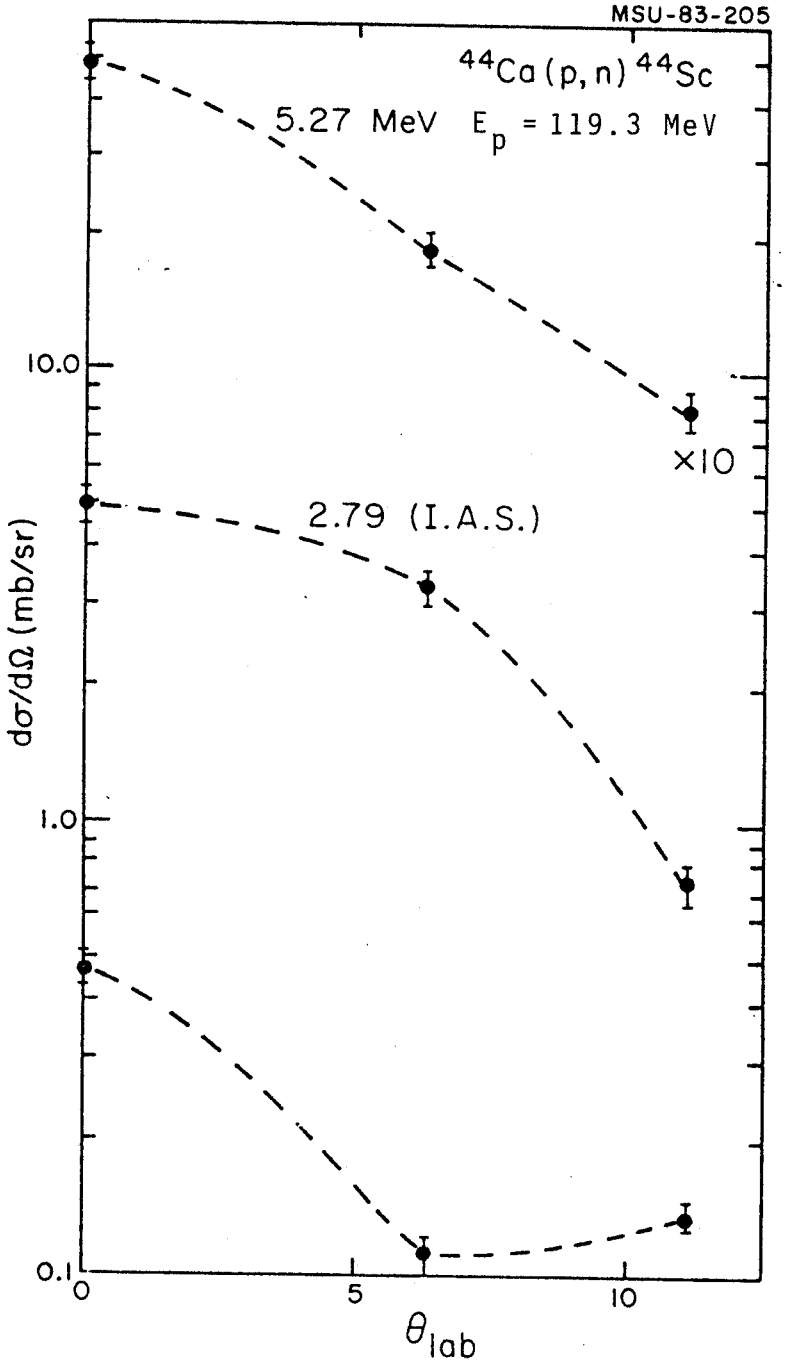

Figure 3.11(a). Angular distributions of observed states in ^{44}Sc.

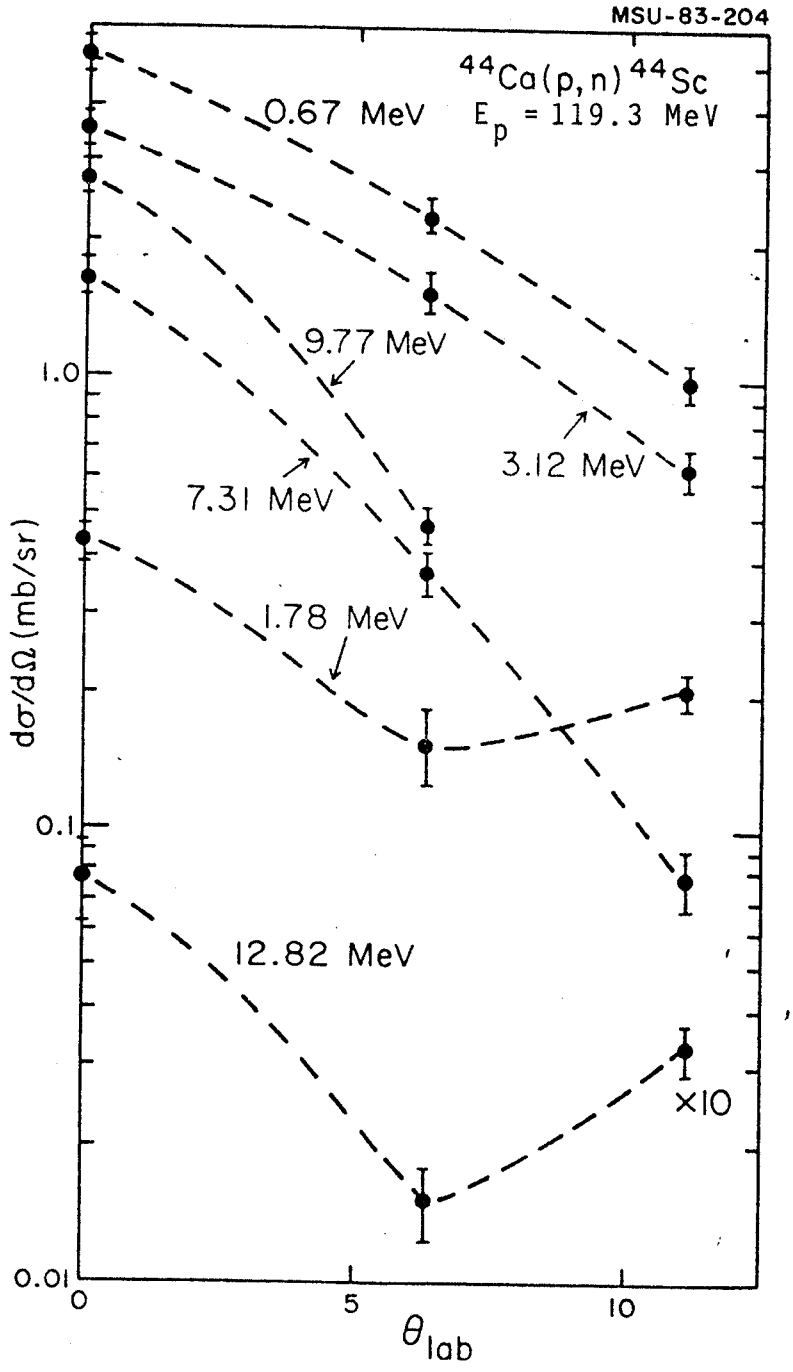

Figure 3.11(b). Same Figure 3.11(a).

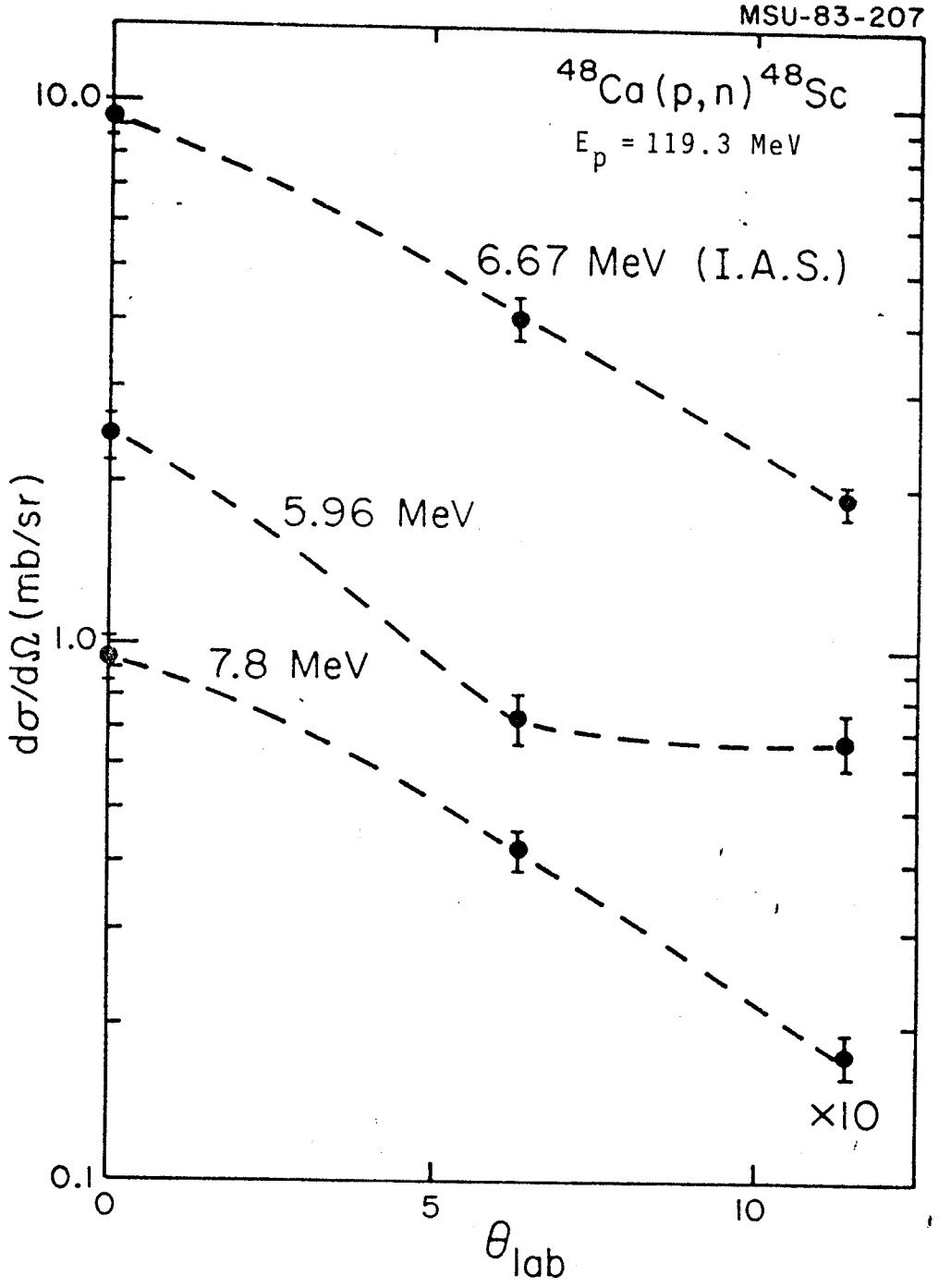

Figure 3.12(a). Angular distributions of observed states in ^{48}Sc.

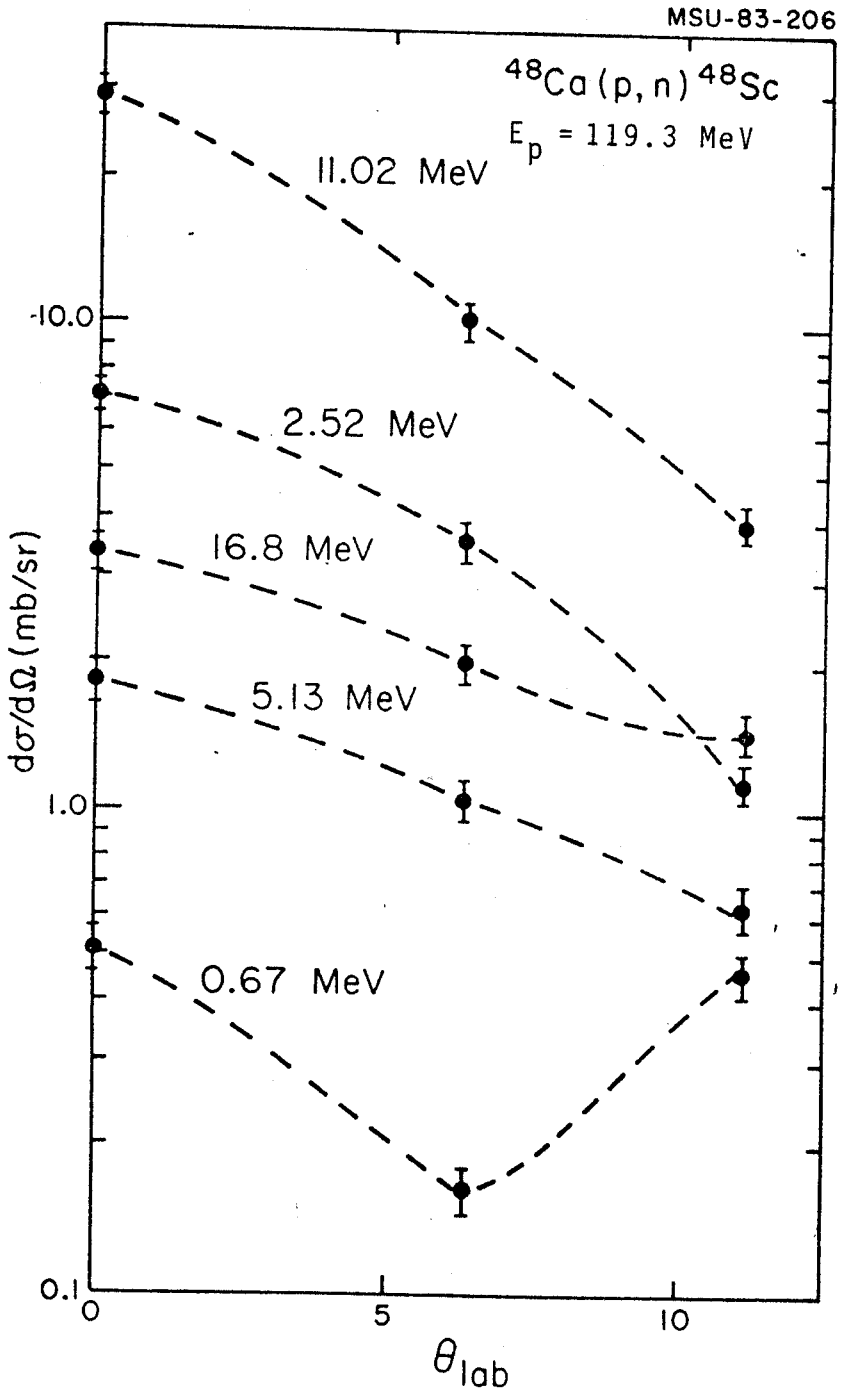

Figure 3.12(b). Same as Figure 3.12(a).

spectrum just below the ground state in ^{42}Sc is at the correct energy for the ^{27}Al(p,n) reaction. Therefore, the apparent measured GT strength of roughly 82% of the sum rule prediction does not have much reliability. The following reasoning might give a rough estimate of what was actually seen from our run, excluding possible contributions from oxygen and aluminum. Consider the high excitation regions of the ^{42,44} and ^{48}Sc spectra with no sharp resonances. The cross sections to this part of the spectra can come from (a) valence neutrons, and therefore, should scale roughly as the neutron excess in the target and should be compared at the same excitation energy in the residual nuclei and (b) valence neutrons from the ^{40}Ca core, and therefore, should be the same for all Ca isotopes, and should be compared at the same Q value (same neutron energy). For the sake of simplicity, let us assume that the knockout neutron background is independent of excitation energy in the residual nucleus within the region of interest. Then we can write,

$$\text{Height(Bkg)} = C_0 + (N-Z) \times C_1$$

where C_0 and C_1 are constants to be determined. From the ^{44} and ^{48}Sc cases, we can solve uniquely for C_0 and C_1. Comparing the measured background height to that predicted by the constants C_0 and C_1 for ^{42}Sc would then provide us with a scale factor with which to reduce the measured strength in ^{42}Ca. For example, choose a neutron energy of 100.0 MeV; the measured heights of the backgrounds for the three cases ^{42,44} and ^{48}Sc, are 1.83, 2.16, and 3.41 mb/sr, MeV respectively. Solving for C_0 and C_1 from the ^{44,48}Ca data one gets

C_0 = 0.91 mb/sr, MeV, and C_1 = 0.31 mb/sr, MeV;

Then the predicted height for ^{42}Ca is 1.53; comparing this to the measured value of 1.83 mb/sr MeV one gets the correction factor to be 0.83 in the knockout region. The measured GT strength of 82% should be scaled by this factor to give a corrected strength of 68%.

One sees in the results for ^{44} and ^{48}Ca the so called quenching of the GT strength (40.5% and 51.8% respectively of the sum rule prediction) that has been seen in recent (p,n) reaction studies at intermediate energies. Suggestions by Osterfeld that substantial 1^+ strength may be hidden in the experimenter's background drawn to extract the above cross sections was investigated in detail, and is discussed in Chapter IV.

7. Error Analysis

There are two types of errors affecting our measurements--systematic and statistical. Sources of systematic error include target thickness uncertainty (1 to 2%), current integrator error (2%), and error in the normalization constant to convert relative differential cross sections to absolute values (8.5%). Sources of statistical errors are the uncertainties in the Monte Carlo calculations of the relative efficiencies (1 to 3%), Cosmic ray and foldover neutron background subtraction (0.1 to 3%), and background definition and peak fitting (0.5 to 5%). By the nature of the method used to compute total GT strength i.e., as a ratio to the IAS peak, the systematic errors do not contribute, only the statistical errors are relevant. But the absolute differential cross sections quoted here carry both the statistical and the systematic errors, which were added in quadrature. These were in the range of 8 to 19%, typically 10%.

IV. Data Analysis

In this chapter, some of the methods used to determine if there really is a quenching of the GT strength in calcium isotopes are discussed. It is appropriate to start with the question of whether the experimenter's background contains substantial 1+ strength and the basis for such a claim. Recently, Osterfeld performed microscopic background calculations for (p,n) reactions on ^{40,48}Ca at 160 MeV (Of 82). His model assumptions were: (i) For (p,n) reactions at incident energies >100 MeV, the reaction mechanism is direct, i.e., one step processes dominate; (ii) The effective projectile-target nucleon interaction can be represented by the free nucleon-nucleon t matrix, i.e., by the G3Y interaction of Love and Franey (impulse approximation); (iii) The (p,n) background is dominated by spin-flip transitions, i.e., S=1, T=1; The final nuclear states are assumed to be simple proton particle-neutron hole states, including bound, quasi bound, and continuum states. The cross sections were calculated with a DWBA code. This code includes knockout exchange amplitudes exactly.

Figure 4.1 shows a schematic representation of the model. This model reproduces 0^{o} data for ^{48}Ca (p,n)^{48}Sc in the continuum to within a factor of 1.3. A striking prediction of these calculations is that the continuum background drops to zero rather sharply at Q = -20 MeV, for ^{48}Ca; a similar behavior is predicted for ^{40}Ca (p,n) at Q = -25 MeV. Figure 4.2 illustrates this. This falling off can be explained qualitatively as follows: The incoming proton knocks out a neutron which carries a major part of the energy leaving the proton with a small amount of kinetic energy ($\leq$10 MeV). The combined effect of the Coulomb and centrifugal barriers keeps the low energy proton away from the

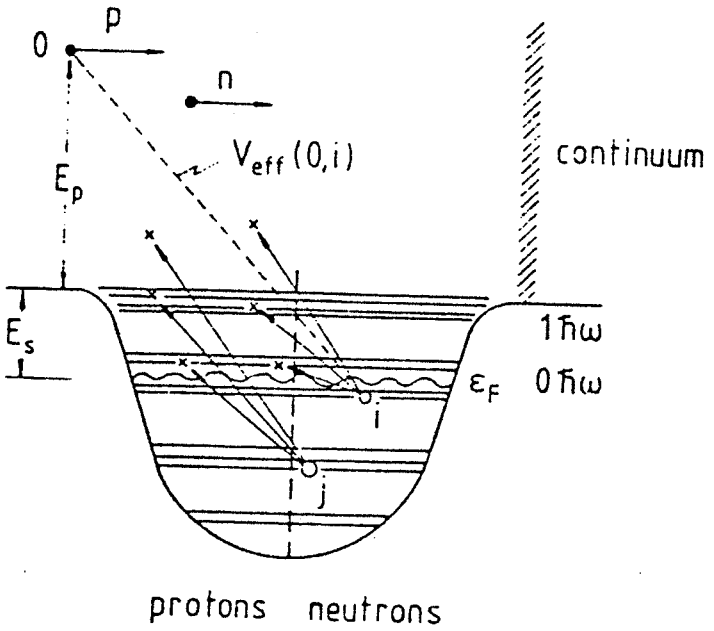

FIG.4.1Schematic representation of the microscopic model used for the background calculations. In the figure ϵ_F denotes the Fermi energy, E_S the nucleon separation energy, and E_p the incident projectile energy. For the effective projectile target nucleon interaction V_{eff} the G3Y interaction of Love and Franey (Ref. 8) is used.

(Figure and caption from Osterfeld's work (Of 82).)

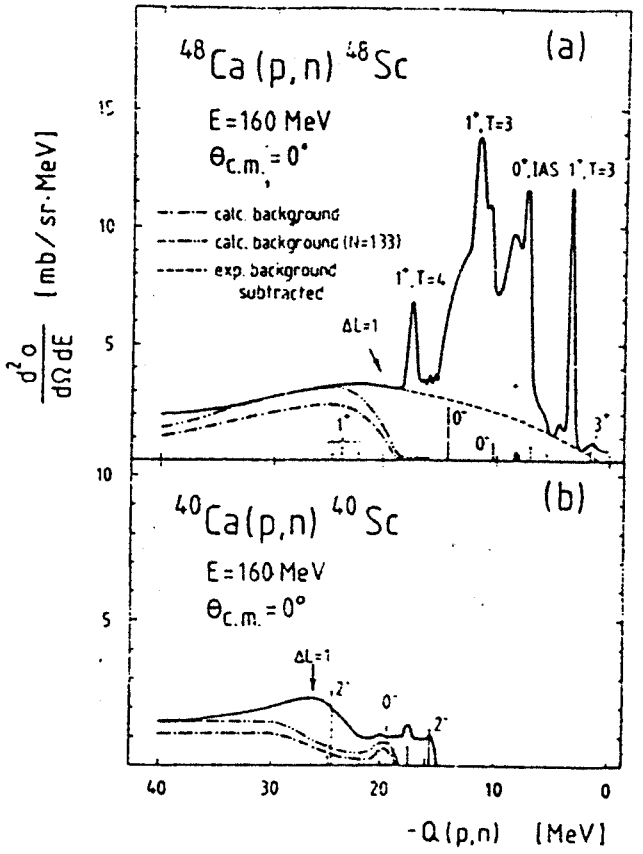

FIG.4.2 Zero degree spectra for the reactions $^{48}Ca(p,n)$ (a) and $^{40}Ca(p,n)$ (b). The data (thick full line) are taken from Refs. 13 and 14 (see text). The discrete lines are calculated cross sections due to bound and quasibound states. The arrow labeled with $\Delta L = 1$ indicates the location where the $\Delta L = 1$ resonance $(0^-, 1^-, 2^-)$ would occur if nuclear collectivity were included for these states. The theoretical cross sections due to the GTR and IAS are *not* plotted. The optical parameters for the cross section calculations have been taken from Ref. 20.

(Figure and caption from Osterfeld's work (Of 82).)

nuclear surface; this means that the proton wavefunction is small near the nuclear surface and so are the transition rates to these states, particularly when L = 0. The implication, then, is that most of the background subtracted in the analysis of ^{48}Ca(p,n) is in fact, GT strength. Osterfeld finds that including this background raises the fraction of the sum rule strength observed in this case from 43% to 51%.

Inspired by the above work, we have analyzed our data following a method suggested by Rapaport (Ra 82). The energy spectra were used to compute cross sections in 2 MeV bins from the ground state upwards, peaks and background included. The angular distributions so derived, were fitted with linear combinatins of DWBA cross sections to final states 1^+, 1^-, and 3^+. A least squares fitting routine was used to minimize χ^2 for combinations of these final states, taken two at a time and that pair which gave the least χ^2 was chosen to obtain the corresponding spectroscopic strengths. The code used was DWBA 79, with the free nucleon-nucleon matrix of Love and Franey; only $\pi f_{5/2} \nu f_{7/2}^{-1}$ configurations were considered. Including $\pi f_{7/2} \nu f_{7/2}^{-1}$ caused negligible change in the angular distributions. Table 4.1 lists the optical model parameters used in computing the DWBA cross sections; Figure 4.3 shows comparisons of measured and predicted DWBA cross sections for known states in ^{42} and ^{48}Sc. Tables 4.2 and 4.3 list the results of this type of analysis for ^{44,48}Ca. A similar analysis was not carried out for ^{42}Ca because of contamination with oxygen and aluminum. As a rule, we find that for ^{44}Ca and ^{48}Ca a mixture of 1^+ and 3^+ states represents the data at low excitations and a combination of 1^+ and 1^- is required to reproduce our data at higher excitations. It is interesting to note that Osterfeld's prediction is borne out by the behavior of 1^- strength, as

Table 4.1
Optical Model Parameters†

	R_c = 1.25 fm
Vol. Real	V = 9.73 MeV
	r_0 = 1.44 fm
	a_0 = 0.52 fm
Vol. Imaginary	W = 13.73 MeV
	r_0 = 1.24 fm
	a_0 = 0.57 fm
SO Real	V_{SO} = 3.0 MeV
	r_{SO} = 1.06 fm
	a_{SO} = 0.6 fm
SO Imaginary	W_{SO} = -1.00 MeV
	$r_{W_{SO}}$ = 1.06 fm
	$a_{W_{SO}}$ = 0.6 fm

†Optical Model parameters provided by N. Anantaraman (Ar 83) and derived from p+^{58}Ni data at 157 MeV. See also Comparat et al. (Co 74).

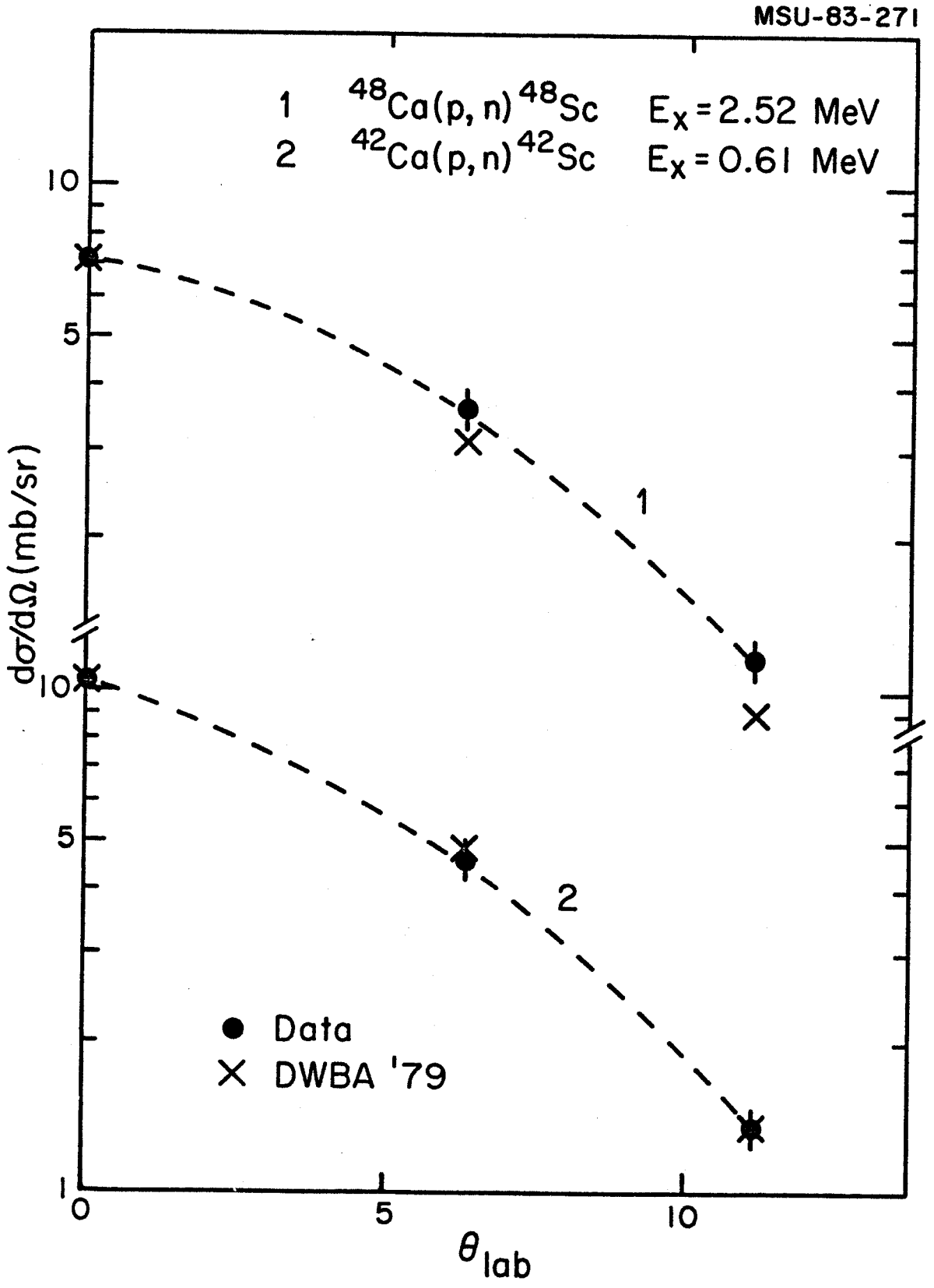

Figure 4.3. Comparison of measured and DWBA 79 predicted differential cross sections for 1^+ states in $^{42}Ca(p,n)^{42}Sc$ and $^{48}Ca(p,n)^{48}Sc$.

Table 4.2

$^{44}Ca(p,n)^{44}Sc$
Contributions to 0° cross sections from 1^+, 1^- and 3^+ states.

E_x(MeV)	$d\sigma/d\Omega$ (mb/sr) (0°)		
	1^+	1^-	3^+
1.0	6.401	-	0.208
3.0	8.757	-	0.256
5.0	7.298	-	0.377
7.0	4.024	-	0.321
9.0	4.690	-	0.508
11.0	4.632	-	0.774
13.0	5.439	0.155	-
15.0	4.806	0.246	-
17.0	5.104	0.348	-
19.0	6.223	0.234	-
21.0	5.694	0.692	-

Table 4.3

Ca(p,n) Sc

Contributions to 0° cross sections from 1^+, 1^- and 3^+ states.

E_x (MeV)	$d\sigma/d\Omega$ (mb/sr)		
	1^+	1^-	3^+
1.0	0.488	-	0.405
3.0	6.754	0.426	-
5.0	3.181	-	0.689
7.0	5.093	0.283	-
9.0	11.045	0.169	-
11.0	13.799	0.174	-
13.0	8.516	0.165	-
15.0	5.008	0.214	-
17.0	6.814	0.339	-
19.0	5.232	0.488	-
21.0	5.247	0.699	-

extracted from our data. The 1^+, 1^- and 3^+ strengths from the best fits are plotted vs. excitation energy in scandium and displayed in Figures 4.4 and 4.5 for A = 44 and 48. One can also see that 1^+ strength extends to higher excitations than was previously thought.

Another way to extract 1^+ strength from (p,n) spectra was recently suggested by Goodman and applied to the case of ^{42}Ca(p,n) (Go 82). The criterion for GT strength is that the angular distribution be that of L = 0. The object is to subtract L≠0 contributions from the 0° spectrum. This is done by first subtracting the 0° spectrum from the 2.5° spectrum scaled by the angular distribution for the L = 0 part so that the strong GT peak subtracts out. The result is taken to be an approximation of the L≠0 spectral shape as seen at 0°. This is then scaled by the cross section ratio between the 2.5° and 0° spectra in the region of the L=1 resonance and is subtracted from the 0° spectrum to yield the L=0 spectrum at 0°. It is instructive to apply the above method in the idealized case shown in Figure 4.6(a) to see its usefulness and check the validity of the argument.

We see that the method would work well if only one L=0 component, say L=1, is important, and if there were no L=0 (1^+) strength in the region of the 1^- resonance. These are implicit assumptions in Goodman's method. If one used the ratio of cross sections in the L=1 region to scale the so called L=0 spectrum, and subtract it from the 0° spectrum to obtain a pure 1^+ spectrum, then at least a part of the 1^+ strength present in that region is subtracted out too. There is no reason for an a priori assumption of no 1^+ strength at high excitations. In fact, our fits to the data (peak + background) through the observed range of excitation indicate just the opposite. Therefore, we believe that

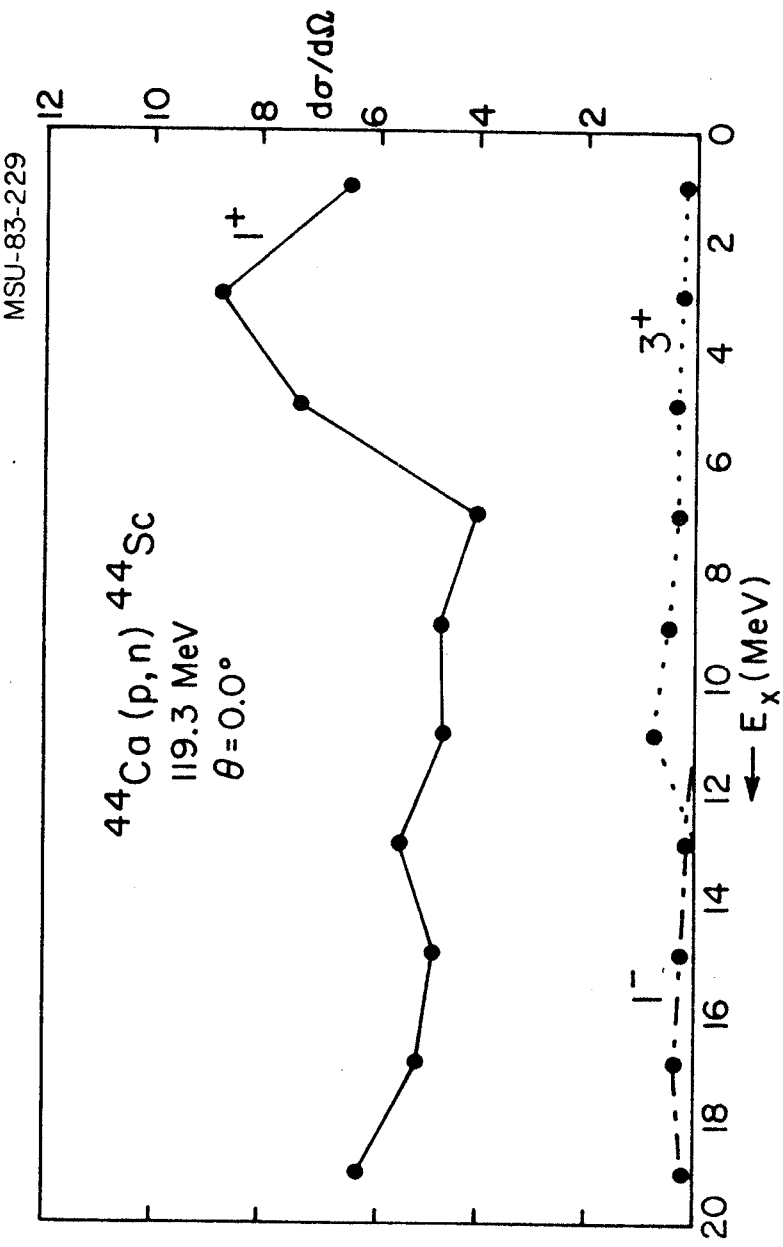

Figure 4.4. Plot of 1^+, 1^- and 3^+ strengths vs. excitation energy in ^{44}Ca(p,n)^{44}Sc at 0°.

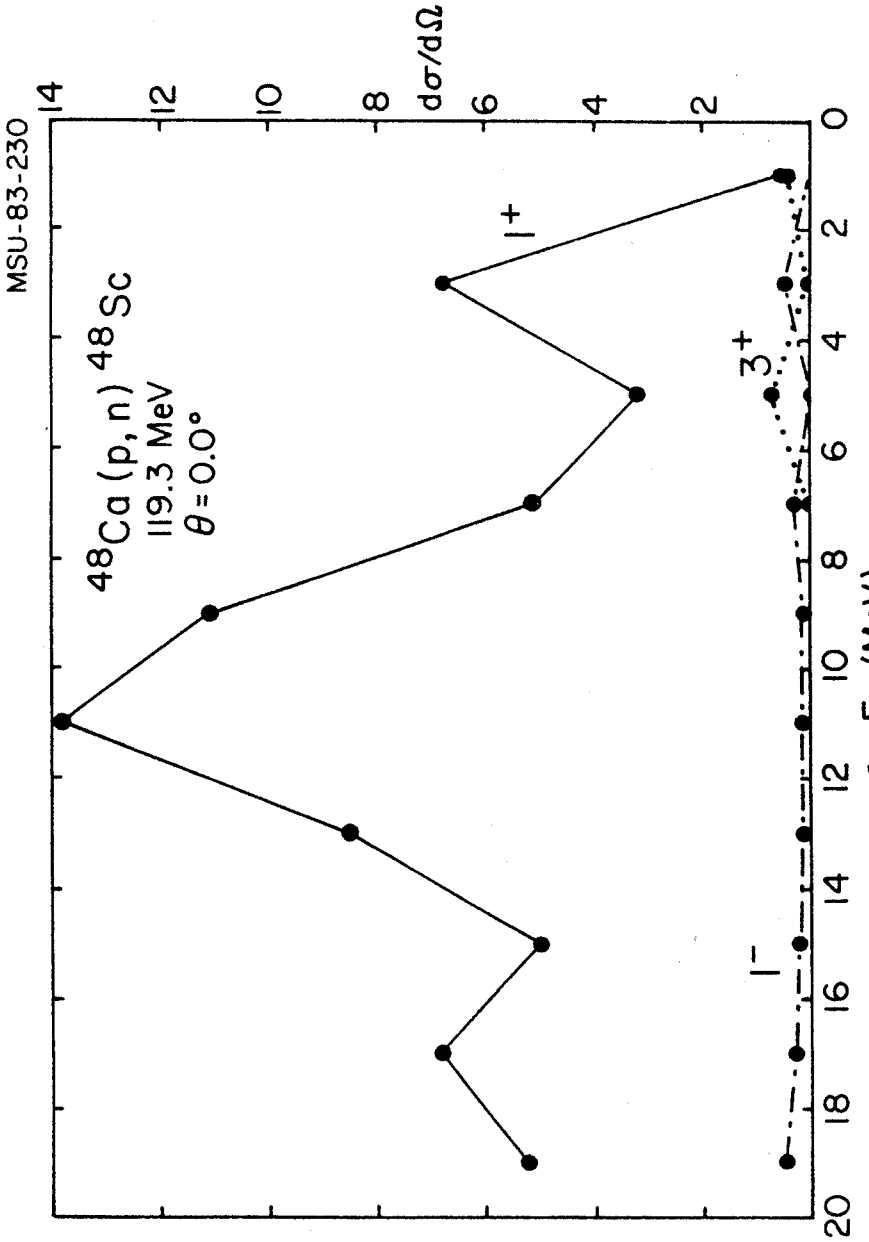

Figure 4.5. Plot of 1^+, 1^- and 3^+ strengths vs. excitation energy in ^{48}Ca(p,n)^{48}Sc at 0°.

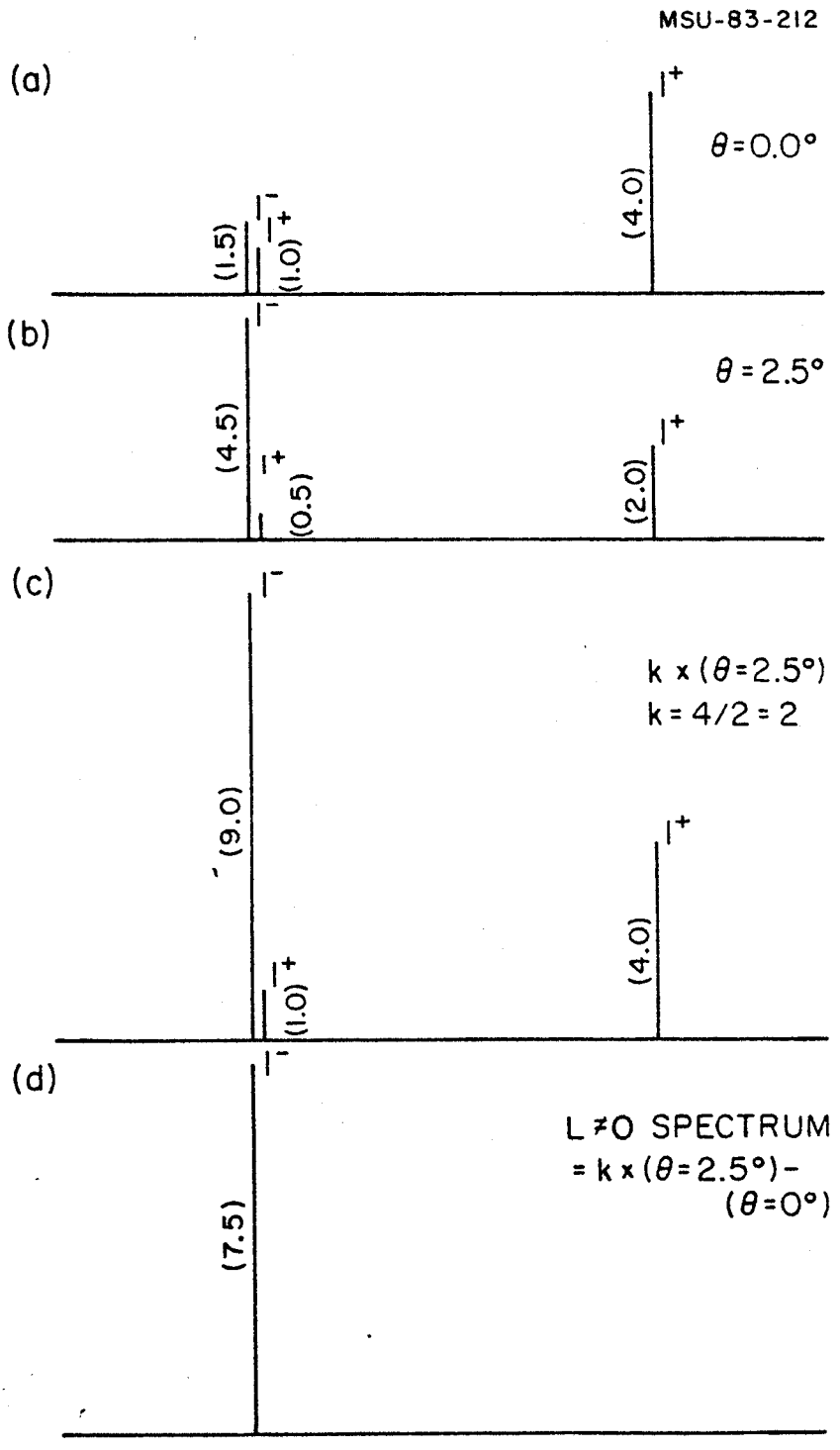

Figure 4.6. Application of Goodman's method in an idealized case.

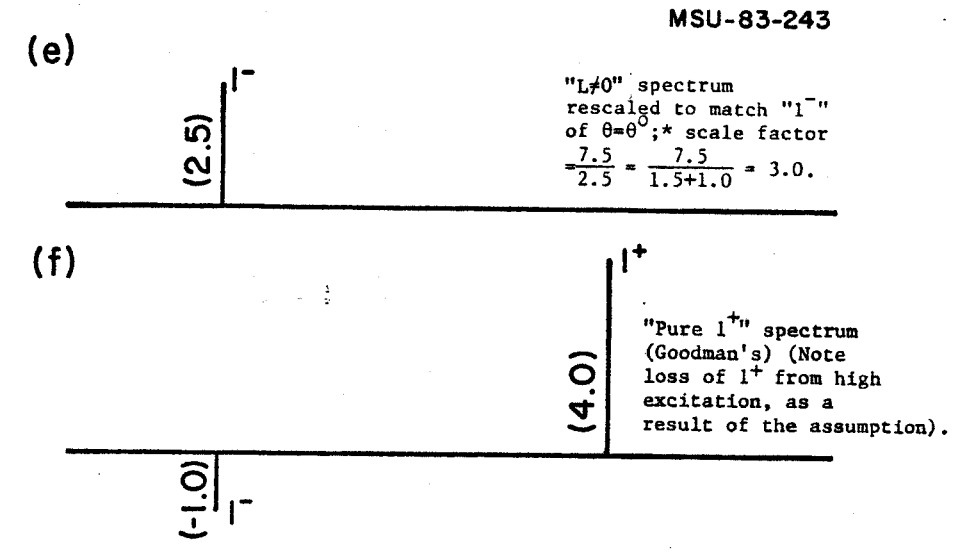

*Including the 1^+ at high excitation as 1^- leads to the wrong scale factor of 3.0; should be 7.5/1.5 = 5.0; making this correction leads to (e') and (f').

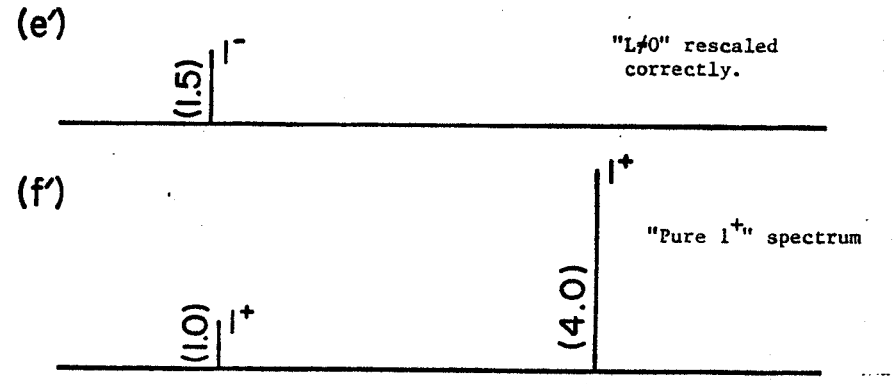

Figure 4.6 continued

Goodman's method is correct only up to the point where he obtains the L≠0 spectrum. Therefore we used it to obtain the L≠0 spectra from the 0^{o} and 6.3^{o} data for ^{42,44} and ^{48}Ca. These are shown in Figure 4.7. The small peaks in the region of the strong GT (1^{+}) at low excitation arise from the fact that we did not apply a correction for kinematic and electronic shifts of the peak. A comparison can now be made of the 1^{-} behavior as derived from the methods of Rapaport and Goodman and an estimate of the background falloff energy for 120 MeV protons on ^{42,44} and ^{48}Ca from Osterfeld's work at 160 MeV. As can be seen from Table 4.4, the agreement is not bad, considering the crudeness of our procedure.

The 1^{+} cross sections at 0^{o}, derived from our DWBA analysis (peak and background included) were used to compute the total GT strength again. We found that for ^{44} and ^{48}Ca, 78% and 63% of the Sum rule predictions were obtained respectively. Appendix D contains the Tables listing the computations of the GT strength. Our analysis conforms with Osterfeld's calculations; there is some 1^{+} contribution from the background; but one has to look elsewhere for at least part of the sum rule strength. It should, however, be remembered that the decomposition of the data into different final state angular momenta, with only 3 forward angles is far from reliable. We therefore, believe that additional data at somewhat larger angles would help resolve this question unambiguously. One should also bear in mind the limitations of using the code DWBA 79 which assumes that the final states are bound while, in fact, they are not. Further, one does not have a check on the constancy of the angular distributions with excitation energy in the residual nucleus. Very often, DWBA predictions are not accurate because,

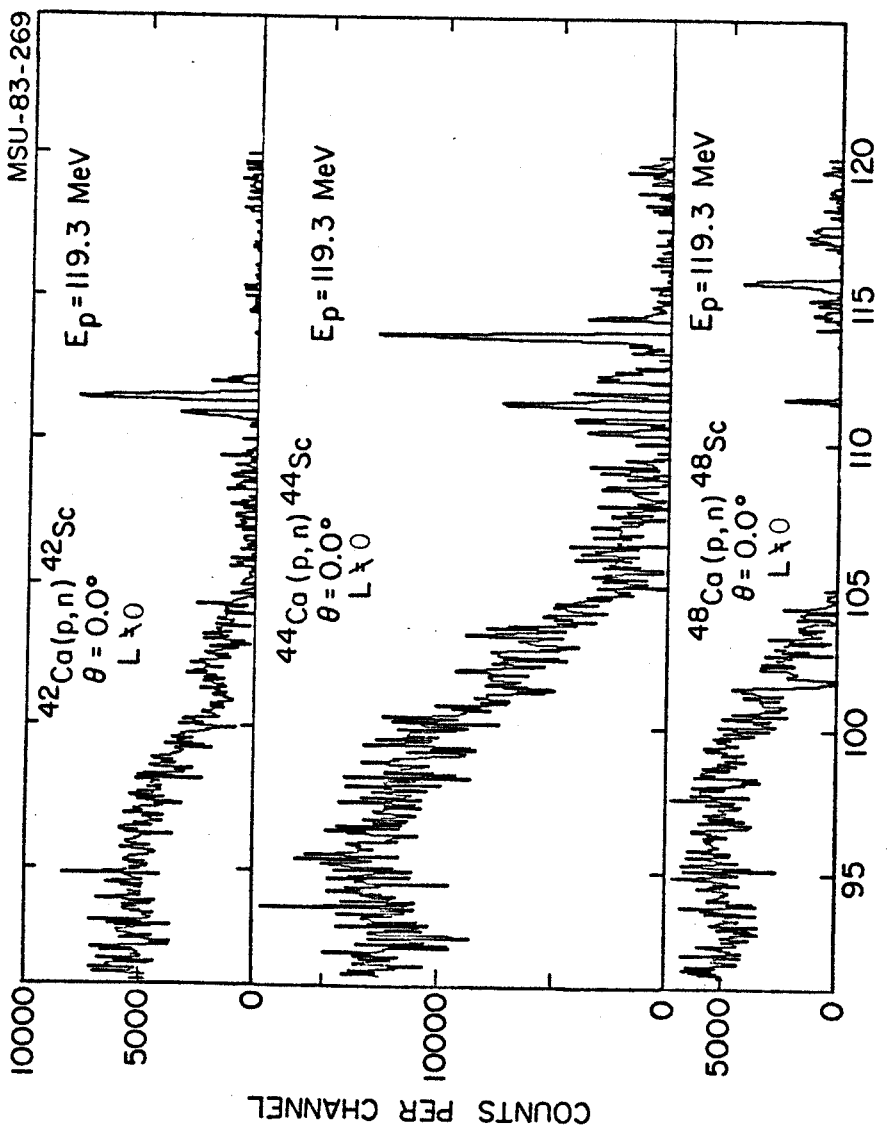

Figure 4.7. L≠0 spectra at $\Theta_{lab} = 0.0°$, for ^{42,44,48}Ca(p,n).

Table 4.4

Comparison of 1^- behavior from present data and background falloff energies (from Of 82)

Target	1^- falloff Energy† from $L \neq 0$ spectrum (Goodman's method)	Onset of 1^- Strength (Rapaport's method)	Estimate from Osterfeld's calculation
^{42}Ca	9.8	11.0	10.4
^{44}Ca	8.2	9.0	12.9
^{48}Ca	13.6	13.0	17.1

†All are excitation energies (in MeV)

for example, the effects of density dependence of the two body force V_{eff} are not very well understood.

There exists yet another way to extract GT strength in a straightforward way from our data. Recall that the method outlined in Chapter I and used to compute the GT strengths quoted in Chapter III relies on normalizing the 1^+ cross sections to that of the IAS; therefore, it is very sensitive to the measured cross section for the IAS. When there is an overlap of peaks near the IAS as in ^{44,48}Ca, the errors are larger than if the IAS were isolated as in ^{42}Ca. Consider now the measured GT strength from the 0.611 MeV peak in ^{42}Sc. Our calculations give a value of 2.55 (using an experimenter's background) while the matrix element obtained from β decay is 2.67 (Go 81). Therefore one can normalize all the measured 1^+ cross sections to the 0.611 MeV cross section in ^{42}Sc, with a known strength. This way, we can also extract B_{Ex}(GT) for the 2.73 MeV state in ^{40}Sc. We carried out such an analysis and obtained total GT strengths of 57.2% and 69.4% of the minimum sum rule prediction for ^{44} and ^{48}Ca, using an experimenter's background. When one includes 1^+ contributions from the background as derived from the DWBA analysis, the total GT strengths are 110.7% and 82.9% of the sum rule prediction for ^{44} and ^{48}Ca. The major limitation of this method is that it is sensitive to errors in normalizations arising from charge and target thickness uncertainties while the method of Taddeucci et al., is independent of such errors. Note also that the difference between the 2 methods results partly from the fact that the measured IAS cross sections for ^{42,44,48}Ca do not scale exactly with N-Z. Another reason the strength is larger when

normalized to 0.611 MeV state is that the extracted strength of 2.55 for the state is scaled to 2.67 (obtained from β decay measurements).

The large GT strength for ^{44}Ca as indicated by the DWBA analysis is presently not understood. Unfortunately, there are no previous (p,n) measurements on this target at intermediate energies for us to compare to. Evidently, this results from the persistence of considerable 1^+ strength at high excitations (see Figures 4.5 and 4.6) for ^{44}Ca, unlike the case of ^{40}Ca. We are currently investigating this. In the ^{40}Ca (p,n) data, there is a peak at 2.73 MeV, with L = 0 angular distribution. Normalizing to 0.611 MeV gives a strength of $B_{Ex}(GT)$ = 0.098 which compares well with the values of B_{Ex} (GT) 0.15 $_5$ 0.04 and 0.13 $_5$ 0.04 at 159.34 and 200.0 MeV respectively reported by Taddeucci et al., (Ta 82)

V. SUMMARY

The total GT strengths (percent of minimum sum rule prediction) extracted from our data using the different methods outlined earlier are shown below in Table 5.1. If one believes the fits obtained with the DWBA 79 analysis, it would seem that substantial GT strength is contained in the background and extends to higher excitations, as proposed by Bertsch, et al., (Be 82). But one should be aware of the ambiguities of these fits, as discussed in Chapter IV.

Our data for ^{40}Ca indicate a GT strength of 0.098 from the peak at E_x = 2.73 MeV. This compares with the values of 0.15 + 0.04 and 0.13 + 0.04 reported by Taddeucci et al.at E_p=159.0 and 200 MeV respectively, (Ta 81). Another finding from our data is that the 16.8 MeV state in ^{48}Sc is about 13% wider than the state at 2.52 MeV excitation. The FWHM's in the TOF spectra for these states are 8.5 channels (E_x = 16.8 MeV) and 7.5 channels (E_x = 2.52 MeV); this observation was made earlier by Anderson et al., (An 80).

Comparison of our data to the electron scattering studies of Steffen et al., (St 80) indicated the following (see Figs. 5.1 and 5.2).

(a) The 2.73 MeV peak in ^{40}Sc has been identified on the analog of the 10.32 MeV state in ^{40}Ca (Ta 82); it has an angular distribution corresponding to L = 0.

(b) More structure is seen in ^{42}Sc than just the analog of the 11.2 MeV state in ^{42}Ca, although it has not been isolated and identified in our data.

(c) Electron scattering reveals practically no structure in ^{44}Ca, while the (p,n) experiment indicates significant GT strength in the excitation range 10.8 to 14.5 MeV.

Table 5.1
Total GT strength from the present data
(as percent of minimum sum rule prediction)

Target	Experimenter's Background			Peak+Background DWBA 79 Analysis		
	Normalize to IAS	Normalize to 0.611 MeV State	Other (p,n) Measurement	Normalize to IAS	Normalize to 0.611 MeV State	Other (p,n) Measurement
^{42}Ca	82.0	-	56.7[a]	-	-	-
^{44}Ca	40.5	57.2	-	78.3	110.7	-
^{48}Ca	51.7	69.4	43.0[b]	62.6	82.9	51.0[b]

[a] C.D. Goodman et al., Phys. Lett. 107B, 406 (1981).

[b] F. Osterfeld, Phys. Rev. C 26, 762 (1982).

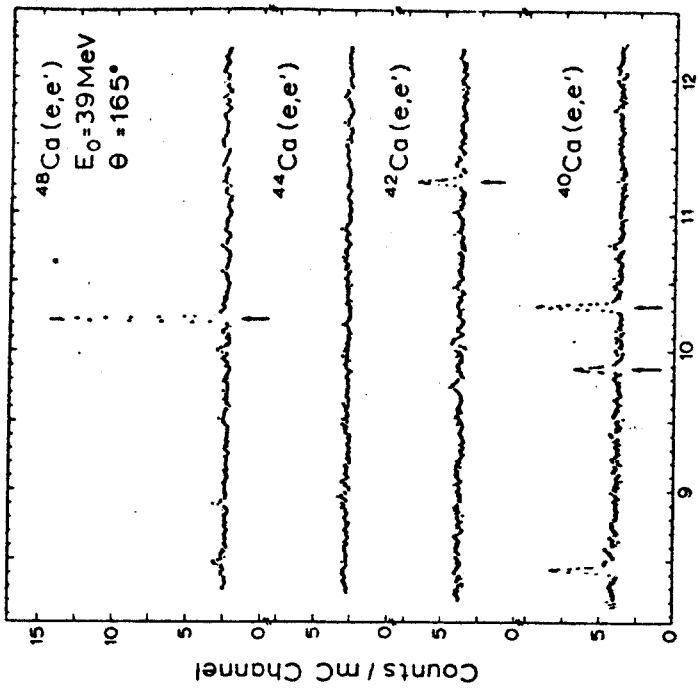

Fig. 5.2 High-resolution inelastic electron scattering spectra of ^{40,42,44,48}Ca all measured at θ = 165° and E_0 = 39 MeV. Magnetic dipole transitions are denoted by an arrow. (Figure and caption from Steffen et al., (St 80).)

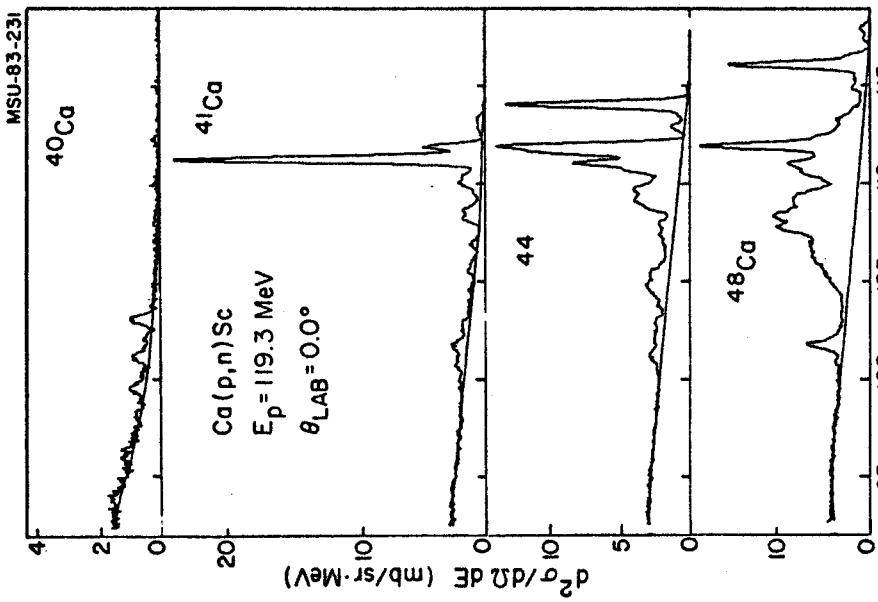

Figure 5.1. Energy spectra for θ_{lab} = 0.0°. Present study.

(d) The analog of the 10.3 MeV M1 state in ^{48}Ca is seen clearly in ^{48}Sc at E_x = 16.8 MeV; this seems to be the only strong resonance in the range of excitation observed.

APPENDICES

APPENDIX A

Derivation of nonenergy weighted sum rule of isovector (T=1) spin flip and non-spin flip operators

APPENDIX A

Derivation of non-energy weighted sum rule of isovector (T=1) spin flip and non-spin flip operators:

Consider

$$\hat{O}_{\pm,F} = \sum_k t_\pm^k \qquad \text{Fermi (non-spin flip)}$$

$$\hat{O}_{\pm,GT} = \sum_k \sigma_k \, t_\pm^k \qquad \text{Gamow Teller (spin flip)}$$

The sum $\sum$ is over the nucleons in the nucleus.

Define

$$S(\beta_- - \beta_+) = \sum_f |\langle f|\hat{O}_-|i\rangle|^2 - \sum_f |\langle f|\hat{O}_+|i\rangle|^2$$

$$= \sum_f \langle f|\hat{O}_-|i\rangle^* \langle f|\hat{O}_-|i\rangle - \sum_f \langle f|\hat{O}_+|i\rangle^* \langle f|\hat{O}_+|i\rangle$$

$$= \sum_f \langle i|\hat{O}_-^\dagger|f\rangle\langle f|\hat{O}_-|i\rangle - \sum_f \langle i|\hat{O}_+^\dagger|f\rangle\langle f|\hat{O}_+|i\rangle$$

$$= \langle i|\hat{O}_-^\dagger O_-|i\rangle - \langle i|\hat{O}_+^\dagger O_+|i\rangle$$

It can be shown that for both Fermi and GT operations,

$$O_-^\dagger = O_+ \text{ and } O_+^\dagger = O_-$$

Then, $S(\beta_- - \beta_+) = \langle i|\hat{0}_+\hat{0}_- - \hat{0}_-\hat{0}_+|i\rangle$

$= \langle i|[\hat{0}_+,\hat{0}_-]|i\rangle$

For Fermi, $[0_+,0_-] = \sum_{k,k'} [t_+^k, t_-^{k'}]$

$\therefore S_{\beta-} - S_{\beta+} = \langle i| \sum_{k,k'} \delta_{kk'}\ 2t_z^k |i\rangle$

$= 2 \sum_k t_z^k$

$= 2 \cdot \frac{1}{2} \cdot (N-Z) = N-Z$

For GT, $[0_+,0_-] = \sum_{k,k'} [\sigma_k t_+^k, \sigma_k, t_-^{k'}]$

$\therefore S_{\beta-} - S_{\beta+} = \langle i| \sum_{k,k'} \delta_{kk'} (\sigma_{x,k'}^2 + \sigma_{y,k'}^2 + \sigma_{z,k'}^2) \delta\ 2t_z^{k'} |i\rangle$

$= 3 \cdot 2 \cdot \frac{1}{2}\ (N-Z)$

$= 3(N-Z)$

APPENDIX B

SPECTRA

(EFFICIENCY CORRECTED AND

ENERGY CALIBRATED)

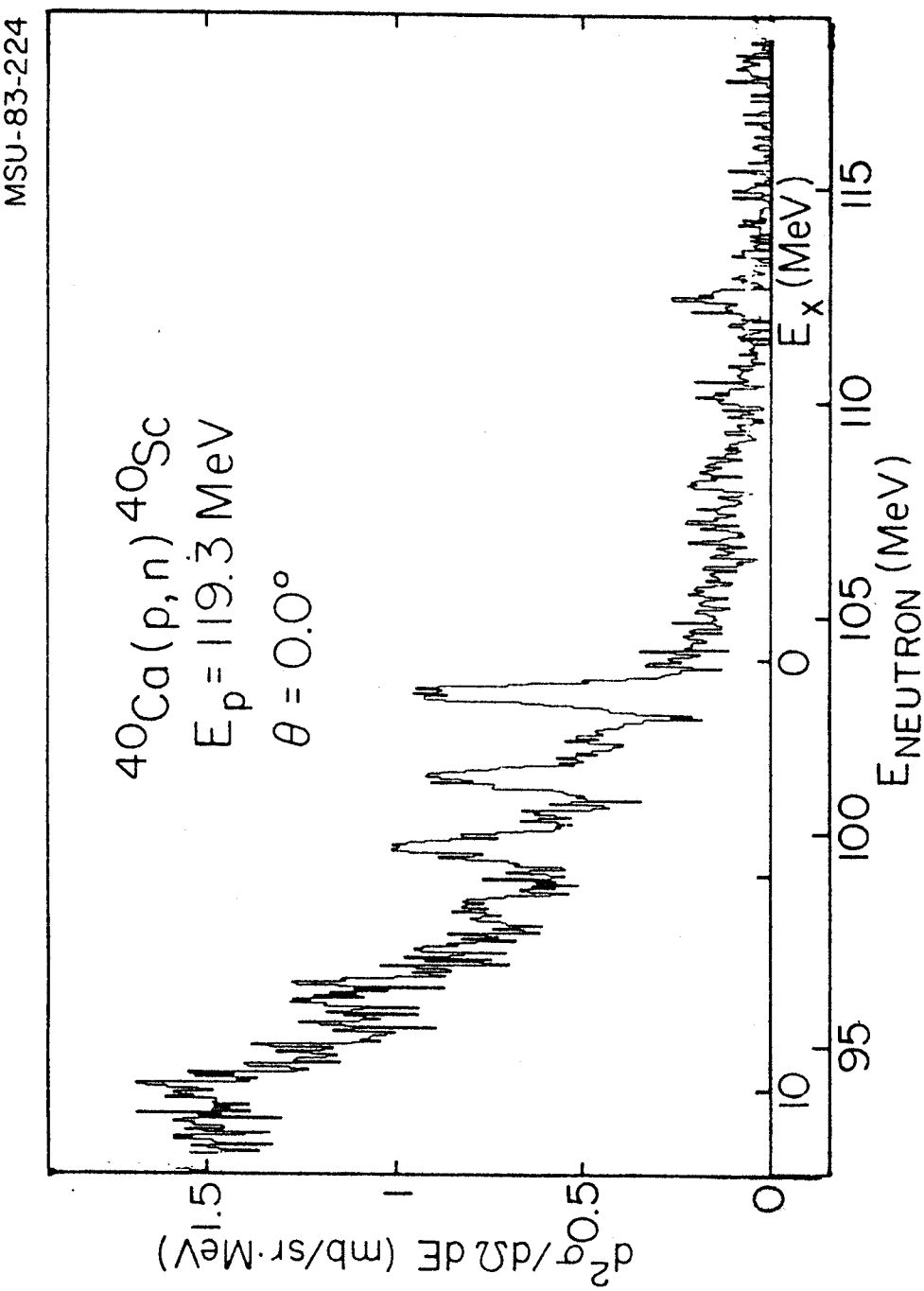
MSU-83-224
$^{40}Ca(p,n)^{40}Sc$
$E_p = 119.3$ MeV
$\theta = 0.0°$
$d^2\sigma/d\Omega\, dE$ (mb/sr·MeV)
1.5
1
0.5
0
10
95
0
100
105
110
115
E_x (MeV)
$E_{NEUTRON}$ (MeV)

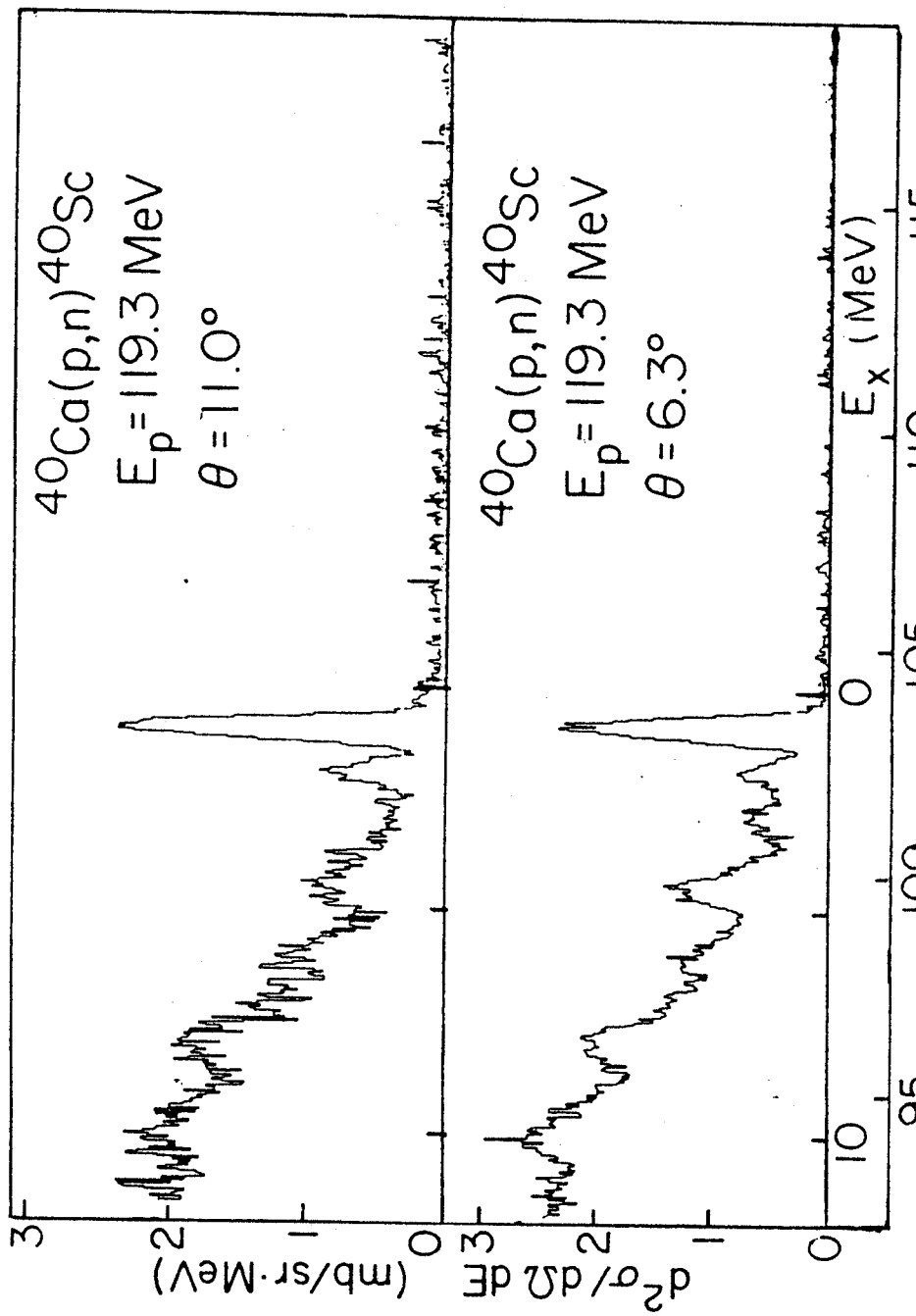
MSU-83-225
$^{40}Ca(p,n)^{40}Sc$
E_p=119.3 MeV
θ=11.0°
$^{40}Ca(p,n)^{40}Sc$
E_p=119.3 MeV
θ=6.3°
$d^2\sigma/d\Omega\,dE$ (mb/sr·MeV)
$E_{NEUTRON}$ (MeV)
E_x (MeV)

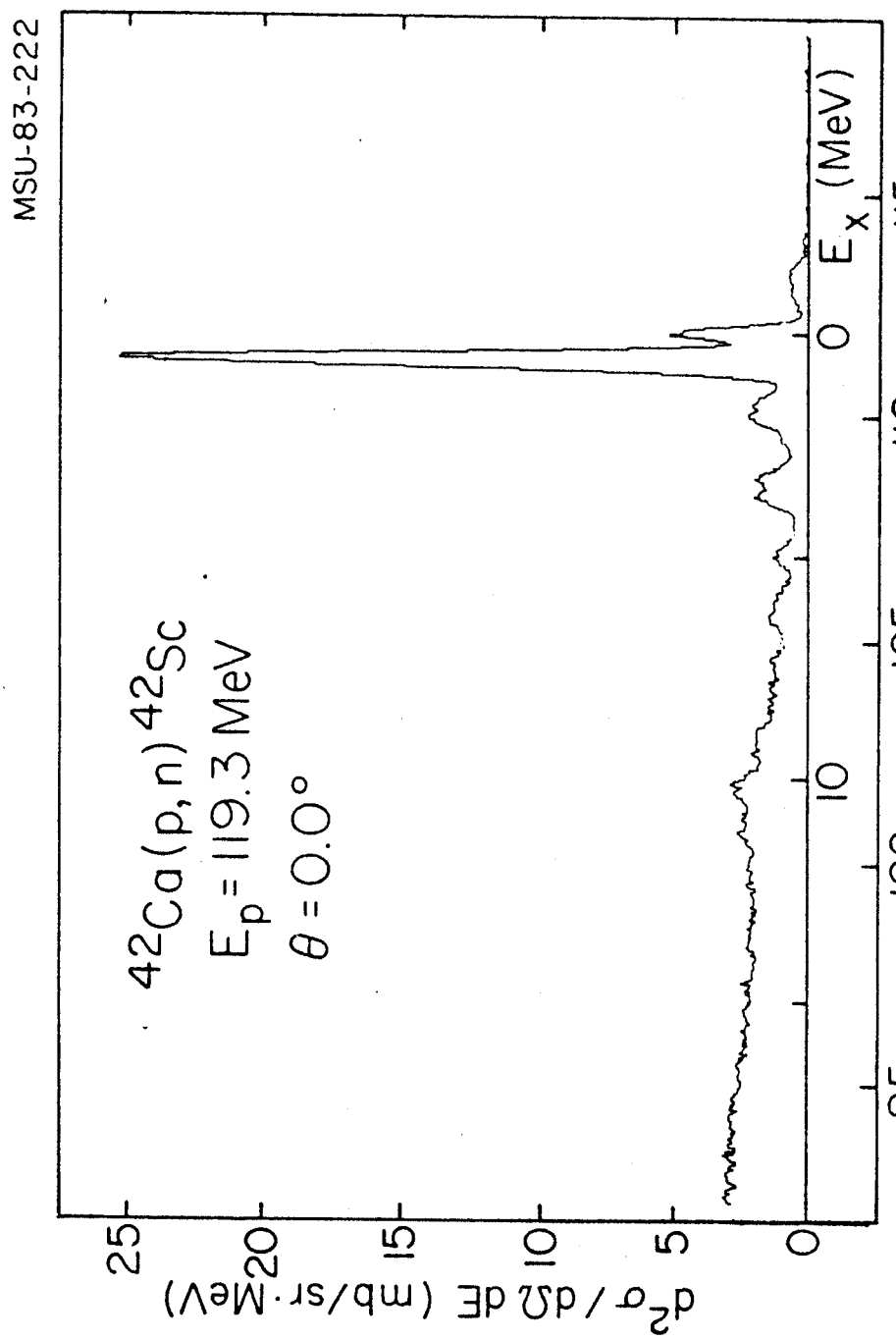
MSU-83-222
$^{42}Ca(p,n)^{42}Sc$
$E_p = 119.3$ MeV
$\theta = 0.0°$
$d^2\sigma/d\Omega\,dE$ (mb/sr·MeV)
25
20
15
10
5
0
95
100
105
110
115
10
0
E_x (MeV)
$E_{NEUTRON}$ (MeV)

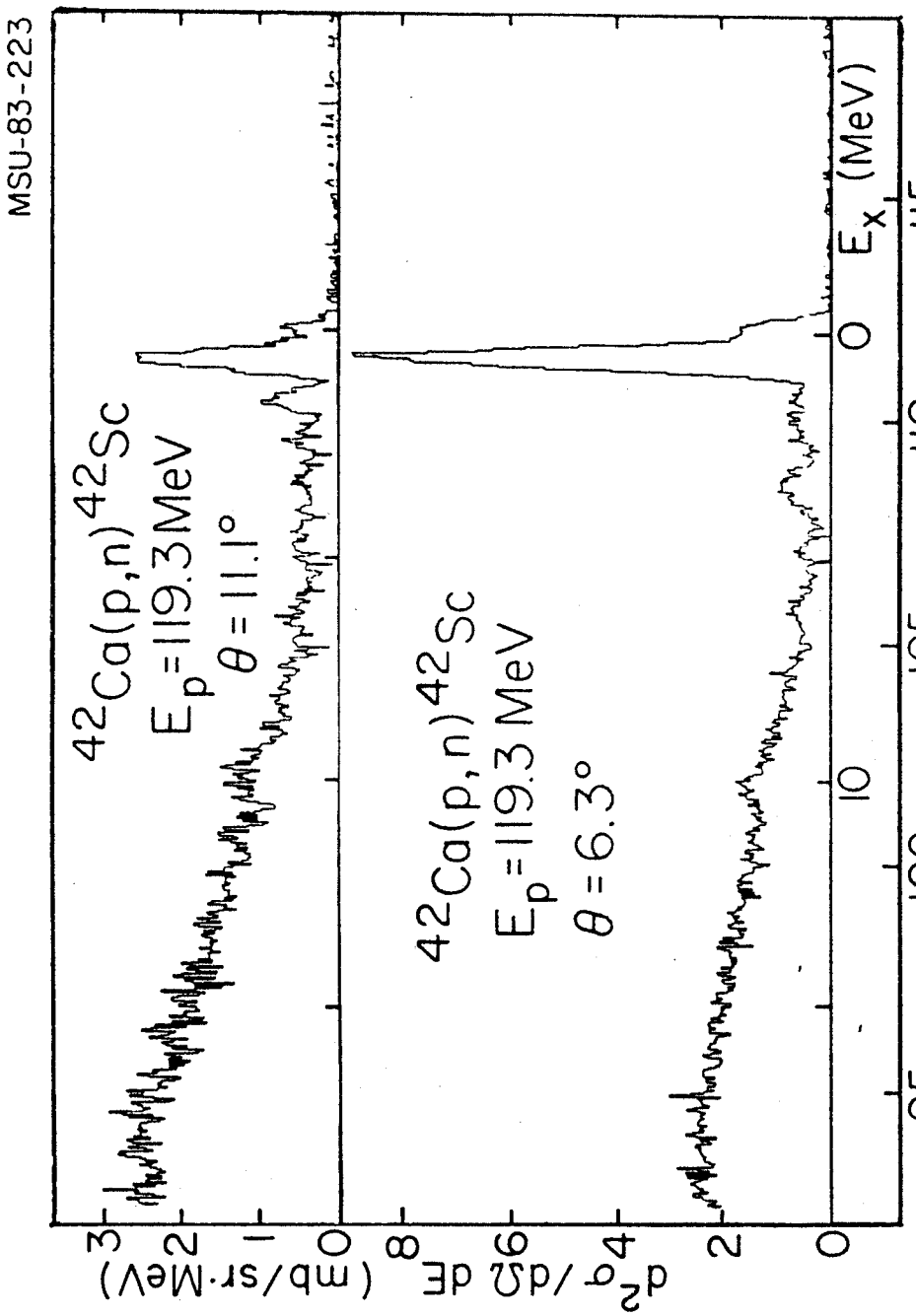
MSU-83-223
$^{42}Ca(p,n)^{42}Sc$
E_p=119.3MeV
θ=11.1°
$^{42}Ca(p,n)^{42}Sc$
E_p=119.3 MeV
θ=6.3°
$d^2\sigma/d\Omega\, dE$ (mb/sr·MeV)
$E_{NEUTRON}$ (MeV)
E_x (MeV)

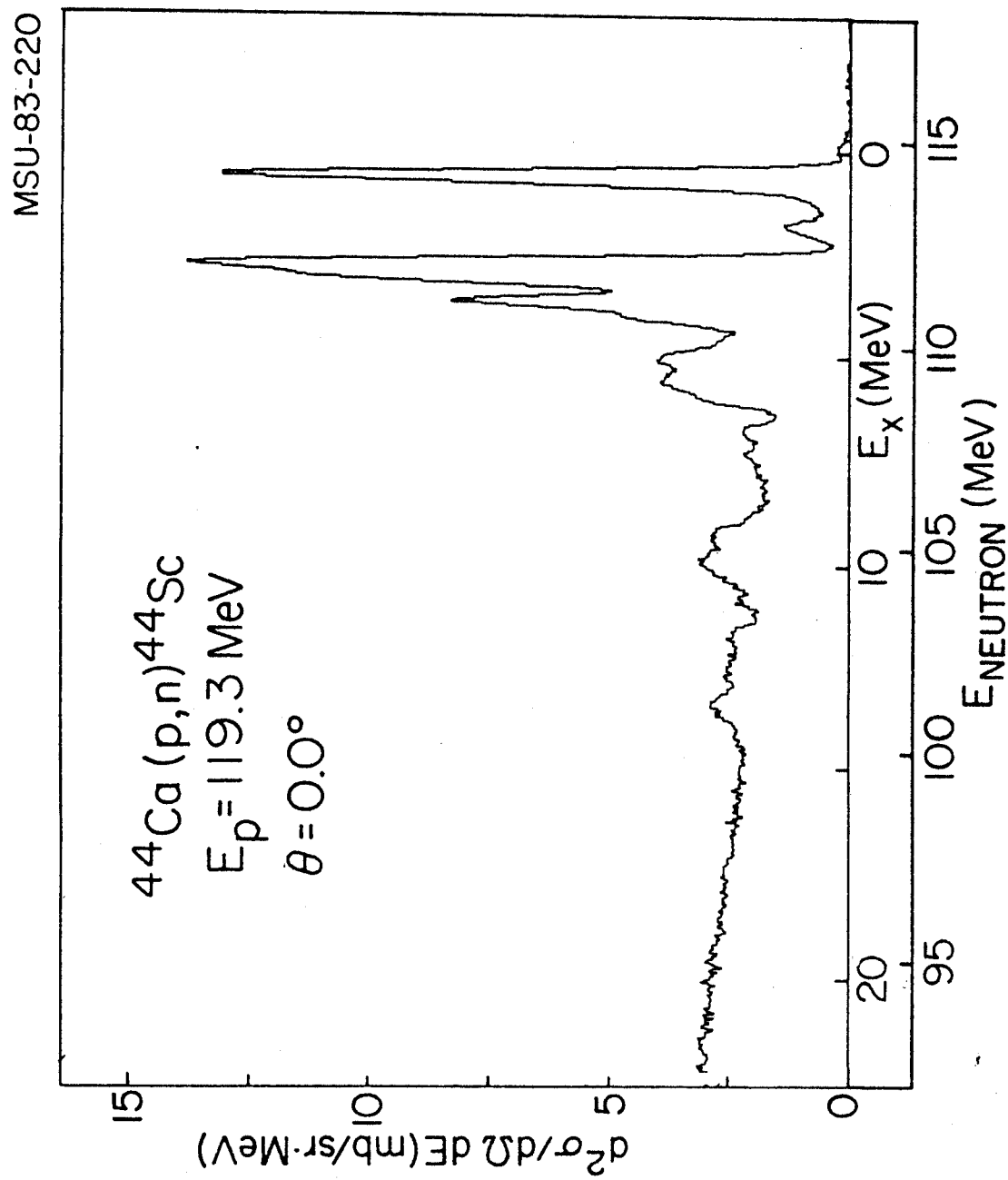
MSU-83-220
$^{44}Ca(p,n)^{44}Sc$
$E_p = 119.3$ MeV
$\theta = 0.0°$
$d^2\sigma/d\Omega\, dE$ (mb/sr·MeV)
0
5
10
15
20
10
0
E_x (MeV)
95
100
105
110
115
$E_{NEUTRON}$ (MeV)

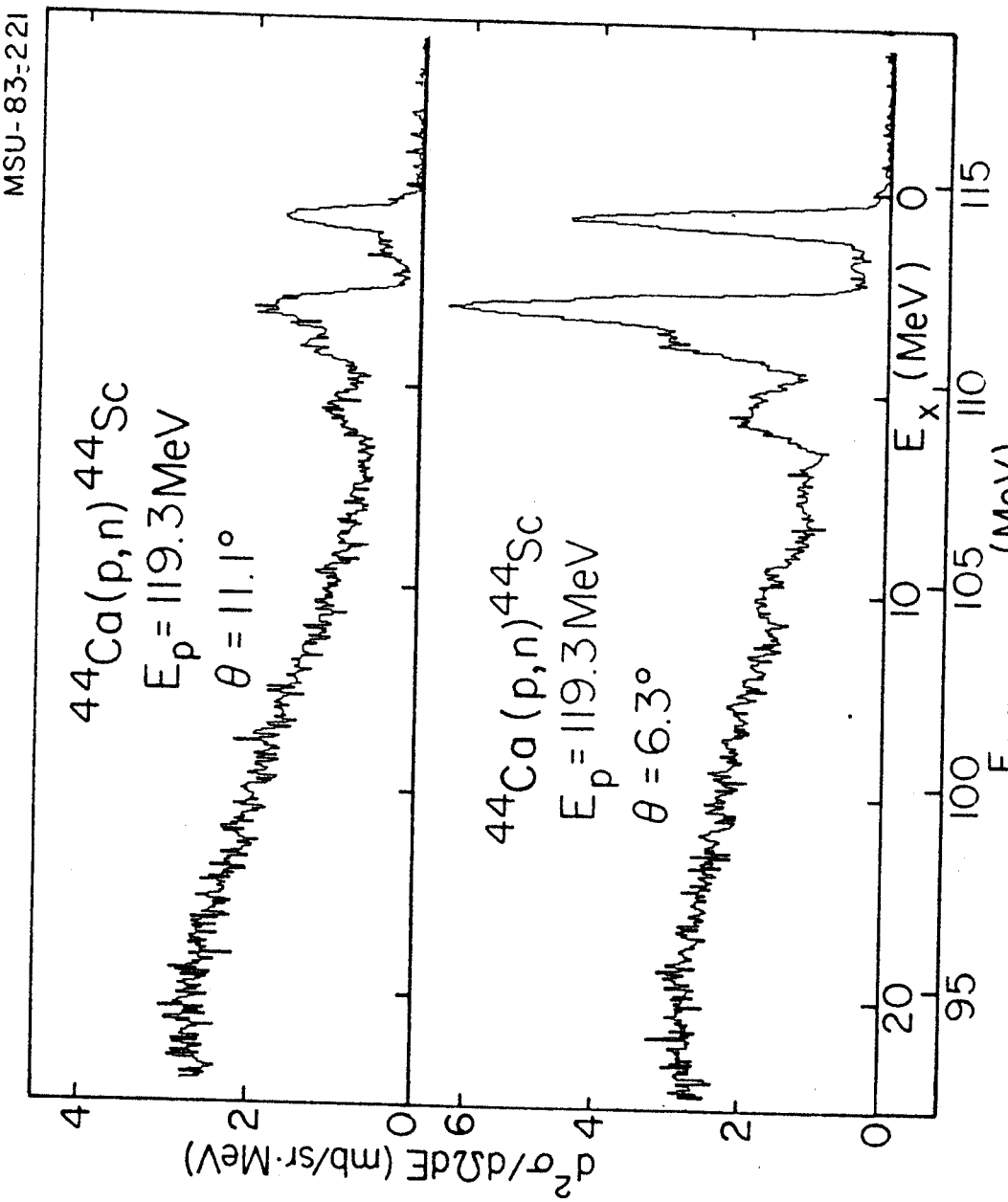
MSU-83-221
$^{44}Ca(p,n)^{44}Sc$
E_p=119.3MeV
θ = 11.1°
$^{44}Ca(p,n)^{44}Sc$
E_p=119.3MeV
θ = 6.3°
$d^2\sigma/d\Omega dE$ (mb/sr·MeV)
$E_{NEUTRON}$ (MeV)
E_x (MeV)

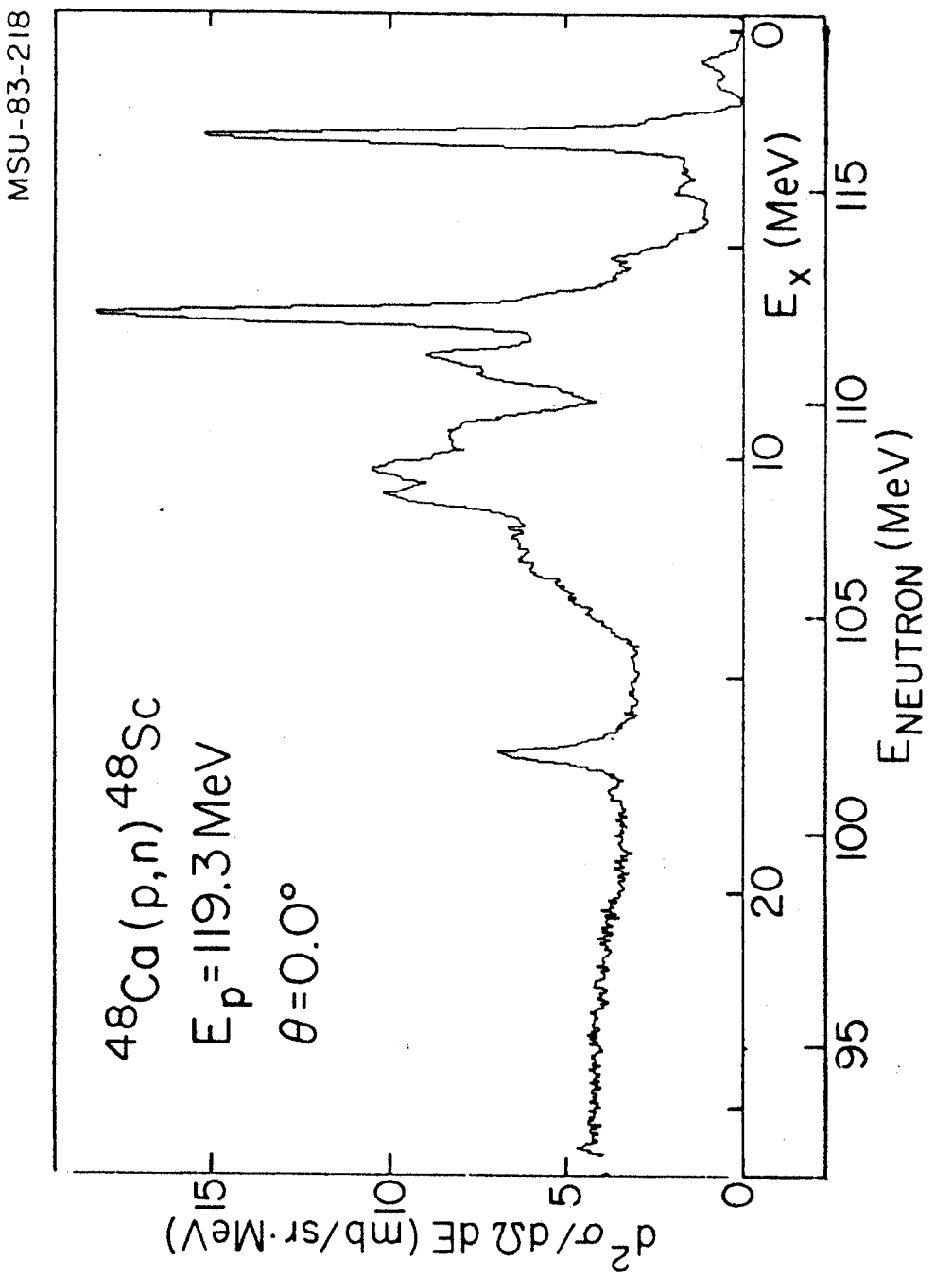
MSU-83-218
$^{48}Ca(p,n)^{48}Sc$
E_p=119.3 MeV
θ=0.0°
$d^2\sigma/d\Omega\, dE$ (mb/sr·MeV)
0
5
10
15
95
100
105
110
115
$E_{NEUTRON}$ (MeV)
0
10
20
E_x (MeV)

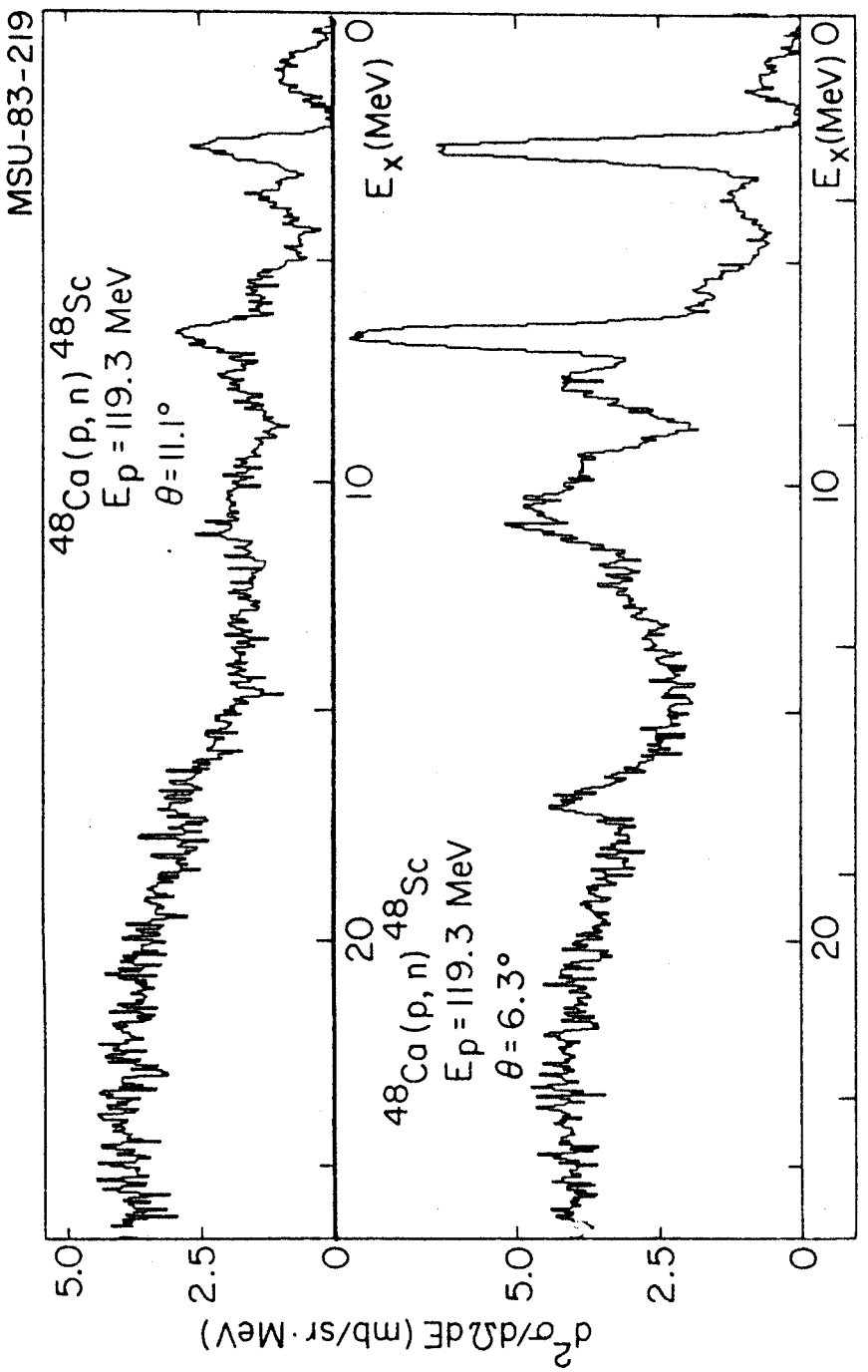
MSU-83-219
^{48}Ca(p, n) ^{48}Sc
Ep = 119.3 MeV
θ = 11.1°
^{48}Ca(p, n) ^{48}Sc
Ep = 119.3 MeV
θ = 6.3°
Ex(MeV)
d²σ/dΩdE (mb/sr·MeV)
E Neutron (MeV)

APPENDIX C

MONTE CARLO CALCULATIONS OF

NEUTRON DETECTOR EFFICIENCIES (RELATIVE)

At each energy 32000 neutrons are incident on the detector. The tabulated numbers are the percentage of neutrons detected at a given bias. The bias is expressed in MeV of electron energy. The first row contains results for biases of 0 to 9 MeV, the second row results for biases of 10 to 19 MeV, etc.

32000 Neutrons of Energy 120.00 ± 2.00 MeV

INCIDENT AT X,Y,Z= 0.0 0.0 0.0 INCHES
DIRECTION COSINES= 0.9400 0.0 0.3420

** RANDOM INITIAL POSITION **

LAST SEED NUMBER 2163607704
TOTAL NUMBER OF NEUTRONS DETECTED 18071

120 MeV

INTEGRAL EFFICIENCY, ONE P.E.= 0.002 MEV BIN WIDTH ,1.000 MEV
NOTE FIRST BIN CORRESPONDS TO ZERO BIAS.

	0	1	2	3	4	5	6	7	8	9
	0.5460	0.3330	0.3235	0.3164	0.3087	0.3008	0.2954	0.2898	0.2842	0.2792
10	0.2720	0.2683	0.2633	0.2580	0.2530	0.2473	0.2423	0.2374	0.2328	0.2272
20	0.2220	0.2187	0.2132	0.2090	0.2037	0.1990	0.1943	0.1896	0.1852	0.1810
30	0.1770	0.1727	0.1691	0.1655	0.1620	0.1582	0.1552	0.1519	0.1489	0.1463
40	0.1430	0.1398	0.1366	0.1337	0.1306	0.1277	0.1246	0.1216	0.1183	0.1158
50	0.1122	0.1088	0.1058	0.1025	0.0999	0.0969	0.0943	0.0914	0.0883	0.0858
60	0.0832	0.0800	0.0774	0.0749	0.0725	0.0698	0.0670	0.0644	0.0610	0.0585
70	0.0563	0.0537	0.0512	0.0492	0.0469	0.0443	0.0415	0.0391	0.0367	0.0343
	0.0329	0.0297	0.0276	0.0256	0.0238	0.0221	0.0207	0.0193	0.0181	0.0170
	0.0161	0.0149	0.0144	0.0137	0.0128	0.0117	0.0108	0.0100	0.0092	0.0082
	0.0074	0.0063	0.0052	0.0041	0.0028	0.0015	0.0006			

32000 Neutrons of Energy 115.00 ± 2.00 MeV

INCIDENT AT X,Y,Z= 0.0 0.0 0.0 INCHES
DIRECTION COSINES= 0.9400 0.0 0.3420

** RANDOM INITIAL POSITION **

LAST SEED NUMBER 1153736416
TOTAL NUMBER OF NEUTRONS DETECTED 18212

INTEGRAL EFFICIENCY,ONE P.E.= 0.002 MEV BIN WIDTH ,1.000 MEV
NOTE FIRST BIN CORRESPONDS TO ZERO BIAS.

	0	1	2	3	4	5	6	7	8	9
	0.3514	0.3339	0.3245	0.3165	0.3082	0.2999	0.2939	0.2884	0.2829	0.2780
10	0.2724	0.2678	0.2623	0.2572	0.2512	0.2457	0.2402	0.2352	0.2293	0.2244
20	0.2200	0.2159	0.2113	0.2065	0.2016	0.1969	0.1923	0.1874	0.1828	0.1791
30	0.1747	0.1701	0.1665	0.1621	0.1573	0.1538	0.1503	0.1465	0.1428	0.1393
40	0.1361	0.1325	0.1294	0.1261	0.1229	0.1203	0.1170	0.1141	0.1110	0.1085
50	0.1059	0.1027	0.0993	0.0959	0.0922	0.0890	0.0858	0.0830	0.0798	0.0776
60	0.0750	0.0717	0.0690	0.0661	0.0635	0.0606	0.0581	0.0559	0.0525	0.0499
70	0.0475	0.0447	0.0419	0.0394	0.0374	0.0349	0.0324	0.0303	0.0281	0.0265
	0.0250	0.0234	0.0220	0.0207	0.0192	0.0185	0.0175	0.0167	0.0158	0.0147
	0.0137	0.0129	0.0119	0.0110	0.0100	0.0094	0.0072	0.0059	0.0047	0.0033
	0.0018	0.0005	0.0000							

32000 Neutrons of Energy 110.00 ± 2.00 MeV

INCIDENT AT X,Y,Z= 2.0 0.0 0.0 INCHES
DIRECTION COSINES= 0.9400 0.0 0.3420

** RANDOM INITIAL POSITION **

LAST SEED NUMBER 1663635200
TOTAL NUMBER OF NEUTRONS DETECTED 18418

INTEGRAL EFFICIENCY, ONE P.E.= 0.002 MEV BIN WIDTH ,1.000 MEV
NOTE FIRST BIN CORRESPONDS TO ZERO BIAS.

0	1	2	3	4	5	6	7	8	9
0 0.5570	0.3333	0.3281	0.3198	0.3116	0.3037	0.2980	0.2929	0.2869	0.2804
10 0.2752	0.2695	0.2634	0.2576	0.2515	0.2463	0.2408	0.2356	0.2301	0.2252
20 0.2196	0.2149	0.2088	0.2040	0.1987	0.1932	0.1879	0.1823	0.1775	0.1728
30 0.1686	0.1646	0.1606	0.1564	0.1521	0.1485	0.1447	0.1408	0.1376	0.1350
40 0.1313	0.1280	0.1239	0.1218	0.1174	0.1131	0.1096	0.1062	0.1034	0.1000
50 0.0970	0.0936	0.0903	0.0872	0.0843	0.0812	0.0782	0.0751	0.0719	0.0692
60 0.0667	0.0634	0.0607	0.0578	0.0549	0.0520	0.0491	0.0459	0.0428	0.0406
70 0.0378	0.0348	0.0320	0.0297	0.0273	0.0252	0.0237	0.0219	0.0203	0.0189
80 0.0180	0.0170	0.0162	0.0154	0.0145	0.0134	0.0126	0.0115	0.0103	0.0095
90 0.0083	0.0074	0.0062	0.0047	0.0036	0.0024	0.0009	0.0002		

32000 Neutrons of Energy 105.00 ± 2.00 MeV

INCIDENT AT X,Y,Z 0.0 0.0 0.0 INCHES
DIRECTION COSINE 0.9400 0.00 0.3420

** RANDOM INITIAL POSITION **

LAST SEED NUMBER 522949888
TOTAL NUMBER OF NEUTRONS DETECTED 18766

INTEGRAL EFFICIENCY, ONE P.E. = 0.002 MEV BIN WIDTH, 1.000 MEV
NOTE FIRST BIN CORRESPONDS TO ZERO BIAS.

	0	1	2	3	4	5	6	7	8	9
	0.5674	0.3442	0.3324	0.3240	0.3149	0.3065	0.3005	0.2944	0.2892	0.2834
10	0.2773	0.2717	0.2655	0.2592	0.2535	0.2479	0.2424	0.2366	0.2313	0.2256
20	0.2195	0.2138	0.2084	0.2032	0.1981	0.1925	0.1877	0.1828	0.1778	0.1727
30	0.1681	0.1632	0.1589	0.1546	0.1514	0.1477	0.1437	0.1402	0.1362	0.1328
40	0.1294	0.1256	0.1218	0.1186	0.1156	0.1116	0.1078	0.1040	0.1005	0.0972
50	0.0937	0.0897	0.0865	0.0831	0.0796	0.0763	0.0730	0.0692	0.0657	0.0618
60	0.0582	0.0557	0.0530	0.0499	0.0469	0.0437	0.0404	0.0377	0.0347	0.0324
70	0.0301	0.0283	0.0267	0.0248	0.0230	0.0218	0.0206	0.0195	0.0188	0.0178
80	0.0166	0.0155	0.0145	0.0133	0.0122	0.0111	0.0092	0.0075	0.0060	0.0044
90	0.0027	0.0012	0.0003							

32000 Neutrons of Energy 100.00 ± 2.00 MeV

INCIDENT AT X,Y,Z= 0.0 0.0 0.0 INCHES
DIRECTION COSINES 0.9400 0.0 0.3420

** RANDOM INITIAL POSITION **

LAST SEED NUMBER 423616256
TOTAL NUMBER OF NEUTRONS DETECTED 19029

INTEGRAL EFFICIENCY, ONE P.E.= 0.302 MEV BIN WIDTH ,1.000 MEV
NOTE FIRST BIN CORRESPONDS TO ZERO BIAS.

	0	1	2	3	4	5	6	7	8	9
0	0.5763	0.3442	0.3341	0.3245	0.3152	0.3068	0.3010	0.2947	0.2887	0.2821
10	0.2760	0.2696	0.2641	0.2578	0.2514	0.2447	0.2376	0.2316	0.2257	0.2199
20	0.2131	0.2074	0.2015	0.1964	0.1906	0.1857	0.1804	0.1750	0.1707	0.1654
30	0.1600	0.1572	0.1527	0.1487	0.1452	0.1407	0.1369	0.1326	0.1281	0.1243
40	0.1203	0.1164	0.1117	0.1073	0.1036	0.1002	0.0961	0.0928	0.0892	0.0855
50	0.0822	0.0787	0.0747	0.0714	0.0681	0.0653	0.0614	0.0575	0.0534	0.0502
60	0.0469	0.0432	0.0399	0.0372	0.0341	0.0312	0.0288	0.0271	0.0253	0.0235
70	0.0224	0.0211	0.0201	0.0192	0.0183	0.0170	0.0156	0.0143	0.0131	0.0122
80	0.0109	0.0096	0.0078	0.0060	0.0047	0.0030	0.0018	0.0006	0.0001	

32000 Neutrons of Energy 90.00 ± 2.00 MeV

INCIDENT AT X,Y,Z= 0.0 0.0 0.0 INCHES
DIRECTION COSINES= 0.9400 0.0 0.3420

** RANDOM INITIAL POSITION **

LAST SEED NUMBER 371773184
TOTAL NUMBER OF NEUTRONS DETECTED 19888

INTEGRAL EFFICIENCY,ONE P.E.= 0.002 MEV BIN WIDTH ,1.000 MEV
NOTE FIRST BIN CORRESPONDS TO ZERO BIAS.

	0	1	2	3	4	5	6	7	8	9
	0.6291	0.3591	0.3472	0.3382	0.3282	0.3182	0.3114	0.3043	0.2961	0.2887
1	0.2817	0.2737	0.2657	0.2591	0.2503	0.2426	0.2360	0.2286	0.2222	0.2156
2	0.2094	0.2030	0.1973	0.1916	0.1656	0.1797	0.1733	0.1684	0.1642	0.1594
3	0.1546	0.1500	0.1457	0.1414	0.1370	0.1327	0.1280	0.1233	0.1192	0.1148
4	0.1107	0.1066	0.1020	0.0976	0.0932	0.0899	0.0844	0.0800	0.0763	0.0722
5	0.0676	0.0624	0.0577	0.0542	0.0501	0.0463	0.0429	0.0402	0.0372	0.0347
6	0.0323	0.0295	0.0291	0.0273	0.0258	0.0244	0.0232	0.0213	0.0195	0.0177
7	0.0160	0.0140	0.0118	0.0096	0.0077	0.0055	0.0032	0.0013	0.0003	

32000 Neutrons of Energy 80.00 ± 2.00 MeV

INCIDENT AT X,Y,Z= 0.0 0.0 0.0 INCHES
DIRECTION COSINES= 1.0000 0.0 0.0000

** RANDOM INITIAL POSITION **

LAST SEED NUMBER 1256435424
TOTAL NUMBER OF NEUTRONS DETECTED 20510

INTEGRAL EFFICIENCY, ONE P.E.= 0.002 MEV BIN WIDTH = 1.000 MEV
NOTE FIRST BIN CORRESPONDS TO ZERO BIAS.

0	1	2	3	4	5	6	7	8	9
0.6211	0.3716	0.3573	0.3456	0.3341	0.3238	0.3154	0.3053	0.2959	0.2870
0.2782	0.2694	0.2600	0.2507	0.2422	0.2346	0.2267	0.2196	0.2120	0.2049
0.1978	0.1901	0.1836	0.1775	0.1723	0.1664	0.1609	0.1558	0.1506	0.1451
0.1407	0.1358	0.1293	0.1240	0.1183	0.1134	0.1081	0.1034	0.0977	0.0921
0.0867	0.0814	0.0760	0.0709	0.0653	0.0602	0.0557	0.0510	0.0467	0.0436
0.0408	0.0385	0.0368	0.0354	0.0332	0.0313	0.0297	0.0280	0.0257	0.0231
0.0206	0.0184	0.0166	0.0142	0.0114	0.0088	0.0057	0.0029	0.0008	0.0000

32000 Neutrons of Energy 70.00 ± 2.00 MeV

INCIDENT AT X,Y,Z= Ø.Ø Ø.Ø Ø.Ø INCHES
DIRECTION COSINES= Ø.94ØØ Ø.Ø Ø.3420

** RANDOM INITIAL POSITION **

LAST SEED NUMBER 698230016
TOTAL NUMBER OF NEUTRONS DETECTED 21553

INTEGRAL EFFICIENCY,ONE P.E.= Ø.ØØ2 MEV BIN WIDTH ,1.ØØØ MEV
NOTE FIRST BIN CORRESPONDS TO ZERO BIAS.

	1	2	3	4	5	6	7	8	9
Ø	Ø.6514	Ø.3930	Ø.3766	Ø.3634	Ø.3494	Ø.3388	Ø.3268	Ø.3145	Ø.3031	Ø.2921
1Ø	Ø.2793	Ø.2678	Ø.2564	Ø.2447	Ø.2343	Ø.2242	Ø.2139	Ø.2046	Ø.1951	Ø.1878
2Ø	Ø.1897	Ø.1756	Ø.1697	Ø.1632	Ø.1565	Ø.1507	Ø.1440	Ø.1374	Ø.1313	Ø.1245
3Ø	Ø.1173	Ø.1109	Ø.1043	Ø.ØØ72	Ø.ØØØ2	Ø.ØØ828	Ø.ØØ765	Ø.ØØ7Ø1	Ø.ØØ641	Ø.ØØ586
4Ø	Ø.ØØ537	Ø.ØØ492	Ø.ØØ464	Ø.ØØ441	Ø.ØØ423	Ø.ØØ4Ø5	Ø.ØØ383	Ø.ØØ363	Ø.ØØ338	Ø.ØØ315
5Ø	Ø.ØØ293	Ø.ØØ255	Ø.ØØ226	Ø.ØØ2Ø1	Ø.ØØ163	Ø.ØØ132	Ø.ØØ1Ø6	Ø.ØØ1Ø57	Ø.ØØ1Ø2Ø	Ø.ØØ1Ø3

70 MeV